Molecular Dynamics Simulation Studies on Deformation and Fracture Behaviour of BCC Fe Nanowires : Influence of Orientation, Mode of Loading, Size, Temperature and Boundaries

By

G. Sainath

(Enrolment No. : PHYS 02 2014 04 012)

Indira Gandhi Centre for Atomic Research

Kalpakkam - 603102, India

A thesis submitted to the

Board of Studies in Physical Sciences

In partial fulfillment of requirements

for the Degree of

DOCTOR OF PHILOSOPHY

of

HOMI BHABHA NATIONAL INSTITUTE

Mumbai, India

March, 2018

Certificate Will be Uploaded Soon

ACKNOWLEDGEMENTS

To my grandmother

8. Applicability of Voce equation for tensile flow and work hardening behaviour of P92 ferritic steel, **G. Sainath**, B.K. Choudhary, J. Christopher, E.I. Samuel, M.D. Mathew, *International Journal of Pressure Vessels and Piping* 132 (**2015**) 1-9. https://doi.org/10.1016/j.ijpvp.2015.05.004.

9. Molecular dynamics simulation of twin boundary effect on deformation of Cu nanopillars, **G. Sainath**, B.K. Choudhary, *Physics Letters A* 379 (**2015**) 1902-1905. https://doi.org/10.1016/j.physleta.2015.05.027.

10. Effects of temperature and strain rate on tensile stress-strain and workhardening behaviour of P92 ferritic steel, **G. Sainath**, B.K. Choudhary, J. Christopher, E.I. Samuel, M.D. Mathew, *Materials Science Technology* 30 (**2014**) 911-920. https://doi.org/10.1179/1743284713Y.0000000349.

11. Influence of temperature and strain rate on tensile deformation and fracture behavior of P92 ferritic steel, B.K. Choudhary, E.I. Samuel, **G. Sainath**, J. Christopher, M.D. Mathew, *Metallurgy and Materials Transactions A* 44 (**2013**) 4979-4992. https://doi.org/10.1007/s11661-013-1869-6.

12. Effect of temperature and strain amplitude on fatigue behaviour of bcc iron single crystal using molecular dynamics simulations, V.S. Srinivasan, **G. Sainath**, B.K. Choudhary, M.D. Mathew, T. Jayakumar, *Procedia Engineering* 55 (**2013**) 742-746. https://doi.org/10.1016/j.proeng.2013.03.324.

13. Continuum damage mechanics approach to predict creep behaviour of modified 9Cr-1Mo ferritic steel at 873K, J. Christopher, **G. Sainath**, V.S. Srinivasan, E.I. Samuel, B.K. Choudhary, M.D. Mathew, T. Jayakumar, *Procedia Engineering* 55 (**2013**) 798-804. https://doi.org/10.1016/j.proeng.2013.03.334.

14. Molecular dynamics simulations of tensile behavior of copper, **G. Sainath**, V.S. Srinivasan, B.K. Choudhary, M.D. Mathew, T. Jayakumar, *Proc. of 4th Inter. Congress on Computational Mechanics and Simulation (ICCMS-2012)*, 10-12 Dec. **2012**, IIT-Hyderabad, Paper No. 78.

Date: 20-03-2018   (G. Sainath)
Place: Kalpakkam

2. Formation of pentagonal chains during the tensile deformation of BCC Fe nanowires, **G. Sainath**, B.K. Choudhary, *Conference on Emerging Materials (CEMAT)*, IISc-Bangalore, July 18-19, **2016** (Oral presentation).

3. Molecular dynamics simulations study on the uniaxial deformation behavior of BCC Fe containing twist grain boundaries, **G. Sainath**, B.K. Choudhary, T. Jayakumar, *5th International Congress on Computational Mechanics and Simulations (ICCMS-2014)*, 10-13 Dec. **2014**, SERC Chennai. https://doi.org/10.3850/978-981-09-1139-3_166.

4. Effect of orientation on deformation behavior of Fe nanowires: A molecular dynamics study, **G. Sainath**, V.S. Srinivasan, B.K. Choudhary, M.D. Mathew, T. Jayakumar, *58th DAE-SSPS, AIP Conference Proceedings* 1591 **(2014)** 1182-1184. https://doi.org/10.1063/1.4872896.

Workshops/Schools/Courses attended

1. BRNS School on "Computational Methodologies Across Length Scales" Aug 28 - Sept 09, **2017**, BARC, Mumbai.

2. GIAN Course on "Nonequilibrium Statistical Mechanics and Molecular Dynamics" Dec 5 -16, **2016**, IIT Kharagpur.

Publications not part of thesis

1. Double reorientation in <110> Cu nanowires, P. Rohith, **G. Sainath**, B.K. Choudhary, *Philosophical Magazine Letters* 97 **(2017)** 408-416. https://doi.org/10.1080/09500839.2017.1390618.

2. Size dependent deformation behaviour and dislocation mechanisms in <100> Cu nanowires, **G. Sainath**, P. Rohith, B.K. Choudhary, *Philosophical Magazine* 97 **(2017)** 2632-2657. https://doi.org/10.1080/14786435.2017.1347300.

3. Molecular dynamics simulation studies on the influence of aspect ratio on tensile deformation and failure behaviour of <100> copper nanowires, P. Rohith, **G. Sainath**, B.K. Choudhary, *Computational Materials Science* 138 **(2017)** 34-41. https://doi.org/10.1016/j.commatsci.2017.06.019.

4. Dependence of equilibrium stacking fault width on thickness of Cu thin films: A molecular dynamics study, P. Rohith, **G. Sainath**, B.K. Choudhary, *AIP Conference Proceedings* 1832 **(2017)** 080060. https://doi.org/10.1063/1.4980520.

5. Directional anisotropy of crack propagation along $\Sigma 3$ grain boundary in BCC Fe, **G. Sainath**, B.K. Choudhary, *Transactions of Indian Institute of Metals* 69 **(2016)** 525-530. https://doi.org/10.1007/s12666-015-0783-6.

6. Fatigue deformation of polycrystalline Cu using molecular dynamics simulations, **G. Sainath**, P. Rohith, B.K. Choudhary, *Transactions of Indian Institute of Metals* 69 **(2016)** 489-493. https://doi.org/10.1007/s12666-015-0823-2.

7. Unified description of tensile work hardening behaviour of P92 steel, E.I. Samuel, J. Christopher, **G. Sainath**, B.K. Choudhary, *Materials Science and Engineering A* 652 **(2016)** 92-98. https://doi.org/10.1016/j.msea.2015.11.028.

List of Publications

Peer reviewed journals

1. Twinning to slip transition in ultra-thin Fe nanowires, **G. Sainath**, B.K. Choudhary, *Physics Letters A* 382 **(2018)** 1047-1051. https://doi.org/10.1016/j.physleta.2018.02.007.

2. Atomistic simulations on ductile-brittle transition in <111> BCC Fe nanowires, **G. Sainath**, B.K. Choudhary, *Journal of Applied Physics* 122 **(2017)** 095101 [*This work has been chosen as the cover figure, issue 9, 07 September*]. https://doi.org/10.1063/1.4999090.

3. Formation of pentagonal atomic chains in BCC Fe nanowires, **G. Sainath**, B.K. Choudhary, *Materials Research Express* 3 **(2016)** 125022. https://doi.org/10.1088/2053-1591/aa50c1.

4. Influence of twist boundary on deformation behaviour of <100> BCC Fe nanowires, **G. Sainath**, B.K. Choudhary, *Philosophical Magazine Letters* 96 **(2016)** 469-476. https://doi.org/10.1080/09500839.2016.1257870.

5. Deformation behaviour of body centered cubic iron nanopillars containing coherent twin boundaries, **G. Sainath**, B.K. Choudhary, *Philosophical Magazine* 96 **(2016)** 3502-3523 [*It has been awarded the best paper for the year 2016 from IIM Kalpakkam chapter*]. https://doi.org/10.1080/14786435.2016.1240377.

6. Orientation dependent deformation behaviour of BCC iron nanowires, **G. Sainath**, B.K. Choudhary, *Computational Materials Science* 111 **(2016)** 406-415. https://doi.org/10.1016/j.commatsci.2015.09.055.

7. Molecular dynamics simulations on size dependent tensile deformation behaviour of [110] oriented body centered cubic iron nanowires, **G. Sainath**, B.K. Choudhary, *Materials Science and Engineering: A* 640 **(2015)** 98-105. https://doi.org/10.1016/j.msea.2015.05.084.

8. Molecular dynamics simulation studies on the size dependent tensile deformation and fracture behaviour of body centred cubic iron nanowires, **G. Sainath**, B.K. Choudhary, T. Jayakumar, *Computational Materials Science* 104 **(2015)** 76-83. https://doi.org/10.1016/j.commatsci.2015.03.053.

Manuscripts under preparation

1. Influence of size, shape and strain rate on the ductile-brittle transition in BCC Fe nanowires, **G. Sainath**, B.K. Choudhary, (Under preparation).

2. Effect of orientation on the fracture behaviour of BCC Fe nanowires, **G. Sainath**, B.K. Choudhary, (Under preparation).

Conference proceedings/presentations

1. Interesting observations on deformation behavior at nanoscale, **G. Sainath**, B.K. Choudhary, *Proceedings of International Conference on Electron Microscopy (EMSI)*, Mahabalipuram, 17-19 July, **2017**, pp. 305-307.

DECLARATION

I, hereby declare that the investigations presented in the thesis have been carried out by me. The work is original and has not been submitted earlier as a whole or in part for a degree/diploma at this or any other Institution/University.

(G. Sainath)

Date: 20-03-2018
Place: Kalpakkam

STATEMENT BY AUTHOR

This dissertation has been submitted in partial fulfilment of requirements for an advanced degree at Homi Bhabha National Institute (HBNI) and is deposited in the Library to be made available to borrowers under rules of the HBNI.

Brief quotations from this dissertation are allowable without special permission, provided that accurate acknowledgement of source is made. Requests for permission for extended quotation from or reproduction of this manuscript in whole or in part may be granted by the Competent Authority of HBNI when in his or her judgement the proposed use of the material is in the interests of scholarship. In all other instances, however, permission must be obtained from the author.

Date: 20-03-2018   (G. Sainath)

Place: Kalpakkam

plane. The deformation by slip observed at low strains is interesting as the slip is not observed in perfect <100> nanowire. This indicates that the presence of {100} twist boundary or initial dislocations in <100> BCC Fe nanowire changes the deformation mode from twinning to slip. The <110> BCC Fe nanowire containing a {110} twist boundary deforms by slip at all strains similar to that in perfect <110> nanowire.

CHAPTER 8 : Conclusions and future directions

This is the final chapter of the thesis. It outlines the important findings and observations on the deformation behaviour of BCC Fe nanowires/nanopillars. For further understanding of the deformation behaviour of BCC nanowires a few recommendations have been suggested for future studies.

ing a square cross-section width (d) of 8.5 nm has been created. Then the pillar is divided into two equal parts, lower and upper along the axis. Following this, the TBs were introduced by rotating one part of the crystal with respect to other by 180° around <112> axis. Using the same procedure, BCC Fe nanopillars containing one, two, three and five TBs perpendicular to the nanowire axis (<112>) have been created. This resulted in a twin boundary (TB) spacing of 8.5, 5.7, 4.2 and 2.8 nm, respectively. The MD simulation results at 10 K indicate that the TBs in BCC Fe nanopillars play a contrasting role under tension and compression. The deformation under tensile loading of perfect <112> as well as twinned BCC Fe nanopillars was dominated mainly by twinning mechanism with minor activity of full dislocations, while the compressive deformation was dominated by the slip of full dislocations. During the tensile deformation of twinned nanopillars, the twin-twin interactions produces mainly the <021> type twin intersections. It has been observed that the edge of the curved TB can acts as a source for the nucleation of full dislocations. The dislocation-TB interactions under the compressive loading revealed that the dislocations can either directly pass through the TB without any deviation in slip plane or it can transmit to a symmetrical slip plane in the neighbouring grain. The yield stress of twinned nanopillars under tensile loading is much lower than the perfect nanopillar and it varies marginally with TB spacing. On the other hand, the yield stress of twinned nanopillars under compressive loading is comparable to that of a perfect nanopillar and decreases with increasing TB spacing. This contrasting behaviour in yield stress is due to the repulsive force offered by TBs. Since the deformation under tensile loading is dominated by twinning, the TB offers negligible repulsive force on twinning partials. As a result, the yield stress varies marginally with TB spacing under tensile loading. In case of compressive loading, the TBs offers a strong repulsive force on full dislocations leading to significant variation of yield stress with TB spacing.

The role of {100} and {110} twist boundaries on the tensile deformation of BCC Fe nanowires has been studied at 10 K. Twist boundaries have been obtained by dividing the nanowire into two grains along the length and rotating the upper and lower grains by an angle of $+2^o$ and -2° around the axis in both <100> and <110> orientations. This resulted in {100} twist boundary in <100> nanowire and {110} twist boundary in <110> nanowire. Following equilibration of this nanowires, a screw dislocations network formed at the boundary. The dislocation network at {100} twist boundary had a square structure and contains a junctions formed by four <100> type dislocation segments. On the other hand, the dislocation network at {110} twist boundary had a hexagonal structure and contains a junctions formed by two 1/2<111> dislocations and one <100> dislocation. The MD simulations results on the tensile deformation of <100> BCC Fe nanowire containing a {100} twist boundary indicate that the deformation proceeds by slip at low plastic strains followed by twinning at high strains. Further, the nanowire doesn't undergo full reorientation and fail by shear along the {112}

The results indicate that the <111> BCC Fe nanowires exhibit ductile to brittle transition (DBT) with decreasing temperature. The nanowires with d = 8.5 nm, yield through the nucleation of a sharp crack and fails in brittle manner at low temperatures (10-375 K). On the other hand, nucleation of multiple 1/2<111> dislocations followed by significant plastic deformation leading to ductile failure has been observed at high temperatures (450-1000 K). At the intermediate temperature of 400 K, the nanowire yields through the nucleation of crack, but fails in ductile manner. The accumulated plastic strain is negligible at low temperatures followed by a sharp increases in the temperature range 375-500 K. Beyond 500 K, it remains nearly constant. These results indicate that <111> BCC Fe nanowires undergo DBT at 400 K. Further, it has been observed that the transition temperature is sensitive to nanowire shape, size and strain rate. The simulations performed on nanowire of circular cross-section with diameter of 8.5 nm shows DBT at 550 K, which is higher than that observed for the square cross-section nanowire. Similarly, the simulations carried out on small (d = 2.85 nm) and large (17.13 nm) size nanowires indicates that the transition temperature increases with increasing size. For nanowire with d = 2.85 nm, the transition has been observed at 350 K, whereas for nanowire with d = 17.13 nm, it has been observed at 450 K. By performing simulations at a higher strain rate of 1×10^9 s^{-1} for nanowire size of 8.5 nm, it has been observed that the DBTT increases to 400 K. The DBTT and it's change with respect to size, shape and strain rate in BCC Fe nanowires has been explained based on the relative variations in yield and fracture stresses as a function of temperature.

CHAPTER 7 : Influence of twin and twist boundaries on deformation behaviour of BCC Fe nanopillars

The grain boundaries play an important role in controlling the strength and deformation behaviour of polycrystalline materials. It has been shown that the FCC nanopillars containing series of twin boundaries (TBs) exhibit higher strength and ductility as compared to their perfect counterparts. As a result, the twinned FCC nanopillars have attracted considerable attention for research and significant progress has been made in this direction. However, little attention has been paid towards understanding the role of TBs in BCC nanopillars. In view of high stacking fault energy of BCC metals, it is difficult to grow twinned nanopillars using experimental techniques. In the present study, an attempt has been made to examine the deformation behaviour of BCC Fe nanopillars containing twin boundaries. In addition, the role of different twist boundaries in BCC Fe nanowires has been investigated.

Twinned BCC Fe nanopillars have been created by the following procedure. Initially, BCC Fe nanopillar oriented in <112> axial direction with {110} and {111} side surfaces hav-

sizes followed by saturation at larger sizes. Contrary to this, flow stress at different strains displayed a rapid decrease with increase in size for small size nanowires followed by saturation at larger sizes.

CHAPTER 5 : Twinning to slip transition and formation of pentagonal atomic chains in ultrathin <100> BCC Fe nanowires

This chapter deals with the combined influence of size and temperature on deformation and failure behaviour of ultrathin <100> BCC Fe nanowires. MD simulations have been performed on different nanowire size in the range 0.404-3.634 nm at temperatures ranging from 10 to 900 K. It has been observed that nanowires with cross-section width (d) less than 3.23 nm deform by twinning at low temperatures, while full dislocation slip has been observed at high temperatures. The deformation mechanisms map separating the two different regions of twinning and slip modes of deformation with respect to size and temperature has been obtained. It indicates that the temperature at which the nanowires show twinning to slip transition increases with increase in nanowire size. In other words, at each temperature, there is a critical size below which twinning cannot occur. Above d = 3.23 nm, <100> BCC Fe nanowires deform by twinning irrespective of temperature. The different modes of deformation are also reflected appropriately in the respective stress-strain behaviour of the nanowires. Interestingly, at high temperatures where the nanowire deform by dislocation slip, the formation of pentagonal atomic chains (PAC) have been observed in the necking region. The pentagonal atomic chains were found to be highly stable over large plastic strains and contribute to high ductility in <100> BCC Fe nanowires. In small size nanowires with d = 0.404 and 0.807 nm, the complete transformation to the pentagonal structure has been observed at high temperatures. The formation of PACs is not been observed in nanowires that deform by twinning. The formation of pentagonal atomic chains in BCC Fe nanowires is interesting because it exhibits a five-fold symmetry with respect to the nanowire axis.

CHAPTER 6 : Ductile-Brittle transition in <111> BCC Fe nanowires

It is well known that BCC materials are generally difficult to deform at low temperatures leading to brittle fracture, whereas at high temperature, they fail by ductile manner. As a result, most of the BCC materials show a ductile to brittle transition with respect to temperature. In this context, it is important to examine the possibility of ductile to brittle transition temperature (DBTT) in BCC Fe nanowires. In order to investigate the DBTT, the tensile deformation and failure behaviour of <111> BCC Fe nanowires has been studied as a function of temperature in the range 10-1000 K for nanowires with d = 2.85, 8.5 and 17.13 nm.

derstanding of size effects in BCC Fe nanowires. MD simulations have been performed at 10 K on <100> and <110> nanowires with cross-section width (d) varying from 1.42 to 24.27 nm. These two orientations have been chosen mainly because, the <100> and <110> nanowires represent two different modes of deformation i.e. twinning and dislocation plasticity, respectively.

MD simulation results on <100> BCC Fe nanowires indicated that the deformation is dominated by twinning mechanism irrespective of size. However, with increasing size, few important differences have been observed with respect to defect nucleation and twin growth. In small size nanowires with d $\leq$ 11.42 nm, the nucleation of a single twin embryo has been observed. Following this, the twin embryo grows systematically along the nanowire axis and completely sweeps the nanowire leading to reorientation from initial <100> to <110> orientation. With increasing strain, the reoriented nanowire again undergo an elastic deformation which results in the occurrence of a second elastic peak in the stress-strain curves. Interestingly, the plastic deformation in the reoriented nanowire occurs by the slip of 1/2<111> full dislocations till its failure by ductile mode. On the other hand, in nanowires with d > 11.42 nm, the yielding occurs by the nucleation of multiple twin embryos on different {112} planes. With increasing deformation, the growth of multiple twins facilitate the twin-twin interactions thereby restricting the the twin growth process in large size nanowires. As a result, the large size nanowires are not able to undergo reorientation. With increasing strain, the twin-twin interactions leads to crack nucleation and the nanowires fail by cleavage along {112} plane. The absence of reorientation and failure by cleavage in large size nanowires results in low ductility compared to small size nanowires. The values of Young's modulus, yield stress and twin propagation stress also exhibit a transition at d = 11.42 nm. The values decreases rapidly with increasing size up to 11.42 nm followed by gradual decrease approaching towards saturation at larger sizes.

Contrary to deformation of <100> nanowires, the simulation results on <110> orientation indicated that the deformation is governed by the slip of 1/2<111> full dislocations irrespective of nanowire size. The yielding in all the nanowires occurred by the collective nucleation of dislocations loops followed by accumulation of large number of straight screw dislocations. However, few important differences have been noticed in large and small size nanowires. In large size nanowires of d > 11.42 nm, slip steps having curved profile have been observed thus providing an evidence for cross-slip. On the other hand, curved slip steps have not been observed in nanowires with d < 11.42 nm. Further, an increase in number of slip steps and slip bands has been observed with increasing size. Following plastic deformation, all the nanowires fail by ductile mode. Unlike <100> BCC Fe nanowires, Young's modulus and yield strength in <110> nanowires exhibited a rapid increase with increasing size for small

compressive loading has been applied for <100> and <110> orientations. All the nanowires had a cross-section of width (d) = 8.5 nm.

The elastic deformation of nanowires of different orientations has been analysed using the radial distribution function (RDF) as a function of strain. It has been observed that during elastic deformation, the peaks in the RDF get split into two independent secondary peaks and with increasing elastic strain, one peak shift towards higher distances and other towards lower distance. At the onset of plastic deformation, all the secondary peaks merged with primary peaks. Following elastic deformation, the plastic deformation mechanisms vary significantly with crystal orientation. Under tensile loading, the <100>, <112> and <102> nanowires deformed predominantly by twinning, whereas <110> and <111> nanowires deformed by slip of dislocations. The deformation by twinning in nanowires has led to reorientation within the twinned region. The orientation dependent deformation behaviour has been explained by the twinning-antitwinning asymmetry of 1/6<111> partial dislocations on {112} planes. Based on this results, a simple model of twin nucleation and growth has been presented. BCC Fe with <100> orientation exhibits the lowest Young's modulus (164 GPa) and yield strength (12.3 GPa), while the <111> orientation showed the highest modulus (288 GPa) and yield strength (27.2 GPa). The modulus and yield strength of other orientations fall in between of these two orientations. In general, the orientations that deform by twinning exhibit lower values of yield strength than the nanowires that deform by slip. The compressive loading applied on <100> and <110> orientations indicated that the <100> nanowire (which deformed by twinning under tensile loading) deform by dislocation slip, while the <110> nanowire (which deformed by dislocation slip under tensile loading) deformed by twinning. No significant influence of loading mode on Young's modulus has been noticed. The yield strength of <100> orientation has been observed to be higher in compression than tension, while <110> orientation showed higher strength in tension than in compression. These results indicate that <100> and <110> orientations display opposite tension-compression asymmetry in deformation mechanisms as well as yield strength.

CHAPTER 4 : Size dependent deformation and failure behaviour of <100> and <110> BCC Fe nanowires

Size plays an important role on the mechanical properties and the associated deformation mechanisms of materials at nanoscale. A thorough literature survey indicates that most of the studies with respect to size effects were focussed mainly on FCC nanowires such as Au, Ag and Cu, while no attention has been paid to BCC nanowires. However, a few experimental studies exist in Mo, W and Nb micropillars. In this backdrop, the present chapter provides the detailed un-

CHAPTER 1 : Introduction

In introduction, a brief overview of the nanowires and their applications, fundamentals of mechanical properties such as strength and modulus, plastic deformation mechanisms like slip, twinning and dislocations and fracture behaviour are presented. The literature status with respect to deformation and failure mechanisms of FCC/BCC nanowires from experimental as well as simulations point of view is reviewed. Following this, the motivation and scope of the thesis have been brought out.

CHAPTER 2 : Molecular dynamics simulations : Methodology and post-processing

In this chapter, the details of computational and analytical techniques used in the present study have been presented. Theory of MD simulations and the embedded atom method (EAM) potentials for BCC Fe have been introduced. The details of integration algorithms, thermostats or ensemble, and boundary conditions used in MD simulations have been presented. The different loading procedures followed in the present study along with the calculation of stress have been described. The defect analysis using different parameters such as radial distribution function (RDF), centro-symmetry parameter (CSP) and common neighbour analysis (CNA) are reviewed. Finally, the details of LAMMPS package used to carry out MD simulations and pre-and post-processing packages such as Atomsk, AtomEye, OVITO, and DXA have been discussed.

In this thesis, the nanowires have been simulated by choosing the periodic boundary conditions along the axis direction, while other two directions were kept free. In case of nanopillars, no periodic boundary conditions have been used in any direction. All the nanowires/nanopillars had a square cross-section with length (l) twice the cross-section width (d). A constant engineering strain rate of 1×10^8 s^{-1} along the nanowire length (z) direction was applied in all the simulations.

CHAPTER 3 : Influence of orientation and mode of loading on deformation behaviour of BCC Fe nanowires

Crystal orientation plays an important role on the strength and deformation mechanisms of single crystals. Although this problem has been well understood in bulk scale and also in FCC nanowires, it is poorly addressed in BCC nanowires. In the present chapter, the effect of orientation on the deformation behaviour of BCC Fe nanowires has been investigated at 10 K. BCC Fe nanowires with <100>, <110>, <111>, <112> and <102> orientations have been considered under tensile loading. IN order to examine the influence of loading mode, the

Synopsis

Nanowires are special class of quasi one-dimensional nanostructures with lateral dimensions much smaller than their length. In recent years, metallic nanowires have attracted a considerable attention due to their unique properties and potential applications in future nano/micro electro-mechanical systems (NEMS/MEMS). Due to high surface area and controlled defect density, nanowires exhibit superior electrical, optical, and mechanical properties compared to their bulk counterparts. In particular, body centered cubic (BCC) Fe nanowires, which possesses good magnetic properties, find applications in data/memory storage devices, high-density recording media, permanent magnets, spin electronics, magnetic field sensing, enhancement agents for magnetic resonance imaging (MRI), medical sensors and other smart devices. Improving the durability and reliability of these devices requires fundamental understanding of mechanical properties and associated deformation mechanisms.

Designing and performing mechanical testing of nanowires at different sample sizes, temperatures, and strain rates require sophisticated and innovative testing methods. Therefore, there is a need to explore the alternative theoretical or computational methods. With rapid progress of computational capability and the availability of reliable inter-atomic potentials, molecular dynamics (MD) simulations have become a major tool to probe the mechanical properties and associated deformation mechanisms of nanowires. In the last decade, many MD simulation studies have been provided valuable and reliable information about the deformation behaviour of face centered cubic (FCC) nanowires. However, there is a lack of understanding in BCC nanowires from both experimental as well as atomistic simulations. In this context, the present thesis focuses towards understanding the deformation behaviour of BCC Fe nanowires using MD simulations. The influence of various factors such as the crystallographic orientation, nanowire size, cross-section shape, mode of loading (tension/compression), temperature, strain rate and the presence of twist and twin boundaries have been investigated. The highlights of the thesis are tension-compression asymmetry in deformation mechanisms, reorientation of the nanowires below certain size, formation of pentagonal atomic chains in ultrathin sizes, ductile-to-brittle transition, absence of twinning in presence of dislocations and strengthening due to twin boundaries. The thesis comprises of eight chapters and the content of each chapter is described briefly in the following;

Contents

List of Tables

xxv

List of Figures

signed 1/6<111> as the Burgers vector of partial/twinning dislocations in BCC Fe.

allel computers. Further, LAMMPS can be used to create some simple geometries like BCC, FCC and HCP lattices. In the present thesis, all the molecular dynamics simulations have been carried out in LAMMPS package installed in 134 Node HPC cluster at IGCAR. The maximum size of the system employed in the present thesis contains close to 2.5 million atoms.

In order to visualize the defects by implementing the above mentioned techniques, Ju Li [102] has developed a visualization tool known as AtomEye. It is a free atomistic 3D visualization software and it shows the atoms as spheres and bonds as tubes/cylinders. The main functions of the AtomEye are 3D navigation with parallel and perspective projections, coordination number calculations, colour-coding of atoms according to user-defined parameters such as CNA or CSP, cutting of planes for clear defect visualization and calculating the distance/angle between any two/three atoms. It produces high quality JPEG, PNG and EPS images and also supports animation scripting. AtomEye can handle more than one million atoms on a simple desktop computer. In the present work, the AtomEye package has been extensively used for the visualization of atomic snapshots. However, the AtomEye is not capable of determining the type of defects i.e., dislocation, vacancy, grain boundary, etc. or any quantitative information like density of defects or the Burgers vector of a dislocation. In this backdrop, Stukowski [103] developed a Open Visualization Tool (OVITO) which extract dislocation lines and their Burgers vectors, and calculates dislocation density, stacking fault and twin boundary densities. Like AtomEye, OVITO is also a 3D visualization open-source software with graphical user interface. OVITO post-processes the simulations data using various analysis techniques. OVITO analyses for dislocations according to dislocation extraction algorithm (DXA) [104]. In addition to dislocation analyses, the main functions of OVITO are calculation and visualization of displacement vectors obtained from the differences between two states of the system, slicing and cutting of atomic structures, selects atoms based on defined criteria, perform common neighbour analysis, coordination number analysis, calculate radial distribution function and other atomic level strain tensors.

In the present work, the Burgers vectors of full dislocations were determined using Dislocation extraction algorithm (DXA) as implemented in OVITO. However, the identification of Burgers vector of partial/twinning dislocations gliding on the twin boundary in BCC system is challenging. This is mainly because the Burgers circuit of twinning dislocation passes through the twin boundary at which the crystal orientation changes. Due to this difficulty, the DXA or OVITO packages failed to detect the Burgers vectors of partial dislocations and the type of dislocation intersections. Based on the experimental observations [105], we have as-
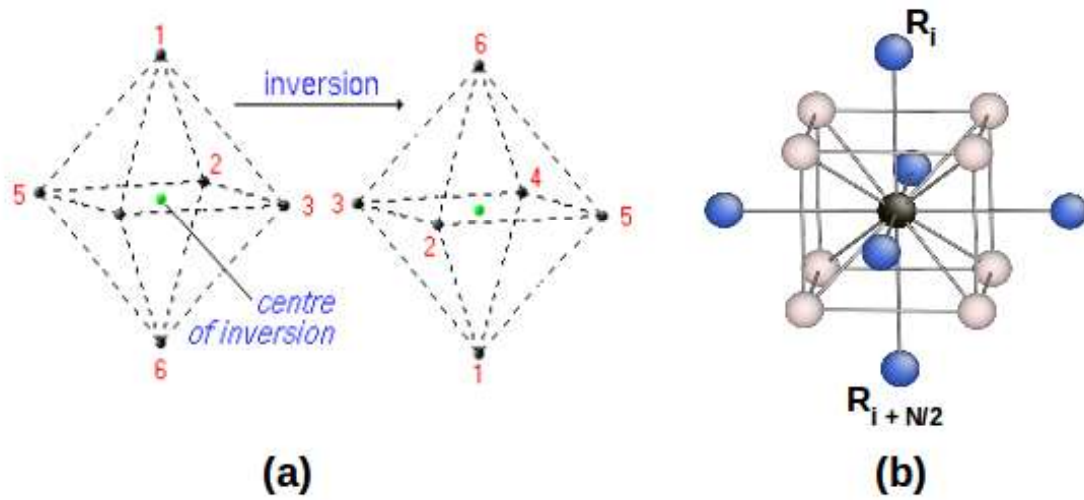
Figure 2.8: (a) A typical inversion symmetry of an atom in a periodic lattice and (b) vectors connecting the pair of atoms to their reference atom in BCC lattice.

measures the departure from inversion symmetry and practically, it can be computed for every atom in a system. For an atom in a perfect lattice, the value of CSP is 0 and it still lies close to zero 0 even for small thermal fluctuations [101]. However, in the presence of a defect, the symmetry is broken, and the value of CSP is a positive quantity. Depending on the crystal structure, the CSP has distinct values for dislocations, stacking faults, point defects and surfaces [101]. Therefore, using an imaging software that colours the atoms according to their CSP values, the different defects can be visualized more clearly, while hiding the atoms having the CSP values close to zero. Thus, the CSP can be used to identify a local lattice disorder around an atom. In the present work, the CSP has been used to detect point defects, partial/twinning dislocations, full dislocations, twin boundaries and other grain boundaries observed during the deformation of BCC Fe nanowires.

2.9 LAMMPS, AtomEye and OVITO

In order to carry out molecular dynamics simulations, there exist many open source software packages such as GROMACS, *DL_POLY* and LAMMPS. The most widely used package for performing molecular dynamics simulations of solid state systems is LAMMPS, stands for Large scale Atomic/Molecular Massively Parallel simulator developed by Plimpton [94] at Sandia national lab. It is an open-source code developed to run efficiently on single or par-

The CNA parameter is sensitive to the cut-off distance. If we chose high cut-off distance, it increases the computation time and small cut-off distance may not enclose sufficient neighbours. Therefore, the cut-off distance must be chosen in such a way that the appropriate nearest neighbours should be found within this distance. Generally within the selected cut-off distance, 12 nearest neighbours should be found for FCC and HCP structures, while for BCC structure, 14 nearest neighbours should be present. For this purpose, the cut-off distance should lie halfway between the first and second shells of for the FCC lattice , whereas for BCC, it falls between the second and third shell. Accordingly, the formulas used to obtain a good cut-off distance (r_c) for calculating CNA parameter are as follows [94]

$$r_c^{fcc} = \frac{1}{2}\left(\frac{\sqrt{2}}{2} + 1\right)a \approx 0.8536a, \tag{2.29}$$

$$r_c^{bcc} = \frac{1}{2}\left(\sqrt{2} + 1\right)a \approx 1.207a, \tag{2.30}$$

where a is lattice parameter of a respective FCC/BCC lattice.

In the present analysis, CNA pattern has been used to distinguish the atoms in crystalline, non-crystalline and pentagonal or icosahedral environment. Since the CNA parameter distinguishes the atoms of different crystalline structures, it can be used to identify the stacking faults in FCC lattice and also the twin boundaries in BCC lattice.

2.8.3 Centro-symmetry parameter

In order to identify the defects with even more precision, Kelchner et al. [101] proposed a parameter based on the inversion symmetry of an atom (Figure 2.8a). In a centro-symmetric lattice such as BCC/FCC, each atom has a pair of equal and opposite bonds with its nearest neighbours. Under homogeneous elastic deformation, these bonds may change direction and/or length, but they remain equal and opposite. However, when a defect is present, this relation no longer holds good. Kelchner et al. [101] defined centro-symmetry parameter (CSP) for each atom as follows

$$CSP = \sum_{i=1}^{N/2} |R_i + R_{i+\frac{N}{2}}|^2, \tag{2.31}$$

where R_i and $R_{i+\frac{N}{2}}$ are the vectors or bonds from the central atom to a particular pair of nearest neighbours and N is the coordination number. The vectors of a pair of atoms from the central atoms is shown in Figure 2.8b for a typical BCC lattice. For any given atom, this parameter

of common neighbours for a pair of atoms can be summarized in a triplet ijk, where i represents the number of common neighbours of a pair, j indicates the number of possible geometrical bonds among the common neighbours and, k represents the number of bonds in the longest continuous chain of bonds which can be formed from these common neighbours [98, 99]. The combination of all triplets is called signature and represents a certain geometric structure.

As an example, the common neighbour analysis of bulk FCC structure is illustrated in Figure 2.7. It can be seen that any atom in perfect FCC structure (for example red atom in Figure 2.7a) has 12 nearest neighbours (green atoms). With each of nearest neighbours, the red atom shares 4 common neighbours, i.e. the neighbours common to pair of atoms containing the original red atom within this shell (e.g. pair of red atoms in Figure 2.7b and c) and , therefore $i = 4$. Out of this four common neighbours, only two geometrical bonds are possible i.e. $j = 2$. This two bonds are the longest possible chains among the common neighbours and the number of bonds in this chains is one, i.e. $k = 1$. Therefore, an atom in bulk FCC structure has a signature of 421. Since all 12 bonds of each atom are the same, a local environment with 12 nearest neighbours and signature of 421 can be identified as FCC structure. Similarly, an atom in a BCC crystal has 8 bonds with 666 signature (first shell) and 6 bonds with 444 signature (2nd shell). In a pentagonal chains, a central atom has 12 bonds with a signature of 555. The complete list of signatures for different structures and their surfaces can be found in the work of Cleveland et al. [100].
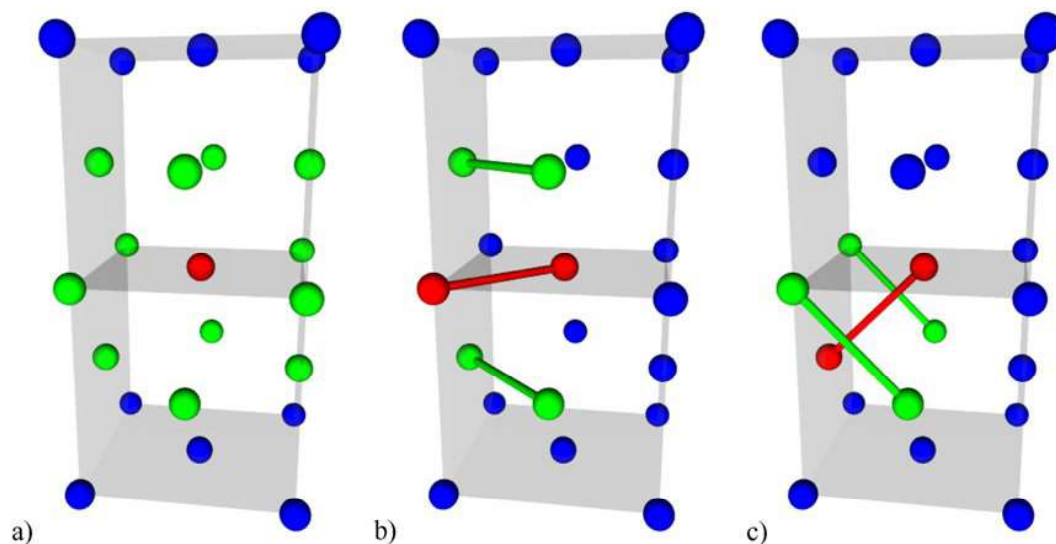
Figure 2.7: Methodology of common neighbour analysis in FCC structure [99]: (a) two adjacent FCC unit cells, where a reference atom is marked in red and its 12 nearest neighbours in green, (b) a typical pair with reference atom (red) with their four common neighbours coloured in green, and (c) another pair with a reference atom (red) and their common neighbours (green).
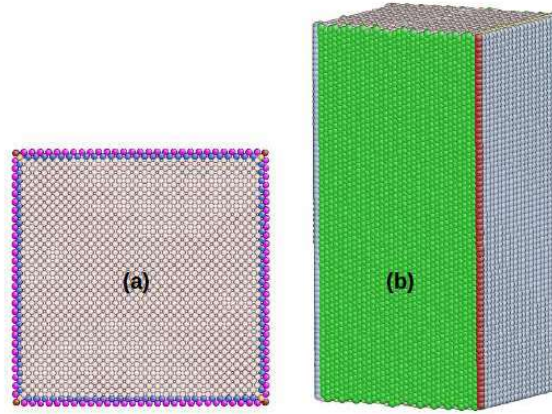
Figure 2.6: Colour coding of atoms in nanowire according to their coordination number. (a) cross-sectional view and (b) side view of a nanowire. It can be seen that the surface and corner atoms have a different coordination number as compared to the perfect interior atoms. Similarly, in (b) the surfaces of different orientation also have different coordination number.

Generally while calculating the coordination number of an atom, only the first nearest neighbour shell is taken into account. However, in BCC lattice the next or second nearest neighbour shell is at distance of 'a' from the reference atom, which is only a little away from the first nearest neighbour shell ($a - 0.866a = 0.134a$). For this reason, sometimes the second nearest neighbours were also included while calculating the coordination number of an atom in BCC lattice. This makes the new coordination number of an atom in BCC lattice to 14. In the present study, the coordination number of an atom in BCC lattice has been taken as 14. This problem doesn't arise in FCC lattice because the second nearest neighbours shell is at a distance of 'a', which is significantly away from the first nearest neighbours shell. Therefore, the coordination number of an FCC lattice is always 12.

However, the analysis of coordination number cannot distinguish the difference between FCC and HCP phases, and thereby the stacking faults in FCC lattice. This is mainly because both FCC and HCP have the same coordination number of 12. Similarly, the twin boundaries in BCC lattice were also indistinguishable from the perfect atoms. This warrants the need of a new parameter.

2.8.2 Common neighbour analysis

The common neighbour analysis (CNA) is useful parameter for obtaining local crystal structure around an atom. This parameter is obtained based on the detailed geometric analysis of a set of common neighbours of two atoms within a specific cut-off distance [98]. The analysis of a set

51

2.8   Post-processing

Molecular dynamics simulations generates vast amount of data which needs to be processed in order to make meaningful conclusions. The data processing ranges from individual atoms to the group of atoms. Various techniques have been developed and reported in the literature to distinguish the atoms sitting on the perfect lattice from that on the defect regions. Different parameters such as potential energy, coordination number, centro-symmetry parameter and common neighbour analysis have been utilised in post-processing techniques. These parameters basically separates the defects such as vacancies, dislocations, stacking faults, surfaces and other structural features from the perfect regions. In the present work, mainly the coordination number, centro-symmetry parameter and common neighbour analysis have been used. The basic principle behind each of these techniques is briefly described in the following;

2.8.1   Coordination number

In any periodic lattice, the coordination number for particular atom is defined as the number of nearest neighbours in all directions. In BCC lattice, each atom is bonded to eight nearest neighbours at a distance of $\sqrt{3}a/2$ or $0.866a$, where a is the lattice parameter. Therefore, the coordination number of an atom in BCC lattice is 8. Similarly, in FCC lattice each atom is surrounded by 12 nearest neighbours at a distance of $a/\sqrt{2}$ or $0.707a$, thereby having a coordination number of 12. The atoms in HCP lattice have a coordination number of 12.

The atoms with coordination number that deviates from the perfect lattice are generally considered as defects or surfaces. Therefore, by colour-coding the atoms according to their coordination number, the defects can be distinguished from the perfect lattice and also the BCC phase from FCC or HCP phase. Further, the coordination number can also be used to differentiate between the surfaces of different orientations. As an example, Figure 2.6a shows a cross-sectional view of a BCC Fe nanowire, where atoms are colour coded according their coordination number. It can be seen that the surface and corner atoms have a different coordination number compared to the perfect interior atoms. Similarly, Figure 2.6b shows the side view of a nanowire, which has a side surfaces of {110} and {112} orientation coloured as green and grey, respectively. This indicates that the coordination number colouring clearly distinguishes the surfaces of different orientations. In the present work, the coordination number colouring has been extensively used to identify the changes in surface structure of the nanowires during tensile/compressive deformation.

imposes an inherent limitations on time-step. As discussed earlier, the typical time-steps used in MD simulations is in the range of 1-5 fs. With these time steps, the physical time scales accessible in MD simulations is in the order of few hundred nanoseconds ($\sim 10^5 - 10^7$ MD steps) [93]. Like experiments, if we use a strain rate of 10^{-3} s^{-1}, it takes unrealistically large MD steps ($\sim 10^{15}$) even to produce a small strain of 0.001. At such large MD steps, the numerical trajectory of MD simulations may not follow the true trajectory of the system (numerical instability). Therefore, at present the experimental strain rates are not accessible in MD simulations. To induce an appreciable strain without any divergence in the trajectories, the strain rate should be in the range of 0.000001 - 1 ps^{-1} i.e $10^7 - 10^{12}$ s^{-1}. In the present investigation, all the simulations have been carried out at a constant strain rate of 1×10^8 s^{-1}.

2.7   Definition of stress and strain

Stress and strain are two important parameters in order to understand the materials deformation behaviour. In continuum mechanics, stress is defined as the force acting per unit area. In atomistic systems, the stress (σ) is calculated using the Virial definition, which takes the form [96, 97]

$$\sigma_{\alpha\beta} = \frac{1}{V} \left[\frac{1}{2} \sum_i^N \sum_{j \neq i}^N F_{ij}^\alpha r_{ij}^\beta - \sum_i^N m_i v_i^\alpha v_i^\beta \right], \tag{2.27}$$

where N is the total number of atoms, V is the volume of the nanowire or simulation cell, r_{ij}^β is the distance between atoms i and j along the direction β, F_{ij}^α is the force between atoms i and j along the direction α, m_i and v_i are the mass and velocity of particle i, and the indices α and β denote the Cartesian components and takes the values of x, y and z. The first term in the above equation is due to the inter-atomic force (potential energy) and the second term is due to thermal vibrations (kinetic energy), which becomes important with increasing temperature. This atomistic definition of stress is equivalent to the continuum Cauchy stress.

The strain (ε) has been obtained as the relative change in the length of the nanowire which gives

$$\varepsilon = \frac{l - l_0}{l_0}, \tag{2.28}$$

where l is the instantaneous length of the nanowire and l_0 is the initial length. This definition of stress and strain has been used in the present work to determine the stress-strain response of the nanowires under different loading conditions.

49

remapped into the simulation box, whenever the box dimensions got changed. For compressive loading, the box dimensions have to be reduced and this can be achieved by reversing the sign of strain rate ($\dot{\varepsilon}$) in Equation 2.26.

Method-2 : In this method, the simulation box is divided into three regions, two fixed regions acts like grips, and one active region as shown in Figure 2.5. Following this, the deformation is applied by fixing one end of the nanowire (mostly the bottom) and then moving the other end (top region) at a constant velocity. To catch the velocity of top region, the atoms in the active region have been given a ramp velocity profile that varied linearly from zero at the bottom region to a maximum value at the top region as clearly shown in Figure 2.5. The effective strain rate in this procedure can be obtained by the dividing the maximum velocity with the original box length. This process closely follows the experimental procedure in which the wire is clamped at two points and pulled apart.
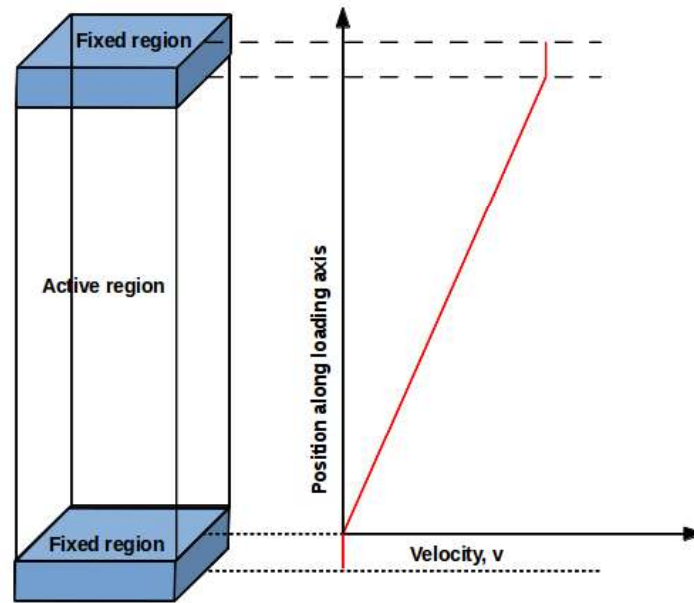
Figure 2.5: Displacement controlled loading of a nanopillar. The tensile/compressive loading is implemented by fixing the bottom region of the nanowire and then moving the top region at a constant velocity. The velocity profile of atoms in different regions/groups of the nanowire is provided as a function of their positions.

The important difference between the above two methods are, in method -1, only the atomic coordinates are remapped without altering the velocities, while in method-2, the moving boundaries can add a velocity component to the atoms.

Irrespective of loading methods, the strain rates used in MD simulations are extremely high ($\sim 10^6 - 10^{12}$ s^{-1}). This is mainly because the integration algorithms in MD simulations

system is ready to carry out loading simulations. The simulations at each temperature have been repeated five times, with a different random number seed for velocity distribution each time.

2.6   Tensile/compressive loading and strain rates

In molecular dynamics simulations, there are different methods of performing tensile or compression tests. The methods used in the present work are described below

Method-1: In this method, the simulation box length is changed uniformly along the loading axis as shown in Figure 2.4. The box length (L_i) as a function of time is varied as

$$L_i(t) = L_{i0}(1 + \dot{\varepsilon}t), \tag{2.26}$$

where $i = x$ or y or z, L_{i0} is the original box length along the direction i, $\dot{\varepsilon}$ is the strain rate and t is the elapsed time. It indicates that the box length changes linearly from initial value to a specified final value and this results in deforming the box at a constant engineering strain rate ($\dot{\varepsilon}$). If one dimension of the box is increased according to Equation 2.26, then the length in
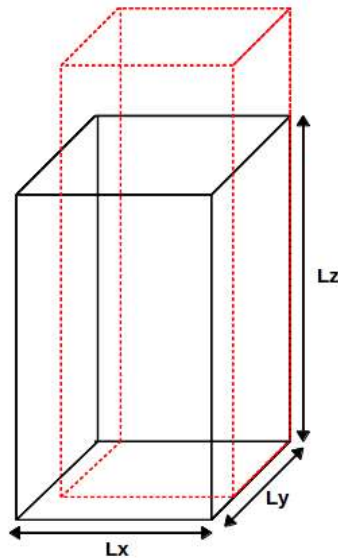
Figure 2.4: Applying the tensile/compressive deformation by uniformly deforming or changing the simulation box dimensions at constant volume

other two directions is varied in such a way that the simulation box volume remains constant during the simulations (Figure 2.4). Further, the coordinates of atomic positions have been

be generated. In order to maintain the continuity across the periodic boundary conditions, the care must be taken such that the size of the nanowire in any direction is an integer multiple of lattice spacing in that particular direction. In the present study, single crystal nanowires have been generated using the LAMMPS package [94] and also recently developed pre-processing software, Atomsk [95]. LAMMPS allows the user to directly define three crystal directions to align with the global simulation coordinate system.

In order to generate a twist or twin boundary, the nanowire has been divided into two parts lower and upper, along its axis. Following this, the specified boundary has been created by rotating one part of the crystal with respect to other by a required angle around a specific axis. This operations has been performed using Atomsk software. Similarly, a polycrystalline materials with random grain boundaries can be generated using Voronoi tessellation.

2.5 Equilibration

The created initial structure of the system may not be in a minimum energy configuration, i.e. the atoms may be too close to each other, for example at grain boundaries. Therefore, we need to obtain a system which is a minimum energy configuration. The minimum energy configuration can be obtained by adjusting the atomic coordinates from their original position and then calculating the total energy of the system. This process has been repeated iteratively until we get a minimum energy state. Therefore, the objective function to be minimized is the total potential energy of the system as a function of atomic coordinates. In the present investigation, the energy minimization was performed by a conjugate gradient (CG) method to obtain a relaxed structure with equilibration atomic positions corresponding to the nanowire/nanopillar. The minimization has been carried out until the energy change between two successive iterations divided by the initial energy is less than 10^{-6} (stopping criterion).

Following energy equilibration, we need to perform thermal equilibration in order to prepare the system at a required temperature. For this purpose, all the atoms have been assigned initial velocities according to the Gaussian distribution. Following this, the system was thermally equilibrated to a required temperature for 125 ps. The temperature is controlled with Nose-Hoover thermostat with a damping constant of 500 fs for all temperatures. This value of damping constant has ensured that the temperature fluctuations are always lower than 1% during simulations irrespective of test temperature. Following thermal equilibration, the

strained dimensions can be simulated by choosing the periodic boundary conditions along that particular dimension. Therefore, the conditions of a nanowire have been simulated by choosing periodic boundary conditions along the length, while the remaining directions have been kept free (Figure 2.3a), which mimics the surfaces. Similarly, choosing the free boundary conditions in all three directions simulates the conditions of a nanopillar which has $l \sim d$ (Figure 2.3b). The nanofilm has negligible thickness compared to other two dimensions and this geometry can be simulated by imposing the free boundary conditions along the thickness direction, while keeping the periodic boundary conditions in other two directions (Figure 2.3c).
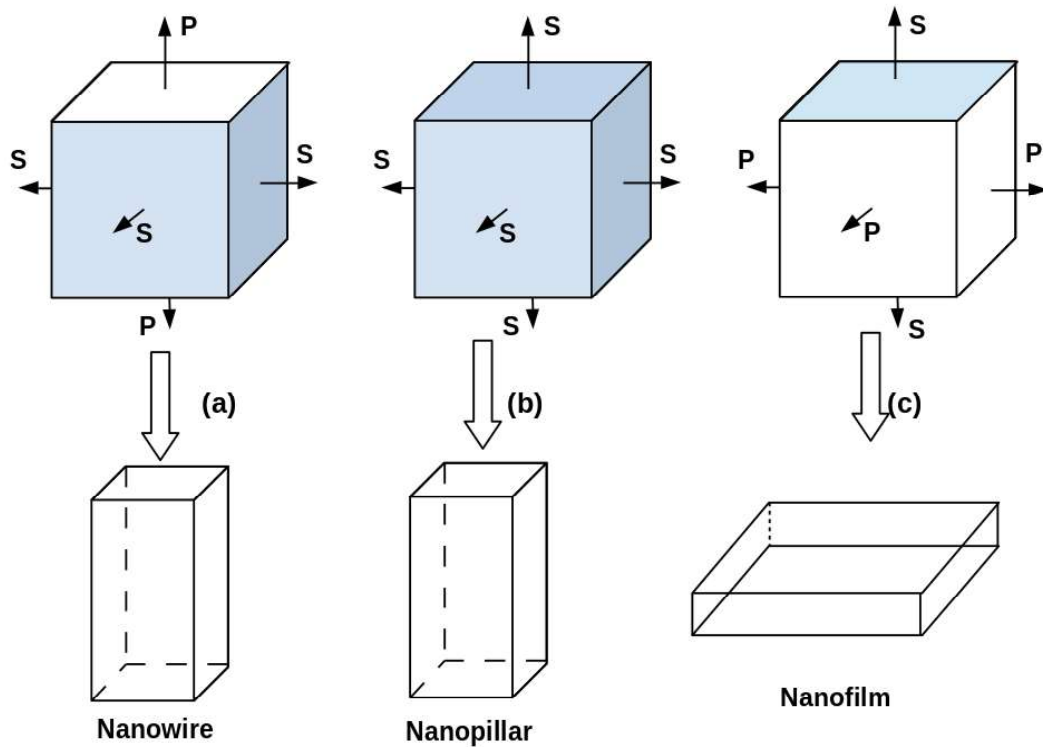
Figure 2.3: Boundary conditions used for different geometries with free surfaces (a) nanowire geometry, (b) nanopillar geometry and, (c) nanofilm geometry.

2.4   Pre-processing

In order to perform MD simulations on the required system (in the present case nanowires), the atomic positions of the system needs to be known. To obtain the atomic coordinates, different parameters such as lattice constant, lattice type, and lattice orientations are needed. The single crystal nanowires are the easiest and simplest to generate. Once the atomic positions of a basic unit cell are known, the unit cell can be duplicated in all directions to get the nanowire of required size. Similarly by rotating this basic unit cell, the nanowire of required orientation can

minimum image convention. According to this convention, any atom interacts with surrounding atoms which fall within the virtual box centered at that particular atom. It is known that the largest contribution to potential comes from the nearest neighbours, the potential can be truncated above certain cut-off distance (r_{cut}). The cut-off distance must not be greater than $\frac{1}{2}$L for consistency with minimum image convention [68].
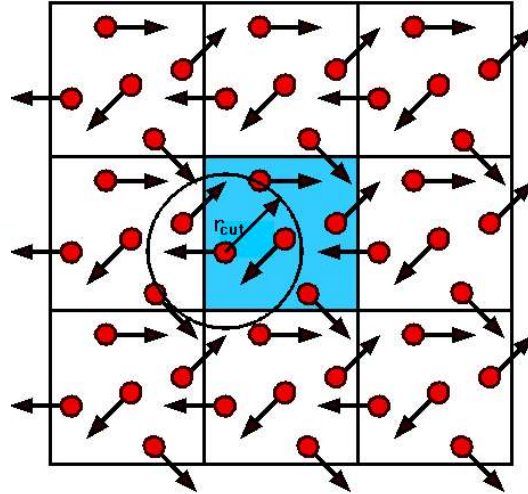
Figure 2.2: A two dimensional periodic system. Shaded region represents the original simulation box and all other boxes are its replicas.

Free boundary conditions: Applying this boundary conditions makes the box non-periodic so that particles do not interact across the boundary and do not move from one side of the box to the other [68]. This boundary conditions are used in order to simulate the effects associated with surfaces. However, using free boundary conditions may result in loss of atoms and this can be avoided by choosing the shrink-wrapped boundary conditions. In shrink-wrapped boundary conditions, even-though the boundary is free, but the position of the face is set so as to encompass the atoms.

Boundary conditions for nanowire, nanopillar and nanofilm: The boundary conditions have to be chosen depending on the system that has to be simulated. Using the periodic boundary conditions may not be the case always. When system of interest contains surfaces, necessarily free boundary conditions have to be chosen. Since the focus of the present thesis is on nanowires and nanopillars, where the role of surfaces becomes important, the shrink-wrapped boundary conditions have been chosen to simulate the nanowire surfaces. Figure 2.3 shows the boundary conditions used in three different directions for nanowires, nanopillars and nanofilms. It has been known that the nanowires are quasi one-dimensional structures with lateral dimensions (d) much smaller than their length (*l*) i.e. length is unconstrained ($l >>> d$). The uncon-

sary to assign initial velocities to the atoms. This velocities have been given according to the Maxwell-Boltzmann distribution which can written as

$$\rho(v_i) = \sqrt{\frac{m_i}{2\pi k_B T}} exp\left(-\frac{m_i v_i^2}{2 k_B T}\right). \tag{2.24}$$

For simplicity, this can be written as a Gaussian function as below

$$\psi(x)_{\mu,\sigma} = \frac{1}{\sqrt{2\pi\sigma^2}} exp\left[-\frac{(x-\mu)}{2\sigma^2}\right], \tag{2.25}$$

with $\mu = 0$, $x = v_i$, and $\sigma = \sqrt{\frac{k_B T}{m_i}}$. A Gaussian random number x generated with zero mean $\mu = 0$ and unit variance ($\sigma = 1$) can be transformed to a random number x' of another normal distribution with μ' and $\mu\sigma'$ by the transformation, $x' = \mu' + \sigma' x$. Since $\mu' = 0$, we can obtain starting velocity distribution by scaling with $\sigma' = \sqrt{\frac{k_B T}{m_i}}$. In simulations, the velocities to each particles were given separately according to $v_i = \sqrt{\frac{k_B T}{m_i}} u_R$, where u_R is random number, usually generated from Gaussian random number generator. This description has been given in detail in ref. [88].

2.3.4 Boundary conditions

Molecular dynamics simulations are usually performed on a system with limited number of atoms. The size of the system is limited by computational speed and storage and also by the execution speed of the algorithm. However, we don't need to simulate a large system all the time. Choosing a small system and replicating it in all three directions may be enough to represent the actual system [68]. This can be achieved by choosing an appropriate periodic or non-periodic (free surface) boundary conditions as described below

Periodic boundary conditions: Applying this boundary condition replicate and translate the system in all three directions to fill the space. As an illustration, Figure 2.2 shows a 2-dimensional system with periodic boundary conditions. The shaded box represents the actual system, while the surrounding boxes are its exact replicas. Whenever an atom leaves the simulation cell, it is replaced by another atom with exactly same velocity, entering from the opposite face. Thus, the atoms in original box and its periodic images behave in exactly the same manner. However, calculating the interaction of a particular atom with remaining atoms in a system with periodic boundary conditions may include its own images. This can be avoided using the

The thermodynamic friction coefficient ζ evolves in time according to a first-order equation as given by

$$\dot{\zeta} = \frac{2}{Q}\left(\sum_i^N \frac{p_i^2}{2m_i} - \frac{gk_BT}{2}\right) \equiv v_T^2\left[\frac{\sum_i^N p_i^2/m_i}{gk_BT} - 1\right] = v_T^2\left[\frac{\tau}{T} - 1\right]. \qquad (2.20)$$

Here v_T is a relaxation rate for thermal fluctuations, τ stands for the instantaneous temperature. The dynamics of the real system depends on the variable ζ and the dynamics of ζ depends on the difference between the present and desired temperature. If $\tau > T$, i.e. the system is hot, accordingly ζ will increase and after reaching a positive value, the system will begin to cool down. If the system is too cold, the reverse happens, and the ζ may become negative, tending to heat up the system again [93]. In terms of velocities the Equation 2.19 can be written as

$$\dot{v}_i = \frac{F_i}{m_i} - \zeta v_i. \qquad (2.21)$$

Therefore, the Nose-Hoover thermostat is implemented by adjusting the velocities of every particle according to ζ. Similarly, the barostat (controlling pressure) can be implemented by adding a dynamic variables coupled to the simulation box dimensions or box volume.

In canonical ensemble (constant NVT), the temperature has a specified average value (T), while the instantaneous total energy of the system can fluctuate. At equilibrium, the root mean square fluctuations σ_E of the Hamiltonian around its average value E are related to the system isochoric heat capacity, c_V through [68]

$$\sigma_E^2 = <H^2>_{NVT} - <H>_{NVT}^2 = k_BT^2 c_V. \qquad (2.22)$$

Similarly, the fluctuations in instantaneous temperature τ in a canonical ensemble are given by [68]

$$\sigma_T^2 = <\tau^2>_{NVT} - <\tau>_{NVT}^2 = 2T^2/g. \qquad (2.23)$$

Here g is number of degrees of freedom in the system. For a system of N particles with N_c constraints, $g = 3N - N_c$. In general, $N >> N_c, \Rightarrow g \approx 3N$. Therefore the Equation 2.23 shows that the fluctuations in the instantaneous temperature are inversely proportional to the number of particles (N) and vanish in the limit of a macroscopic system ($N \to \infty$). Similarly at large T (high temperatures), the fluctuations are non-negligible.

In order to perform constant temperature molecular dynamics simulations, it is neces-

stant pressure (P). Therefore, the equations of motion have to be modified with the purpose of maintaining the constant temperature. Different approaches have been proposed to conduct constant temperature molecular dynamics simulations. All this techniques essentially rely on the equipartition theorem, where the temperature is directly proportional to kinetic energy of the system i.e. the particle velocities. Therefore by adjusting the particle velocities according to the desired kinetic energy, the temperature of the system can be controlled. Similarly, the pressure can be controlled by adjusting the volume of the system.

One simplest method to control the temperature is periodically rescaling the atomic velocities, known as velocity rescaling. However using this method violates the conservation of energy. Therefore, different thermostat algorithms have been proposed to carry out constant temperature molecular dynamics simulations such as Nose-Hoover thermostat [89–91] and Berensden thermostat [92]. In the present thesis, Nose-Hoover thermostat has been used in a canonical ensemble (constant NVT) to carry out constant temperature MD simulations. Generally, the Noose-Hoover thermostat is implemented by introducing an additional degrees of freedom coupled to the particle velocities of the system as described below.

According to Nose [89], the Lagrangian in constant temperature ensemble can be written as

$$L_{Nose} = \frac{1}{2} \sum_i^N m_i s^2 \dot{r}^2 - U(r) + \frac{1}{2} Q \dot{s}^2 - g k_B T \ln s, \qquad (2.17)$$

where m_i is mass of particle i, s is the additional degree of freedom, g is the number of degrees of freedom of a system, Q is a parameter which acts like an effective mass for the degree of freedom s and determines the time scale of the temperature fluctuation, k_B is the Boltzmann constant and T is externally set temperature. Here, the parameter s works like a heat reservoir and acts as a friction coefficient to draw back the current temperature to desired temperature. The kinetic energy term $-\frac{1}{2} Q \dot{s}^2$ is introduced in order to construct a dynamic equation for s.

For this extended system, the Hamiltonian becomes [89]

$$H = \sum_i^N \frac{p_i^2}{2 m_i s^2} + U(r) + \frac{p_s^2}{2Q} + g k_B T \ln s, \qquad (2.18)$$

where p_i and p_s are momenta conjugate to r_i and s, respectively. By introducing the variable $\zeta = p_s/Q$, Hoover [91] eliminated the variable s and p_s from the equations of motion as follows

$$\dot{p}_i = F_i - \zeta p_i. \qquad (2.19)$$

2.3.2 Time step

In the integration schemes of molecular dynamics discussed above, it is necessary to choose an appropriate time step Δt. As the truncation error (e_n) in atomic positions and velocities varies in power-law proportion to the time-step i.e. $e_n \propto (\Delta t)^n$, choosing the large time step leads to divergent unphysical trajectory and also violates conservation of energy and momentum. Similarly, choosing a too small time step makes the calculations inefficient and take very long time. However, there are no reliable methods to calculate the appropriate time step in molecular dynamics simulations. It must be chosen by a balance between the correct trajectory and spanning sufficient phase space. Table 2.2 presents the different values of time-steps used in MD simulations for different systems. In practise, the time step is limited by the fastest process expected to happen during the simulations. Generally, the distance travelled by the atoms in one time step should not be larger than 1/20 of the inter-atomic distance and also it should be smaller than the 1/10 of the period of a bond oscillation [88]. However, the ultimate choice of time step should be based on the conservation of energy. For each new system, new potential, new process and new condition, one must test the suitability of the time step in terms of energy conservation. In the present study, the time steps ranging from 1 - 5 fs have been used in all the simulations.

Table 2.2: Typical values of time-steps used in MD simulations [88].

System (fastest motion)	Time step (1 fs = 10^{-15}s)
Molecules (bond vibrations)	0.5 - 1.0 fs
Molecules, rigit bonds (angle bending)	2.0 fs
Atoms (translations)	1- 10 fs

2.3.3 Ensembles, temperature control and initial velocities

Performing molecular dynamics simulations using the standard equations of motion implements micro-canonical ensemble by default i.e. the simulations will be performed at constant energy (E), with fixed volume (V) and number of particles (N) (constant NVE). In this micro-canonical ensemble, there is no control over temperature (T) and pressure (P). If the system is at equilibrium, then T and P fluctuate about their mean value. In a non-equilibrium simulations, these quantities may undergo a systematic drift. However to mimic the real experimental conditions, the simulations often have to be carried out at constant temperature (T) and/or con-

first order central difference method as

$$v(t) = \frac{r(t + \Delta t) - r(t - \Delta t)}{2\Delta t}. \tag{2.12}$$

It shows that to calculate the velocities at present time t, the positions at later time $t + \Delta t$ needs to be known. Further, the velocity has a 2nd order accuracy compared to the 4th order accuracy of position (Equation 2.10), which introduces some numerical imprecision in particle trajectories [68]. In order to overcome these disadvantages, Verlet algorithm has been modified by incorporating the explicit velocities of high accuracy, known as velocity Verlet algorithm. In the present study, the velocity Verlet algorithm has been used in to integrate the equations of motion. This velocity Verlet algorithm takes the form

$$r(t + \Delta t) = r(t) + v(t)\Delta t + \frac{1}{2}a(t)\Delta t^2 \tag{2.13}$$

$$\text{and} \quad v(t + \Delta t) = v(t) + \frac{1}{2}\Delta t[a(t) + a(t + \Delta t). \tag{2.14}$$

This is generally implemented in three steps

1. First positions at time $t + \Delta t$ are calculated using Equation 2.13.

2. Then, the velocities at the mid-step are calculated using

$$v(t + \frac{\Delta t}{2}) = v(t) + \frac{1}{2}a(t)\Delta t \tag{2.15}$$

3. From the equations of motion, the the acceleration $a(t + \Delta t)$ is calculated and then the new velocities $v(t + \Delta t)$ are obtained as

$$v(t + \Delta t) = v(t + \frac{\Delta t}{2}) + \frac{1}{2}a(t + \Delta t)\Delta t \tag{2.16}$$

Here, the new velocity is obtained based on previous velocity and current force or acceleration. Further, the accuracy of velocity is also improved and it is in the order of $O(\Delta^4)$. Like Verlet, this algorithm is also time reversible and therefore conserves the energy if the system being studied is Hamiltonian.

is an improved version of Verlet algorithm has been used [87]. In the following, the Verlet and velocity Verlet algorithms have been described in detail.

2.3.1 Verlet and velocity Verlet algorithm

The basic idea in Verlet algorithm [87] is that writing a Taylor expansion for position $r(t)$, one forward and one backward in time.

$$r(t+\Delta t) = r(t) + r'(t)\Delta t + \frac{1}{2}r''(t)\Delta t^2 + \frac{1}{6}r'''(t)\Delta t^3 + O(\Delta t^4), \qquad (2.6)$$

$$r(t-\Delta t) = r(t) - r'(t)\Delta t + \frac{1}{2}r''(t)\Delta t^2 - \frac{1}{6}r'''(t)\Delta t^3 + O(\Delta t^4). \qquad (2.7)$$

By defining $r'(t)$ as velocity $v(t)$ and $r''(t)$ as acceleration $a(t)$ and combining the above two equations leads to

$$r(t+\Delta t) + r(t-\Delta t) = 2r(t) + a(t)\Delta t^2 + O(\Delta t^4) \qquad (2.8)$$

$$\implies \quad r(t+\Delta t) = 2r(t) - r(t-\Delta t) + a(t)\Delta t^2 + O(\Delta t^4) \qquad (2.9)$$

Using the Equation 2.5, the above equation can be written as

$$r(t+\Delta t) = 2r(t) - r(t-\Delta t) + \frac{F}{m}\Delta t^2 + O(\Delta t^4). \qquad (2.10)$$

This relation predicts the position of atom at time $t+\Delta t$ using the position at current time t, and previous time $t-\Delta t$ along with acceleration (force) at time t. This algorithm is known as Verlet algorithm [87]. In simple form, the Verlet algorithm can be summarized as [88]

$$\{r(t), a(t), r(t-\Delta t\} \longrightarrow \{r(t+\Delta t), a(t+\Delta t)\}. \qquad (2.11)$$

Verlet algorithm possesses high numerical stability, accuracy and conserves energy and linear momentum. It is also time reversible because of the symmetric usage of $r(t+\Delta t)$ and $r(t-\Delta t)$. However, this algorithm performs calculations without using the velocities, which are necessary to calculate kinetic energy and temperature. The velocities have to be calculated separately by

also used this potential for studying the deformation behaviour of Fe nanopillars. The results obtained in this thesis using Mendelev EAM potentials are in qualitative agreement with either experimental or DFT studies.

2.3 Molecular dynamics

Molecular dynamics is an atomistic simulations technique, where the atoms are assumed to be the building blocks of matter and interacts via a well known inter-atomic potentials [68, 85]. Following this, the time evolution of the system can be obtained by solving the classical Newton's equations of motion for every atom of the system. This is equivalent of saying, advance the system by small time Δt, calculate the forces and velocities, and then repeat this process iteratively. If the time-step (Δt) is small enough, this produces an acceptable approximate solution to continuous motion. Initially, it has been questioned that how a classical equation can describe a system of atoms involving coupled behaviour of electrons and nuclei. However, the foundation of using classical equation of motion in MD simulation lies in the Born-Oppenheimer approximation [86]. It is well known that the nuclei are much heavier than the electrons, and move on a time scale three orders of magnitude longer than that of electrons. The Born-Oppenheimer approximation says that movement of electrons can be reasonably neglected and the movement of atoms involves the motion of nucleus only, which obeys classical Newton's equations of motion. Therefore, the Newton's equations are plausible and can be used to get a phase space trajectory of a system. For a system of N particles interacting through the potential U, the equation of motion for any atom i of mass m_i can be written as

$$m_i \frac{d^2 \vec{r}_i}{dt^2} = \vec{F}_i = -\nabla U(\vec{r}_1, \vec{r}_2......\vec{r}_N), \quad i = 1, 2, ...N \tag{2.5}$$

where r_i is the position of atom i, and F_i is the force acting on this atom due to all other atoms in the system. Once the initial conditions (positions and velocities) and the inter-atomic potential are defined, the equations of motion can be solved numerically to get the phase space trajectory.

For a system of particles/atoms, it is difficult to get a closed form solution [68]. This problem can be overcomed by descretising the equations of motion in time and integrating them by using the finite difference methods. There are many different finite difference methods such as Predictor-Corrector algorithm, Leap-frog algorithm, Verlet and velocity Verlet algorithms. More details can be found in ref. [68]. In the present study, the velocity Verlet algorithm which

range of properties in crystalline and liquid structure.

In clear advancement to the existing potentials, Mendelev et al. [75] developed the potential for BCC Fe based on the Finnis-Sinclair [70] type many body potentials, where the form of the embedding function is chosen as a combination of $\sqrt{\rho}$ and ρ^2. Precisely, $F(\rho_i)$ is chosen as $-\sqrt{\rho} + a^\phi \rho^2$, where a^ϕ is the parameter to be fitted. The detailed functional form of a pair term and other parameter set can be found in ref. [75]. The fitting procedure of Mendelev potential uses a large set of experimental and Ab-initio data in liquid as well as solid phase. In view of this, the Mendelev EAM potential accurately reproduce many defect properties such as self diffusion [76], self interstitial diffusion [77], mobility of edge and screw dislocations [78, 79] and six-fold symmetry of screw dislocation core [80]. Further, this is the only potential which predicts a non-degenerate core structure for screw dislocations [81] and is in good agreement with density functional theory (DFT) calculations [82]. The prediction of screw dislocation core is important in order to correctly reproduce the dislocation behaviour in BCC Fe, where screw dislocations dominates the deformation. In contrast, all other potentials predict a degenerate core structure for screw dislocations.

To simulate the deformation behaviour of nanowires, special attention should be paid towards surface energies and also the generalized stacking fault energy (GSFE). As shown in Table 2.1 the surface energies obtained using the Mendelev EAM potentials are in good agreement with DFT calculations and experimental values [83, 84]. Similarly, Cao [61] has shown that Mendelev potential outperforms all other potentials in predicting the different fault energies such as generalized stacking fault energies and twin fault energies of BCC Fe, in agreement with DFT calculations.

Table 2.1: Surface energies (in J/m^2) of different surfaces in BCC Fe

Method	{100}	{110}	{111}
Mendelev	2.461	2.352	2.653
DFT [83]	2.47	2.37	2.58
Experiments [84]		2.41	

In view of the above superiorities of Mendelev EAM potential for predicting the defect properties, dislocation mobilities, screw dislocation core structure, surface energies and GSFE, this potential has been used in the present study for modelling deformation behaviour of BCC Fe nanowires/nanopillars. In the past, Healy and Ackland [62] and Amlan Dutta [56] have

Finnis-Sinclair chose $F[\rho_i]$ to be $\sqrt{\rho}_i$, which comes from the second moment tight binding approximation.

The second interpretation to Equation 2.3 is given by Daw and Baskes, known as embedded atom method (EAM) [69]. In this interpretation, the attractive second term is the energy change one gets by placing an atom in a uniform electron gas. $F[\rho_i]$ is an embedding functional representing the energy due to embedding an atom in an electron gas of density ρ. The charge density (ρ_i) at site i is calculated from a superposition of atomic charge densities due to atoms within a short range of the atom in question. In this interpretation, the electron density ρ_i is defined as

$$\rho_i = \sum_{j \neq i} \rho(r_{ij}).$$ (2.4)

It may be noted that $j \neq i$ i.e. the electron density at atom i is contributed by neighbouring atoms except the atom i.

However, it must be note that both the FS and EAM interpretations result in a similar functional form for the potential. The only difference being that $F(\rho_i)$ was set as $\sqrt{\rho}_i$ in FS interpretation, while in EAM it was kept as a function to be fitted. Because of this similarity, sometimes both the class of potentials are termed as EAM. Finally, it must be note that these potentials are suited mainly for metals, while different forms are used for strongly covalent materials such as oxides and glasses.

2.2.3 Potential for BCC Fe

Iron (Fe) exhibits distinct polymorphic nature, where it exists in three different solid phases in two different crystal structures, BCC and FCC. The BCC or α phase is stable up to the temperature of about 1184 K, where it transforms to FCC structure (γ phase) and this structure remains stable up to 1665 K. Above this temperature, it again transforms back to BCC structure (δ phase), which is stable up to a melting point of 1809 K. Due to this complex polymorphic nature, developing a potential for Fe is challenging. Generally, the potentials are designed and parametrised by fitting to available experimental data such as lattice parameter, density, cohesive energy, melting temperature, thermal expansion coefficient, elastic constants, vibrational frequencies, etc. In the past, numerous potentials have been developed for modelling the different properties of BCC iron [71–73]. Malebra et al. [74] reviewed the capability of different potentials for BCC Fe. However, none of this potentials are satisfactory in describing it's wide

potential is given by

$$U_{LJ}(r) = 4\varepsilon \left[\left(\frac{\sigma}{r} \right)^{12} - \left(\frac{\sigma}{r} \right)^{6} \right], \tag{2.2}$$

where σ and ε are material parameters. The term $+1/r^{12}$ is the repulsion term acting at very small distances. The negative term $-1/r^6$ dominates at large distance and constitute the attractive part of the system. This part also describes the van der Waals forces, which are responsible for bonding in closed-shell systems, such as inert gases. In view of this, L-J potential describes the inert gases most effectively. However, this potential fails to describe the interaction between the atoms when the covalent or metallic bonding is present [68].

The advantage of pair potentials is that, they are computationally efficient for large scale simulations because of the simple description of potential energy. In view of this, L-J potential is often used in simulations where the objective is to model the general effects rather than the specific ones. However, the disadvantage of L-J potential is low accuracy, fails to describe the anisotropy of elastic constants, overestimates the melting point, and it cannot distinguish between vacancy formation energy and binding energy. These limitations can be overcomed using semi-empirical potentials.

2.2.2   Semi-empirical potentials

The functional form of a semi-empirical potential consist of many body term in addition to the pair term. The many body term takes care of all higher order interactions other than the pairwise interactions. The framework of this potential is partly based on quantum mechanics, while some parameters are determined empirically. In this framework, the total potential energy can be written as

$$U_{tot} = \frac{1}{2} \sum_{ij} V(r_{ij}) + \sum_{i} F[\rho_i]. \tag{2.3}$$

Here, $V(r_{ij})$ is purely repulsive pair potential and $F[\rho_i]$ is many body term. In many body term, the material dependency has been introduced through the electron density ρ. The functional form of $F[\rho_i]$ is deduced primarily by semi-empirical methods and partly through fitting. There are mainly two different interpretations for above potential, the embedded atom method (EAM) interpretation by Daw and Baskes [69] and Finnis-Sinclair (FS) [70] interpretation.

The FS interpretation [70] is based on the tight binding model. In this interpretation, the second term in Equation 2.3 is a band energy that results in bonding and the repulsive pair term is the interaction between atomic cores consisting of nuclei and valence electrons.

The real potentials are the combination of many terms and hence, it is difficult to obtain their precise functional form. However, for simple cases, the pair potentials serve as a reasonable approximation for the inter-atomic interactions. Further, the pair potentials can be parametrised or an extra empirical terms can be added to reproduce the many body interactions. The goal of the potential development is to obtain the approximate functional form and the material specific set of parameters. Depending on the complexity of a material, the potential function may contain several parameters. In the following, the basic potential functions such as pair potentials followed by complex many-body potentials, which is of more importance for the representation of metals have been described briefly.

The potential function of a particular system can be obtained in three different ways. In first a functional form is assumed and then the parameters are obtained to reproduce the experimental data. The potentials obtained in this method are known as **empirical** potential. The potentials functions such as Lennard-Jones, Morse, and Born-Mayer potentials falls in this category. Second method is to calculate the electronic wave function for fixed atomic positions and using different quantum-mechanical arguments, an analytic form for the potential is derived. These potentials are known as **semi-empirical** potentials. The potentials such as Embedded Atom Method (EAM), Modified EAM, Finnis-Sinclair (FS), Stillinger-Weber (SW), bond order potentials (BoP) falls under this category. Third way is by performing the quantum mechanics based electronic structure calculations of forces, a method known as **Ab-initio or first principle** calculations. However, the first principle calculations are computationally expensive and hence their utility is limited to a system with few hundred atoms or less. As a result, most large-scale and long-time simulations are performed using empirical or semi-empirical potentials. In the following, the empirical and semi-empirical potentials are briefly described.

2.2.1 Empirical potentials

In empirical potentials, the inter-atomic interactions are represented by a simple function of distance between the atoms (r), and the parameters in the function are determined empirically to reproduce the experimental results of interest, for example, lattice constant, elastic constants etc. There are many well known empirical potentials such as hard sphere, soft sphere, square well, Buckingham, Morse and Lennard-Jones potentials. The functional form of different potentials are described in Ref. [68]. As an example, the functional form of Lennard-Jones (L-J)

repulsive terms [67, 68]. It can be seen that the potential has a well defined "well" around its minimum. The inter-atomic distance corresponding to the minimum of this well, E_0 is equilibrium separation r_0. The magnitude of E_0 and r_0 vary from material to material and dictates many important properties of materials. For example, the materials having large E_0 have high melting point. Similarly, the elastic modulus depends strongly on the the shape of the curve, particularly around r_0 [67].
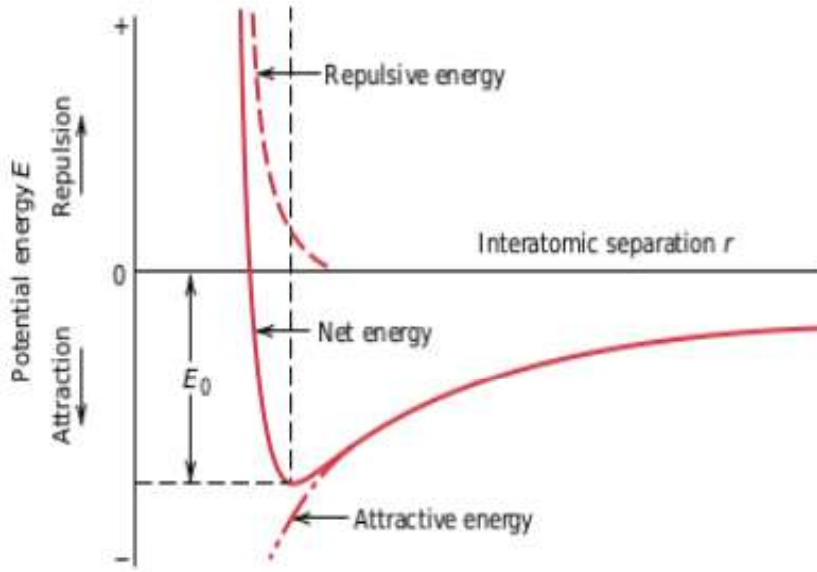
Figure 2.1: The typical shape of an inter-atomic potential as a function of inter-atomic separation [67].

The general functional form of any inter-atomic potential for a system of N particles can be written as [68]

$$U(r) = \sum_i U_1(r_i) + \sum_{i,j} U_2(r_{i,j}) + \sum_{i,j,k} U_3(r_{i,j,k}) + \dots \dots \quad (2.1)$$

The term U_1 is a one-body term and it is due to an external field. The second term U_2 is a typical two-body term known as pair potential, where the interaction of any pair of atoms depends only on their spacing and is not affected by the presence of other atoms. The third term U_3 is a three-body term and it arises when the interaction of a pair of atoms is modified by the presence of a third atom. In practice, the external field term, U_1 is usually ignored. Based on the type of interactions, the potentials have been separated into two main classes: (1) **pair potentials**, where only U_2 is present, and (2) **many-body potentials** which includes U_3 and all other higher order terms in addition to the pair term.

Chapter 2

Molecular dynamics simulations : Methodology and post-processing

2.1 Introduction

In the present work, the classical molecular dynamics simulations have been used to investigate the mechanical properties and deformation behaviour of BCC Fe nanowires. It has been known that the inter-atomic potentials plays an important role on the reliability of MD simulation results. This chapter provides a brief overview of different inter-atomic potentials and the basics of molecular dynamics simulations. The method of implementing tensile/compressive loading in MD simulations, pre-processing methods to create the required configurations of nanowire/nanopillars and the post-processing techniques used for the visualization of various defects have been described in detail. Following this, a short description about the LAMMPS package used for MD simulations has been given. Visualization packages such as AtomEye and OVITO have been described.

2.2 Inter-atomic potentials

In solid, the inter-atomic forces binds the atoms together and it is responsible for the structural stability. Many properties of a material can be predicted based on the knowledge of inter-atomic forces. At large inter-atomic distances, the interactions are negligible and at the same time, the atoms cannot come too close to each other. Therefore, the inter-atomic potential contains an attractive term, so that the atoms bond together, and repulsive term giving rise to a state of equilibrium separation. Figure 2.1 shows the form of a typical inter-atomic potential as a function of inter-atomic separation between two atoms clearly showing the attractive and

31

3.8 Conclusions

Molecular dynamics simulations performed on BCC Fe nanowires indicated that the deformation behaviour strongly depends on orientation and loading mode. Under tensile loading, the <100>, <112> and <102> nanowires deformed by twinning on <111>/{112} twin system, while the deformation in nanowires with <110> and <111> orientations was dominated by the slip of 1/2<111> full dislocations. Under compressive loading, the <100> oriented nanowire deformed by full dislocation slip, while twinning was observed in <110> nanowire. The deformation by twinning in BCC Fe nanowires has led to reorientation within the twinned region. Based on the observed results on deformation twinning, a simple twin nucleation and growth model applicable to BCC Fe nanowires was presented. A good agreement between the operative deformation mechanisms with respect to nanowire orientation and those reported for the bulk single crystal counterparts based on experimental results was observed. Both <100> and <110> oriented nanowires displayed opposite tension-compression asymmetry. The orientation dependent deformation behaviour and the opposite tension-compression asymmetry in deformation mechanisms in BCC Fe nanowires has been explained in terms of twinning-antitwinning asymmetry of 1/6<111> partial dislocations on {112} planes.

3.16, which is equivalent to the motion of a single 1/6<111> partial dislocation in Figure 3.14. Initially, the 1/12<111> partials lie on adjacent planes {112} planes marked 1 and 3 in Figure 3.16a. With continuous glide, annihilation and nucleation of these partials on adjacent planes, the twin grows along the nanowire axis by a layer by layer by growth process. Each nucleation, glide and annihilation of twinning partial dislocation removes one inter-planer spacing from the parent lattice and adds to the twinned lattice (Figure 3.16a-d).
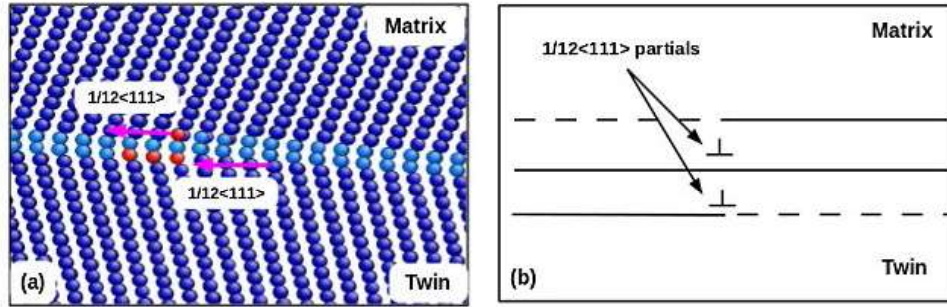
Figure 3.15: The structure of twin boundary in BCC Fe nanowire using Mendelev EAM potential.
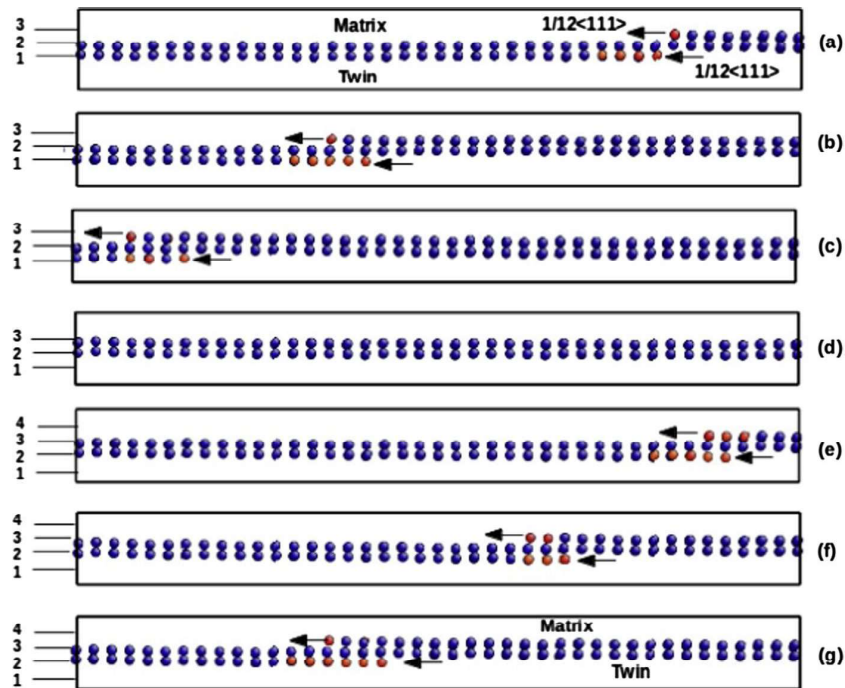
Figure 3.16: The atomistic process of twin growth in BCC Fe nanowires. The twin growth proceeds by repeated initiation and glide of 1/6<111> (= 1/12<111> + 1/12<111>) partial dislocations on adjacent {112} planes. The blue atoms represents the {112} twin boundary and arrow marks on twin boundary show the 1/12<111> partial dislocations. The twin boundary layers are marked with 1, 2, 3 and 4..

3.7.4 Twin nucleation and growth and twin boundary structure

Several twin nucleation and growth model have been proposed in single crystal bulk BCC metals [116]. Based on the results obtained in the present study (Figures 3.6, 3.7, and 3.11), a simple model of twin nucleation and growth in BCC Fe nanowires has been presented in Figure 3.14. It can be seen that the 1/6<111> partial dislocation nucleates from the corner of the nanowire (i.e. the stress concentration site) with a stacking fault behind in Figure 3.14a. In defect free nanowire, the stress required for the nucleation of 1/6<111> partial dislocation is in the order of theoretical stress. The nucleation of twin embryo corresponds to the onset of yielding in the nanowire and this leads to an abrupt drop in flow stress. With increasing deformation, the initially nucleated 1/6<111> partial dislocation glides further in <111> direction (Figure 3.14b) and an additional 1/6<111> partial dislocations nucleates from the intersection of the surface and stacking fault as shown in Figure 3.14b and c. Eventually, the twin front reaches the opposite surface and becomes twin lamella enclosed by {112} twin boundaries (Figure 3.14d). Following this, the twin lamella grows along the nanowire axis by the successive nucleation and glide of 1/6<111> partial dislocations on adjacent {112} planes.
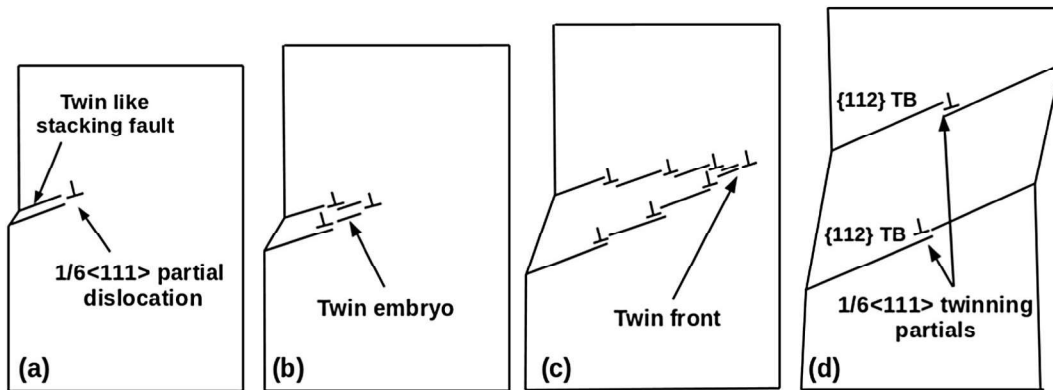
Figure 3.14: The schematic diagram showing the nucleation and growth of a twin in BCC Fe nanowire.

The structure of the twin boundary in BCC Fe nanowires observed in the present investigation using Mendelev EAM potential is typically shown in Figure 3.15a. It can be seen that the twin boundary does not have a mirror image structure and is similar to a displaced boundary (Section 1.2.5) as observed by Bristowe and Crocker [19] and Yamaguchi and Vitek [20]. Unlike a sharp twin boundary which consists of 1/6<111> partial dislocation, the displaced twin boundary comprises of two 1/12<111> partial dislocations lying in the adjacent {112} planes [20], as shown schematically in Figure 3.15b. In the case of a displaced boundary, the twin grows by the collective motion of two 1/12<111> partial dislocations as shown in Figure
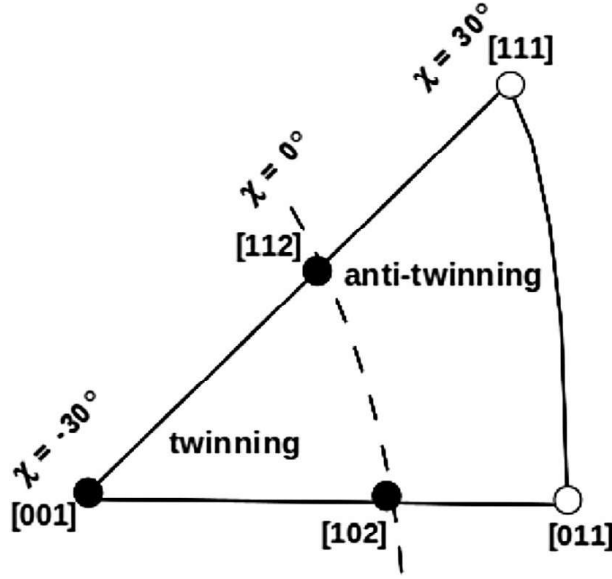
Figure 3.13: The standard stereographic triangle showing the regions of twinning and antitwinning sense of 1/6<111> partials during tensile deformation. Under compression, this twinning-antitwinning sense is reversed. Here χ is defined as the angle of maximum resolved shear stress plane (MRSSP) with respect to $(\bar{1}01)$ plane in BCC Fe.

3.7.3 Tension-compression asymmetry

The stress-strain behaviour of BCC Fe nanowires under tensile and compressive loading (Figure 3.4) indicated that the <100> and <110> orientations display opposite tension-compression asymmetry in yield stress. Under tensile loading, the <110> orientation showed higher yield strength than in compression, while the <100> orientation exhibited higher yield strength in compressive loading than in tension. The opposite tension-compression asymmetry observed in BCC Fe nanowires is in agreement with the reported experimental observations on BCC Mo nanowires [113]. The observed opposite tension-compression asymmetry in <100> and <110> nanowires results mainly from the different yielding mechanisms under tensile and compressive loadings. The yielding in <100> nanowire under tensile loading occurred by the nucleation of a twin embryo, while the nucleation of full dislocation loop has been observed under compressive loading. This is consistent with the yielding behaviour reported by Healy and Ackland [62]. In <110> orientation, the yielding under tensile loading occurred due to the nucleation of full dislocation loops, while the nucleation of a twin embryo has been observed under compressive loading. The opposite tension-compression asymmetry in <100> and <110> BCC Fe nanowires can be ascribed as a consequence of opposite twinning-antitwinning sense of 1/6<111> partial dislocations.

the orientation and loading mode dependent deformation behaviour of BCC Fe nanowires based on the twinning-antitwinning asymmetry of 1/6<111> partial dislocations on {112} planes (Section 1.2.4). In BCC systems, the full dislocations can be regarded as leading 1/6<111> partial and trailing 1/3<111> partial dislocations, and the twinning can be considered as repeated initiation and glide of 1/6<111> partial dislocations on adjacent {112} planes [60]. Once the 1/6<111> partial dislocation nucleates from the corners of the nanowires, the mode of deformation is determined by the nucleation of subsequent partial dislocation. If the subsequent partial dislocation is of 1/6<111> type, the deformation occurs by twinning [60]. In case, the next partial dislocation is of 1/3<111> type, the deformation occurs by full dislocation slip [60]. It can be seen that in both slip and twinning cases, the first partial that nucleates is 1/6<111>. However, the glide of these 1/6<111> partial dislocations is allowed only in one direction (twinning sense) and the glide in opposite direction (antitwinning direction) creates an unstable stacking fault which is not a twin plane (Section 1.2.4). By defining χ to be an angle between maximum resolved shear stress plane (MRSSP) and $(\bar{1}01)$ plane, a boundary separating the twinning-antitwinning sense of 1/6<111> partial dislocation can be drawn at $\chi = 0$ [113–115] as shown in Figure 3.13. The orientations with positive and negative χ values are not equivalent. Under tensile loading, the 1/6<111> partial dislocation glides in twinning sense on {112} planes for the orientations where $\chi < 0$ [114]. Because of this twinning sense, it would be easier for the initial and subsequent nucleation of 1/6<111> partial dislocations (1/6<111> partials have lower critical resolved shear stress in twinning sense), which facilitates deformation by twinning rather than the full dislocation slip in <100>, <102> and <112> orientations. On the other hand, the 1/6<111> partial dislocation glides in antitwinning sense for the orientations where $\chi > 0$ [114]. Due to this antitwinning sense for $\chi > 0$, it would be difficult for the nucleation of 1/6<111> partial dislocations (1/6<111> partials have high critical resolved shear stress in anti-twinning sense) and this hinders the occurrence of twinning in <110> and <111> orientations leading to deformation by full dislocation slip.

Under compressive loading, the twinning-antitwinning sense of 1/6<111> partial dislocations is reversed (Figure 3.13), i.e., for $\chi < 0$ orientations, the 1/6<111> partial dislocations move in antitwinning sense, and this leads to deformation by slip under the compressive loading of <100> nanowire. Similarly for $\chi > 0$ orientations, the 1/6<111> partial dislocations move in twinning sense leading to deformation by twinning under the compressive loading of <110> nanowire.

tion twinning for <100>-tension, <110> and <111>-compression, while dislocation slip is observed for <112>-tension and compression. In agreement with this experimental study, the present results shows deformation twinning for <100>-tension and <110>-compression. The orientation dependence of twinning in BCC Fe nanowires observed in the present study along with that reported in bulk single crystals by Harding is shown in Figure 3.12. In bulk single crystals, a boundary at an angle of 37°from <100> orientation separating the orientations favourable for twinning and those not favourable is shown as dashed contour. It can be seen that the nanowire orientations exhibiting twinning fall within the contour defined by Harding. However, the main difference between the two studies is that the twinning is observed along with slip in bulk single crystals [106], whereas in BCC Fe nanowires, the deformation is solely dominated by twinning without major slip events.
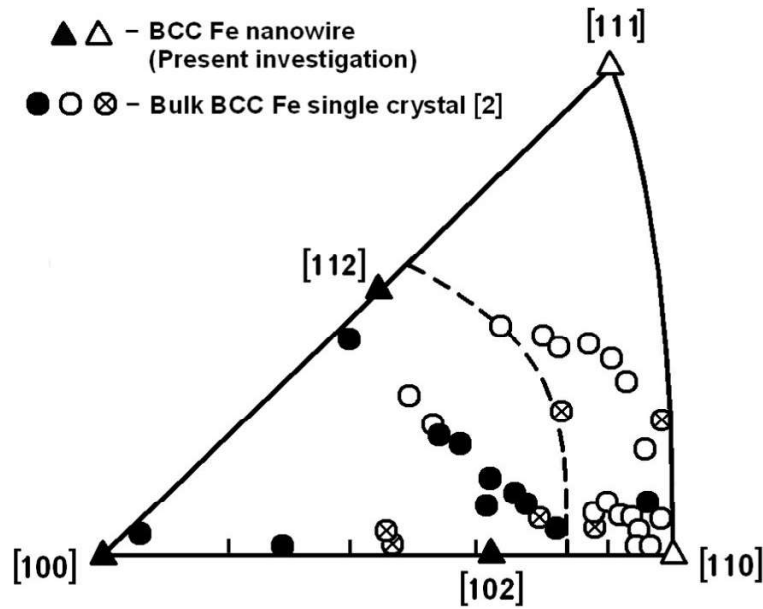
Figure 3.12: The standard stereographic triangle showing the orientation dependence of twinning in BCC Fe nanowires. The symbols ▲ and △ denote the presence and absence of twinning, respectively, in BCC Fe nanowires. The twinning behaviour with respect to orientation (● - extensive twinning, ○ - no twinning and ⊗ - with few twins) reported for bulk BCC Fe single crystals at room temperature and at dynamic strain rates is superimposed [106].

The orientation dependent deformation behaviour in FCC nanowires has been explained by the Schmid factor analysis (Section 1.3.1). In BCC nanowires, presence of non-Schmid stresses makes the slip to violate the Schmid law and therefore, the Schmid law cannot be used. The deformation by slip or twinning in FCC/BCC nanowires can also be understood by calculating the generalised planer fault energies [60, 61]. However, this method cannot explain loading mode dependence of deformation behaviour. Here, we provide a clear explanation for

3.7 Discussion

3.7.1 Non-linear elastic deformation

In atomistic simulation studies, the elastic deformation of many metallic nanowires have been observed to be non-linear under different loading conditions [22, 23]. The non-linear elastic deformation observed at large strains in the present investigations can be attributed to the nature of inter-atomic forces in BCC Fe nanowires. For small displacements about equilibrium, the inter-atomic forces vary linearly with inter-atomic distance and this leads to linear relation between stress and strain at small strains [16, 67]. However, at higher inter-atomic distances, the inter-atomic force varies non-linearly and this leads to the non-linear elastic deformation at large strains. Due to negligible defect density and high surface effects, the defect nucleation in the pristine nanowires requires high stress, and as a result, the nanowires display enhanced elastic deformation (i.e., higher elastic strains) compared to their bulk counterparts. As a result, the non-linear elastic deformation is observed mainly in materials at nanoscale. The observed non-linearity in elastic deformation of BCC Fe nanowires (Figure 3.3) results as a consequence of the ability of the nanowires to undergo large elastic deformation.

3.7.2 Effect of orientation on deformation mechanisms

The yield strength dependence on orientation is associated with the defect nucleation in a pristine nanowire. It has been observed that the <100>, <102> and <112> BCC Fe nanowires yield by the nucleation of a twin embryo and exhibit lower yield strength than the yield strength values of <110> and <111> nanowires deformed by dislocation slip mode. The high yield strength in <110> and <111> nanowires results from the higher stress required for nucleation of high energy full dislocations responsible for slip mechanism [112]. Contrary to this, lower stress is needed for the initiation of relatively low energy partial dislocations responsible for twinning [112] and this result in the low yield strengths in <100>, <102> and <112> orientations. The occurrence of twinning in <100>, <102> and <112> oriented nanowires and its absence in <110> and <111> orientations is similar to their bulk single crystal counterparts [106].

The deformation mechanisms observed in the present investigation on Fe nanowires are quite close to the experimental observations in BCC W nanopillars [63]. Using in-situ transmission electron microscopy in BCC W nanopillars, Wang et al. [63] predicted deforma-

72
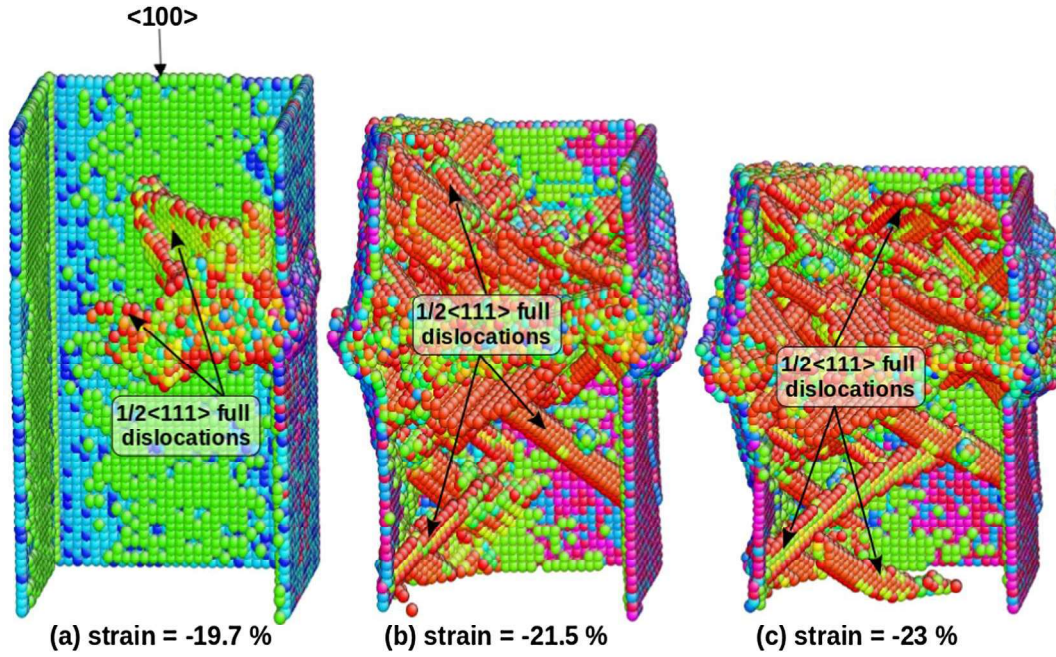
Figure 3.10: The atomic snapshots showing deformation behaviour of $<100>$ oriented BCC Fe nanowire under compressive loading. Nucleation of full dislocations in (a) and dislocation interactions along with bulging at the surfaces in (b-c) can be seen. The atoms are coloured according to the centro-symmetry parameter (CSP). The perfect BCC atoms and front surfaces are removed for clarity.
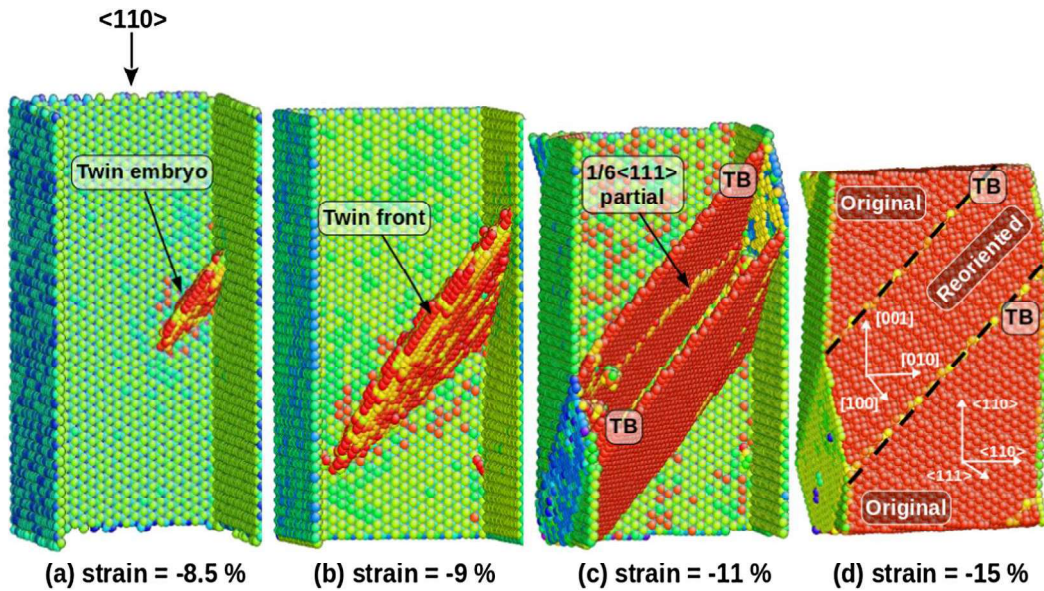
Figure 3.11: The atomic snapshots showing (a) nucleation and (b) growth of twin embryo, (c) formation of a full twin plate and (d) reorientation within the twinned region during the compressive deformation of $<110>$ nanowire. The atoms are coloured according to the centro-symmetry parameter (CSP). The perfect BCC atoms and front surfaces are removed in (a-c) for clarity. Only front surface is removed in (d).

71

3.6 Deformation behaviour under compression

In order to examine the influence of loading mode, additional MD simulations were performed under compressive loading on <100> and <110> oriented BCC Fe nanowires. The deformation behaviour under compression in both <100> and <110> nanowires is presented below:

3.6.1 Deformation by slip

Figure 3.10 shows the atomic configurations during compressive deformation of <100> BCC Fe nanowire. The plastic deformation initiated by the nucleation of 1/2<111> full dislocations from the corner of the nanowire can be seen in Figure 3.10a. The <100> nanowire under compression yielded at a significantly higher strain of 19.7% than under tension (Figure 3.4). With increasing strain, the deformation spread uniformly across the nanowire by the dislocation motion, and large number of dislocations arising from continuous dislocation nucleation and interactions can be seen in Figures 3.10b and c. Significant bulging on the side surfaces can also be seen in Figures 3.10b and c. Like tensile deformation in <100> nanowire, twinning was not observed during compressive loading and the deformation was dominated by dislocation slip mechanism.

3.6.2 Deformation by twinning

In Section 3.5.2, it has been shown that the <110> oriented BCC Fe nanowire deform by dislocation slip mechanisms under tensile loading (Figure 3.8). The atomic configurations at various stages of deformation during the compressive loading of <110> nanowire are shown in Figure 3.11. The yielding under compressive loading occurred by the nucleation of a twin embryo from the corner of the nanowire (Figure 3.11a) causing an abrupt drop in flow stress. The propagation of initially nucleated twin embryo towards the opposite surface can be seen in Figure 3.11b. The twin embryo consisted of 1/6<111> partial dislocations along with 'twin' like stacking faults on {112} planes (Figure 3.11a and b). With increasing deformation, the propagation of the leading edge of the twin embryo, i.e. the twin front to the opposite surface results in the full twin enclosed by twin boundaries on {112} planes as shown in Figure 3.11c. With further increase in deformation, the twin grows by the motion of twin boundary along the nanowire axis (Figure 3.11c and d). The transformation of <110> nanowire into <100> nanowire with {100} lateral surfaces due to twinning induced reorientation in the twinned region can be seen in Figure 3.11d.
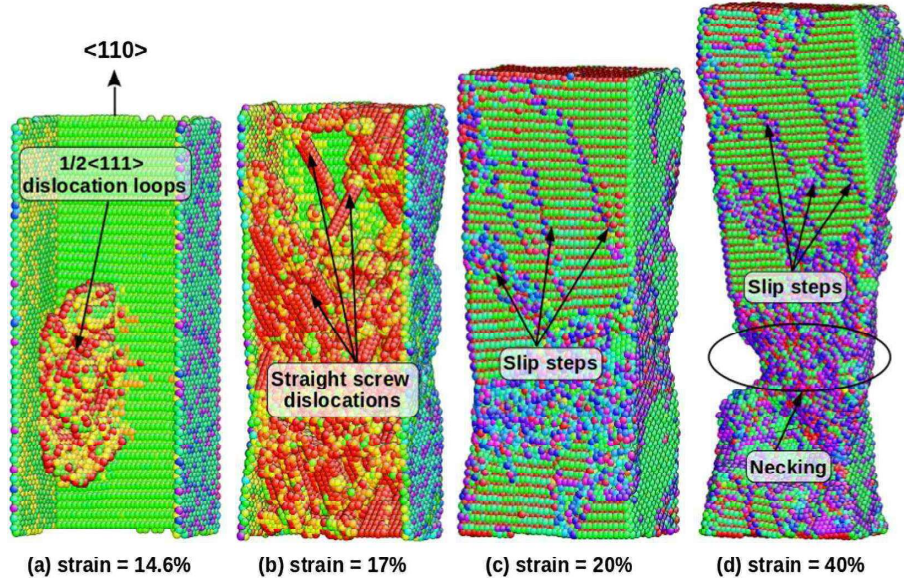
Figure 3.8: The atomic snapshots showing (a) nucleation of dislocation loops, (b) accumulation of straight screw dislocations, (c) slip steps formed due to dislocation escape and (d) neck formation during the tensile deformation of <110> nanowire. The atoms are coloured according to the centro-symmetry parameter (CSP). Perfect BCC atoms and front surfaces are removed for clarity in (a) and (b).
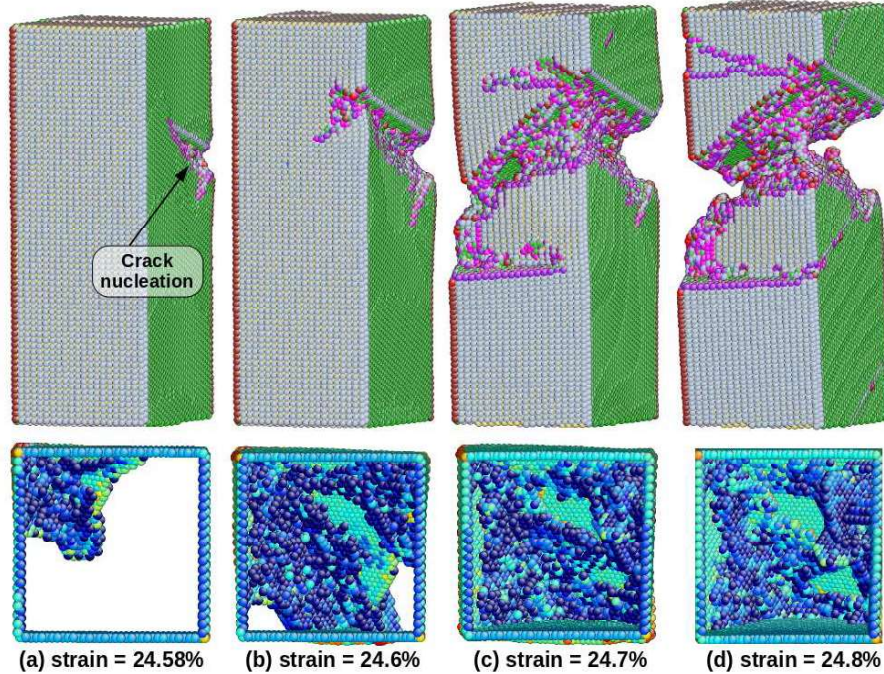
Figure 3.9: The atomic snapshots showing (a) nucleation of crack, (b-d) rapid growth of crack leading to sudden failure during tensile deformation of <111> BCC Fe nanowire. Bottom row figures shows the axial view of the nanowire. The atoms are coloured according to the coordination number in top row and centro-symmetry parameter in bottom.

69

the reoriented <100> nanowire again transform to <110> orientation as observed in Figure 3.6. With increasing deformation, it has been observed that these reoriented <100> nanowire deforms by twinning, however, further reorientation of this nanowire is not observed due to minor dislocation activity, which disrupts the reorientation process [59].

3.5.2 Deformation by dislocation slip

The BCC Fe nanowires with <110> and <111> orientations deforms by dislocations slip under tensile loading. The deformation behaviour of <110> oriented nanowire at different strain values is presented in Figure 3.8. In <110> nanowire, the yielding occurred at a strain level of 14.4% by the nucleation of multiple 1/2<111> dislocation loops from the corner of the nanowire (Figure 3.8a). The yielding resulted in large stress drop from 22.72 GPa to 2.2 GPa. In absence of obstacles in the nanowire, dislocations loops once nucleated easily expand in multiple directions. With increasing strain, the accumulation of large number of straight screw dislocations can be seen in Figure 3.8b. It is known that the edge dislocations have higher mobility than the screw dislocations in BCC metals [111]. As a result, the edge components easily escape to surface, and this leads to pile-up of screw dislocations in the nanowire. The annihilation of edge components at the surface also leaves slip steps as seen clearly in Figure 3.8c. With increasing strain, the activation of multiple slip leads to the formation of a neck in the nanowire (Figure 3.8d). Similarly, the deformation in <111> BCC Fe nanowire is also dominated by dislocation slip. However, the deformation is slightly different than <110> nanowire.

Figure 3.9 shows the deformation behaviour during the tensile loading of <111> nanowire. The nanowire yielded at a strain level of 24.58% by the nucleation of a crack from the corner (Figure 3.9a). With increasing strain, the crack grows rapidly along the direction at 45°angle with the loading axis (Figures 3.9b and c). During crack growth, a few 1/2<111> in the vicinity of crack tip can be seen in the bottom figures (Figures 3.9b and c). The growing crack reaches the opposite surface within a short strain interval and the nanowire fails abruptly without showing significant plastic deformation (Figure 3.9d). These observations clearly suggest that the <111> nanowire undergo deformation by crack nucleation and growth with few dislocations at the crack tip. Since few dislocations have been observed without any twinning, the deformation behaviour in this nanowire is considered as deformation by slip.
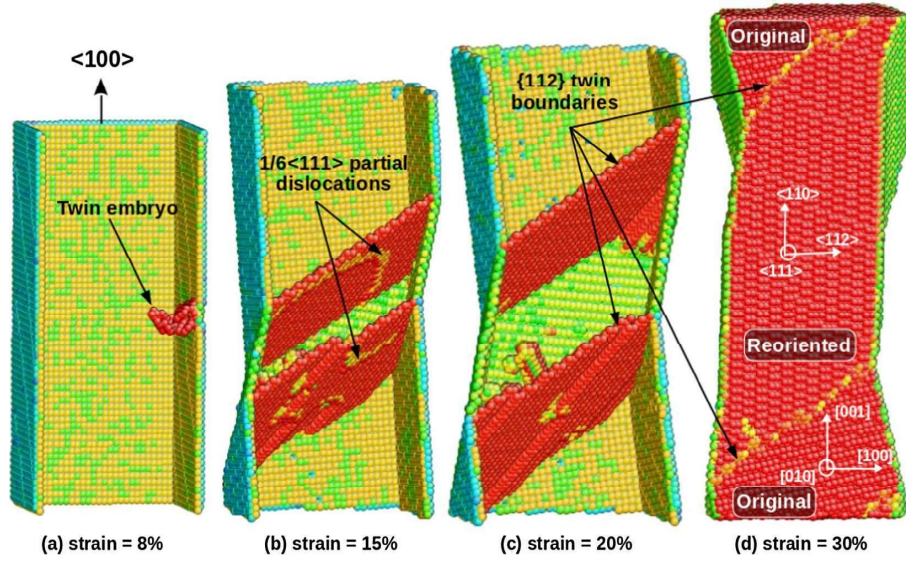
Figure 3.6: The atomic snapshots showing (a) nucleation of a twin embryo, (b) full twin enclosed by two twin boundaries, (b-c) twin boundary motion and (d) the reorientation within the twinned region during the tensile deformation of <100> nanowire. The atoms are coloured according to the centro-symmetry parameter (CSP). The perfect BCC atoms and the front surfaces are removed for clarity in (a-c), while only front surface was removed in (d).
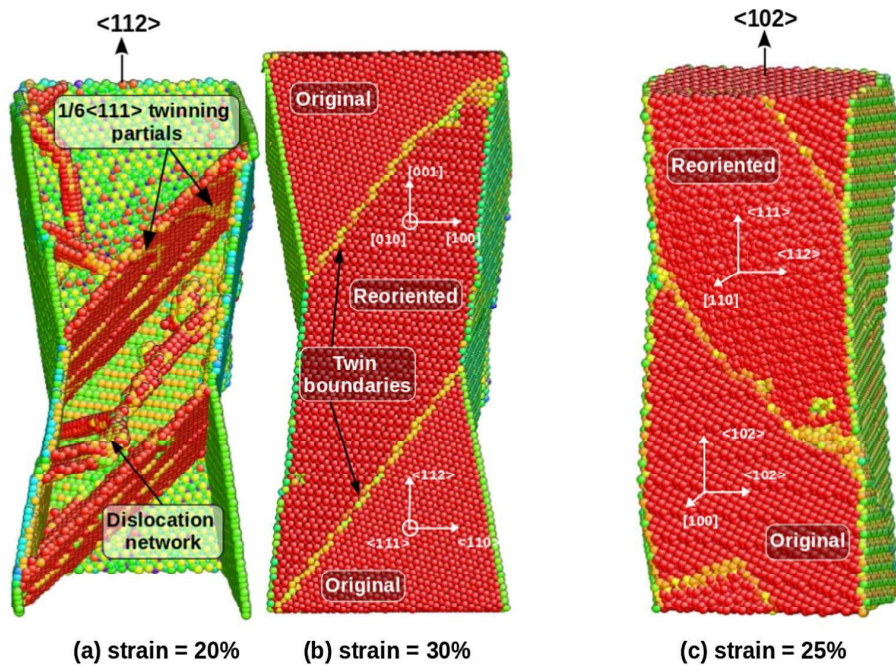
Figure 3.7: The atomic snapshots showing (a) full twin with small dislocation activity and (b) reorientation within the twinned region in <112> orientation and, (c) reorientation within the twinned region in <102> orientation during tensile deformation of BCC Fe nanowires. The atoms are coloured according to the centro-symmetry parameter (CSP). The perfect BCC atoms and the front surfaces are removed in (a) for clarity. Only front surfaces are removed in (b) and (c).

3.5   Deformation behaviour under tensile loading

The evolution of atomic configurations at various stages of tensile deformation were analysed for all the orientations using centro-symmetry parameter (CSP) [101]. Based on this analysis, the deformation mechanisms under the tensile loading of BCC Fe nanowires with various orientations were classified into twinning and dislocation slip as described in the following:

3.5.1   Deformation by twinning

The BCC Fe nanowires with <100>, <112>, and <102> orientations deforms mainly by twinning mechanisms under tensile loading. The atomic snapshots at various strain levels during tensile deformation of <100> oriented nanowire are shown in Figure 3.6. The yielding in <100> nanowire by the nucleation of a twin embryo on {112} planes can be seen in Figure 3.6a. Similar yielding mechanism was observed in <112> and <102> orientations. The yielding in the nanowires resulted in a sharp drop in flow stress from a peak value to a low stress value (Figure 3.3). With increasing strain, the twin embryo grows into full twin enclosed by two {112} twin boundaries consisting of 1/6<111> twinning partial dislocations as depicted in Figure 3.6b. The repeated nucleation and glide of 1/6<111> twinning partial dislocations leads to twin growth along the nanowire axis (Figure 3.6b and c). The observed constant and low flow stress during plastic deformation of <100>, <112> and <102> nanowires result mainly from the twin boundary motion along the nanowire axis. Based on the surface structure analysis, it has been observed that the twinning in <100> oriented nanowire with {100} surfaces leads to reorientation to <110> nanowire with {111} and {112} lateral surfaces in the twinned region (Figure 3.6d).

The atomic configurations during the tensile deformation of <112> and <102> nanowire is presented in Figure 3.7. Like <100> orientation, the <112> and <102> nanowires also deforms by twinning mechanism. However, in <112> oriented nanowire, the minor dislocation activity in both the twinned region and the original lattice has been observed (Figure 3.7a). With further increase in deformation, these dislocations move to the surface and the twin grows along the nanowire axis. Due to deformation twinning, the original <112> nanowire with {111} and {110} surfaces transforms to <100> nanowire with {100} lateral surfaces (Figure 3.7b). Similarly, the <102> nanowire with {100} and {102} lateral surfaces also transforms to <111> nanowire with {110} and {112} side surfaces (Figure 3.7c). Since the <112> nanowire is reoriented to <100> orientation, it would be interesting to see whether

66
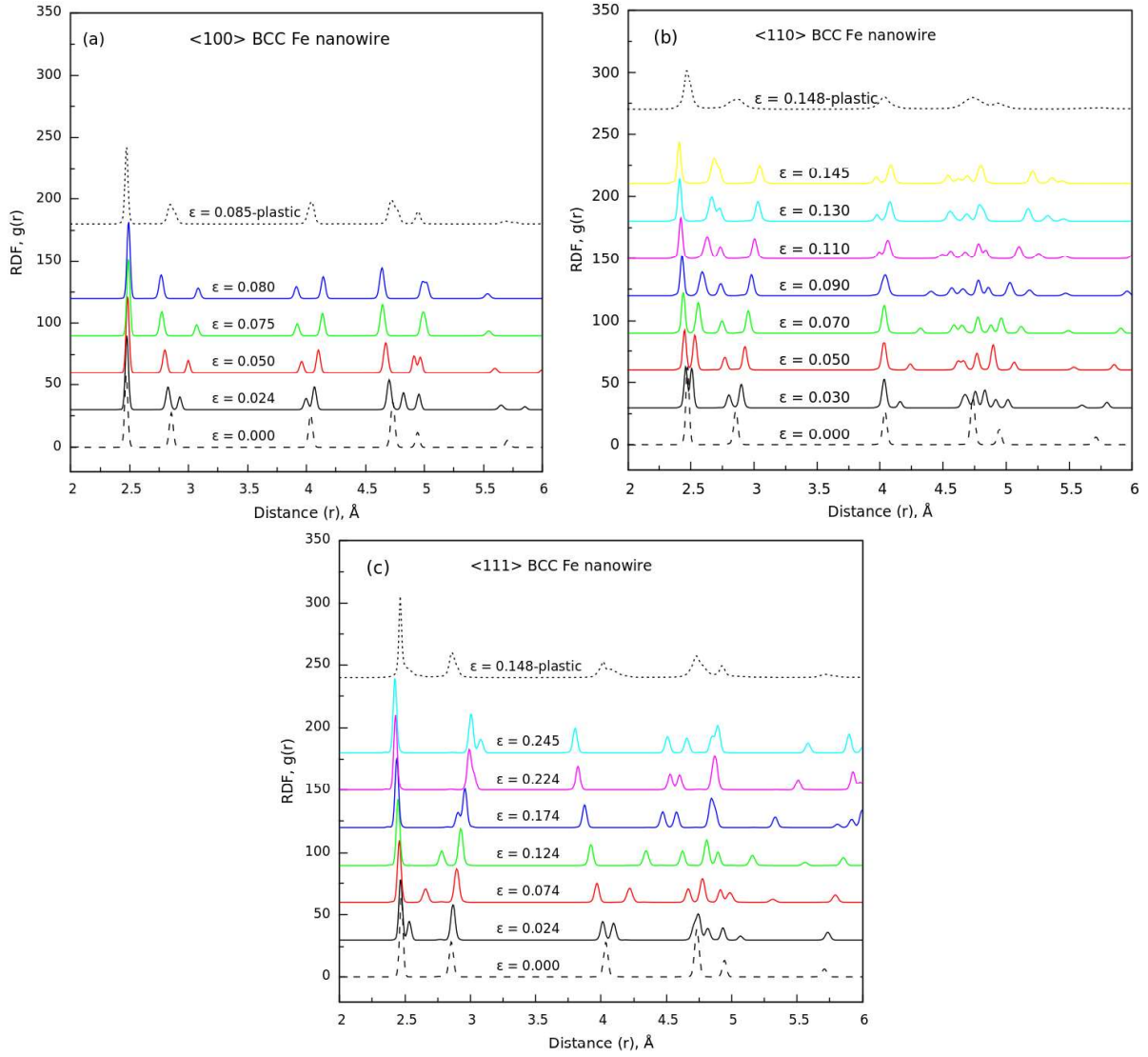
Figure 3.5: The radial distribution function (RDF) at various strains during the elastic deformation of (a) <100>, (b) <110>, and (c) <111> oriented BCC Fe nanowires under tensile loading at 10 K.

Based on the relative shift of secondary peak positions in RDF, the atomic level tensile or compressive strain (e) in various coordination shells has been calculated as $e = (d_\varepsilon - d_0)/d_0$, where d_ε is position of the peak in RDF at strain ε, and d_0 is the original position of the peak at zero strain. The microscopic or atomic level tensile and compressive strains have been evaluated in the first four nearest neighbour shells for <100>, <110>, and <111> orientations. In <100> orientation, the microscopic tensile strain in second shell has been found to be equal to the overall macroscopic strain, while in <110> and <111> orientations, the microscopic tensile strains in third and first shells, respectively represented the overall macroscopic strain.

of <100> nanowire, the second, third and fourth peaks in RDF splits into two independent secondary peaks at low elastic strain of 0.024 (Figure 3.5a). With increasing strain, one of the secondary peaks shifts towards higher distances, while other move towards lower distance with respect to original RDF peaks. At the atomic level, this splitting of peaks indicates that during elastic deformation of <100> BCC Fe nanowire, the second, third and fourth nearest neighbour shells gets divided into two independent secondary shells. With increasing strain, one secondary shell radius increases, while the other shell radius decreases. In addition to shifting of secondary peaks, recombination of one of the secondary peaks originating from the fourth peak with the fifth peak can be clearly seen at the elastic strain levels of 0.050 and 0.075 (Figure 3.5a). This suggests that the coordination shells gets dissociated and reorganized continuously during elastic deformation of BCC Fe. It is important to mention that the position and amplitude of the first peak remains constant during elastic deformation of <100> BCC Fe nanowire. This indicates that there is no change in the radius (2.47 Å) and number of atoms of the first nearest neighbour shell. Following transition from elastic to plastic deformation, the peak positions in radial distribution function falls back to original positions as observed for zero strain (e.g., plastic strain of 0.085 in Figure 3.5a). All the secondary peaks, which originates during elastic deformation gets quickly merged with the primary peaks at the onset of plastic deformation. This can be clearly seen between the strain levels of 0.080 and 0.085 in Figure 3.5a. Further, a general broadening of peaks has been observed during the plastic deformation (e.g., at strain level of 0.085 in Figure 3.5a). Unlike elastic deformation, the peak shifting or peak splitting has not been observed during plastic deformation of BCC Fe nanowires.

Splitting of primary RDF peaks into secondary peaks followed by shifting of secondary peaks has also been observed during elastic deformation of <110> and <111> BCC Fe nanowires (Figures 3.5b-c). In these two orientations, multiple splitting of fourth peak centered at the distance of 4.74 Å with increase in elastic strain leading to multiple secondary peaks can be seen in Figure 3.5b-c. Higher number of splitting and formation of multiple secondary peaks results in the wavy appearance of RDF in <110> oriented BCC Fe nanowire (Figure 3.5b). Like <100> orientation, both <110> and <111> displayed recombination of secondary peaks with increase in elastic strain. Further, at the onset of plastic deformation, all the secondary peaks merged with the primary peaks (e.g., at the strain levels of 0.148 in Figure 3.5b and 0.248 in Figure 3.5c). Similar to the present study, the peak splitting and shifting of secondary peaks have been reported during the elastic deformation of <100> Au [108], <100> Mo [109] and <100> Pd-Pt [110] nanowires.

Table 3.1: Variation of Young's modulus, yield strength and strain to yielding with respect to orientation and loading mode in BCC Fe nanowires. The values of Young's modulus and yield strength available in literature on BCC Fe [16, 107] are given in small brackets.

Orientation	Loading	Young's modulus, GPa	Yield strength, GPa	Strain to yielding
<100>	Tension	164 (155 [107])	12.3 (12.6 [107])	8%
	Compression	162	31.8	19.4 %
<110>	Tension	195 (210 [16])	18.5	14.6%
	Compression	198	22.72	9%
<111>	Tension	288 (285 [107])	27.2 (27.3 [107])	24.5%
<112>	Tension	212 (227 [16])	17.05	13.4%
<102>	Tension	186	15.10	8.7%

Under tensile loading, BCC Fe with <100> orientation exhibited the lowest yield strength of 12.3 GPa, while the <111> orientation showed the highest yield strength of 27.2 GPa. The yield strength values for other orientations fall between these two values. A good agreement between the yield strength values obtained for <100> and <111> orientations with those reported for the respective orientations based on Ab-initio calculations by Friak et al. [107] can be seen in Table 3.1. The variations in strain to yielding followed a trend similar to that observed for yield strength. For <100> orientation, significantly higher yield strength and strain to yielding under compressive loading than tensile loading has been observed (Figure 3.4 and Table 3.1). Contrary to this, the <110> nanowire displayed lower strength and strain to yielding under compression than tensile loading. This indicated opposite tension-compression asymmetry in yield strength for <100> and <110> orientations.

3.4 RDF analysis of elastic deformation

In order to examine the atomic rearrangements and structural correlations, the radial distribution function (RDF) has been calculated at various macroscopic strains during the elastic deformation of BCC Fe nanowires with <100>, <110> and <111> orientations (Figure 3.5). In all the orientations, the radial distribution function at zero applied strain (i.e., without external load) display peaks at 2.47, 2.855, 4.04, 4.74 and 4.95 Å. These peaks corresponds to first nearest neighbour shell at a distance of $\sqrt{3}a/2$, second shell at a distance of a, third shell at a distance of $\sqrt{2}a$, fourth shell at a distance of $\sqrt{11}a/2$ and fifth nearest neighbour shell at a distance of $\sqrt{3}a$ with respect to an arbitrary atom in BCC Fe. During elastic deformation
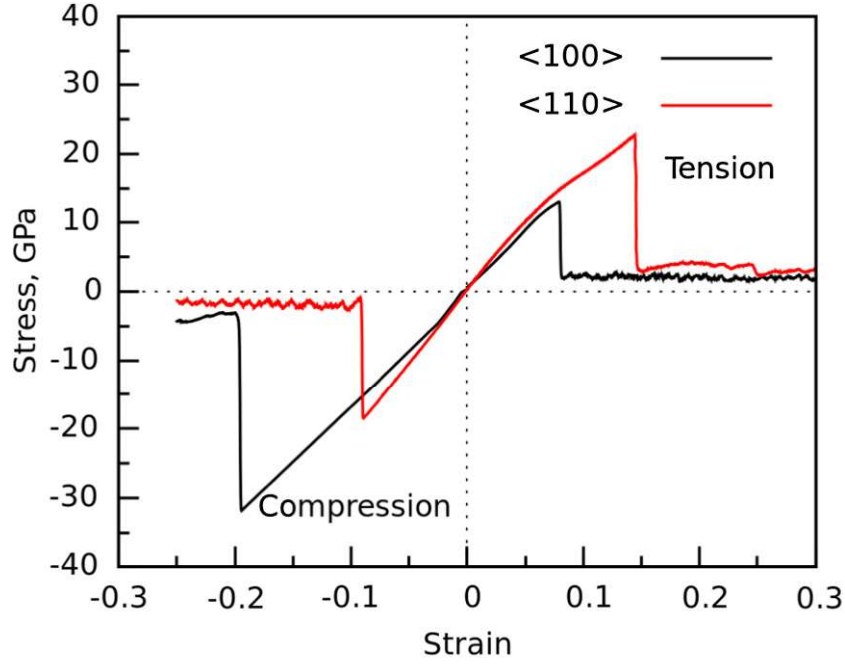
Figure 3.4: Stress-strain behaviour of <100> and <110> BCC Fe nanowires under tensile and compressive loadings at 10 K.

under compression than tension.

The peak value obtained at the end of elastic deformation has been taken as the yield strength of defect free nanowires, and the corresponding strain at which the abrupt stress drop occurred has been considered as strain to yielding. In view of the occurrence of non-linearity, the values of Young's modulus for different orientations have been evaluated from the slope of initial linear elastic regime. The measured values of the Young's modulus, yield strength and strain to yielding under tensile and compressive loadings for various orientations are presented in Table 3.1. The relevant data for Young's modulus and yield strength available in literature on BCC Fe [16, 107] are also given in small brackets. The <100> orientation exhibited minimum Young's modulus of 164 GPa followed by an increase in the order <102>, <110>, <112>, and <111>. The <111> orientation displayed the highest modulus of 288 GPa. No significant influence of loading mode, i.e., tension and compression on Young's modulus has been noticed. Further, a reasonable agreement between the values of Young's modulus evaluated in the present study and those obtained using elastic constants [16] and Ab-initio calculations [107] can be seen in Table 3.1. The large variations in Young's modulus with respect to orientation indicate the presence of high elastic anisotropy in BCC Fe nanowires. The orientation dependence of Young's modulus arises from the inter-atomic forces that vary differently in different directions of a single crystal.
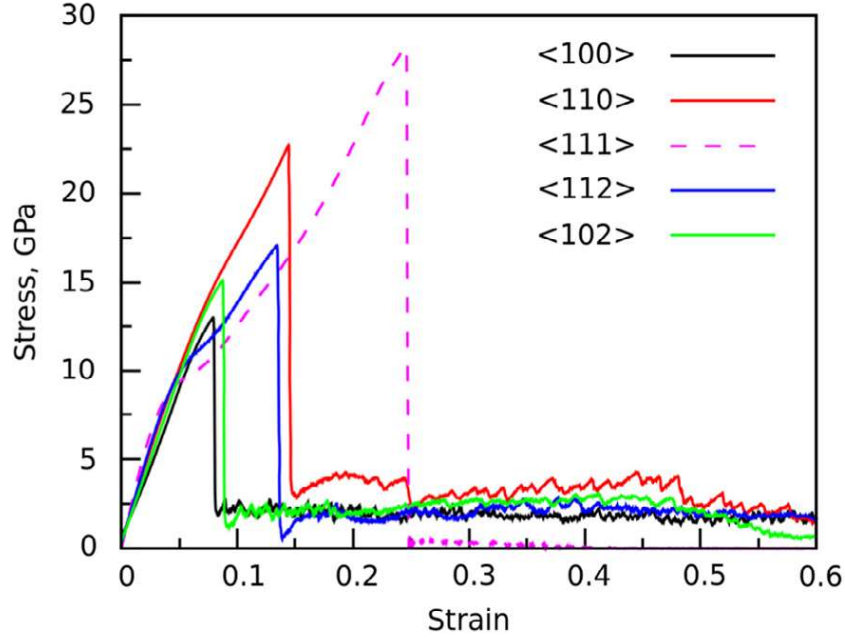
Figure 3.3: Stress-strain behaviour of BCC Fe nanowires with different orientations under tensile loading at 10 K.

regime in terms of both stress and strain followed by increase in the order of <102>, <112>, <110> and <111>. The <111> nanowire displayed the highest elastic regime. In addition to above, all the nanowires show non-linear behaviour at high elastic strains (Figure 3.3). The non-linearity in <100> and <102> orientations occurred only at the end of elastic deformation and an increased non-linearity can be seen for <110> nanowire. The <112> and <111> nanowires exhibited large non-linearity in terms of higher deviations from the initial elastic regime. Following elastic deformation, the abrupt drop in stress indicated the occurrence of yielding in all the nanowires. After yield drops, <100>, <112> and <102> nanowires exhibited nearly constant stress response, while the <110> nanowire displayed small flow stress oscillations during plastic deformation. The flow stress dropping abruptly to zero immediately after the yielding can be seen for <111> oriented nanowire (Figure 3.3).

In order to examine the influence of loading mode on deformation behaviour of BCC Fe nanowires, the stress-strain curves under tensile and compressive loadings for <100> and <110> orientations are shown in Figure 3.4. The nanowires in compression undergo an elastic deformation up to peak stress followed by yielding and progressive plastic deformation at low stresses. Unlike tensile deformation, insignificant non-linearity in the elastic deformation under compressive loading can be seen in Figure 3.4 for both the orientations. For <100> orientation, a significantly higher elastic deformation regime in terms of both stress and strain ranges has been observed. Contrary to this, the <110> nanowire displayed reduced elastic deformation

61

The realistic atomistic simulations were limited in size and time scale, however, the careful choice of size can be used to obtain the important insights into the deformation mechanisms. All the nanowires in the present study have an initial dimensions of $8.5 \times 8.5 \times 17$ nm^3 ($30a \times 30a \times 60a$, where $a = 2.855$ Å is lattice parameter of BCC Fe). Correspondingly, the simulation box contains about 110000 Fe atoms arranged in BCC lattice. Periodic boundary conditions were chosen only along the wire axis, while the other directions were kept free in order to mimic an infinitely long nanowire. Following the initial construction of the nanowire, energy minimization was performed by conjugate gradient (CG) method. The stable structure thus obtained was thermally equilibrated to a required temperature of 10 K in canonical ensemble (constant NVT). Working at low temperature of 10 K provide several advantages in terms of comparison with Ab-initio data, stress calculation, minimal temperature fluctuations and post-processing of simulation data. Velocity Verlet algorithm was used to integrate the equation of motion with a time step of 5 fs. Upon completion of the equilibration process, the deformation is carried out at constant strain rate of 1×10^8 s^{-1}. The tensile loading was applied by constantly deforming the box along the nanowire axis (Method -1, Section 2.6) for all the five orientations i.e. <100>, <110>, <111>, <112> and <102>. In order to study the influence of loading mode on the deformation behaviour, MD simulations were also performed with compressive loading applied along the nanowire axis for <100> and <110> orientations. During the loading, the atomic system was allowed to deform naturally at a constant strain rate without imposing any stress constraints in the other two directions. The stress was calculated from the Virial expression of stress as given in Equation 2.27, which is equivalent to a Cauchy's stress in an average sense. The RDF analysis has been carried out in OVITO [103]. AtomEye package [102] was used for the visualisation of atomic snapshots with coordination number, centro-symmetry parameter and common neighbour analysis (Section 2.8).

3.3 Stress-strain behaviour

The stress-strain curves under tensile loading of BCC Fe nanowires with <100>, <110>, <111>, <112> and <102> orientations at 10 K are shown in Figure 3.3. In general, the stress-strain behaviour of all the nanowires is characterised by initial elastic deformation up to peak stress followed by large and abrupt stress drop and then progressive plastic deformation at low stresses. However, the elastic regime has shown significant differences with respect to orientation. The nanowire with <100> orientation showed the smallest elastic deformation

Finnis-Sinclair (FS) type many body potential. The potential was fitted to the properties obtained using first-principles calculations in a model liquid configuration and also to other experimentally obtained material properties of solid BCC Fe. Further, the use of Mendelev EAM potential is strengthened by the fact that with this potential the deformation in <100> BCC Fe nanowires proceeds by twinning [60–62] and this is in agreement with the reported observations in <100> BCC W nanowire [63].

In order to examine the orientation dependence of deformation mechanism in BCC Fe nanowires, different axial orientations of <100>, <110>, <111>, <112> and <102> have been considered. Figure 3.2 shows the initial orientations and surface structure of the nanowires. For <100> orientation, all four surfaces were of {100} type (Figure 3.2a). The <110> oriented nanowire was enclosed by two {112} and two {111} surfaces (Figure 3.2b), while <111> oriented nanowire contained two {112} and two {110} as its side surfaces (Figure 3.2c). Similarly, the <112> oriented nanowire was enclosed by two {111} and two {110} surfaces (Figure 3.2d), while the <102> oriented nanowire has two {102} and two {100} side surfaces (Figure 3.2e). The structures of all these surfaces are in good agreement with those reported by Blonski and Kiejna [83] using density functional theory calculations. At the atomic scale, the surface structures become important for determining the orientation of the reoriented regions due to deformation twinning.
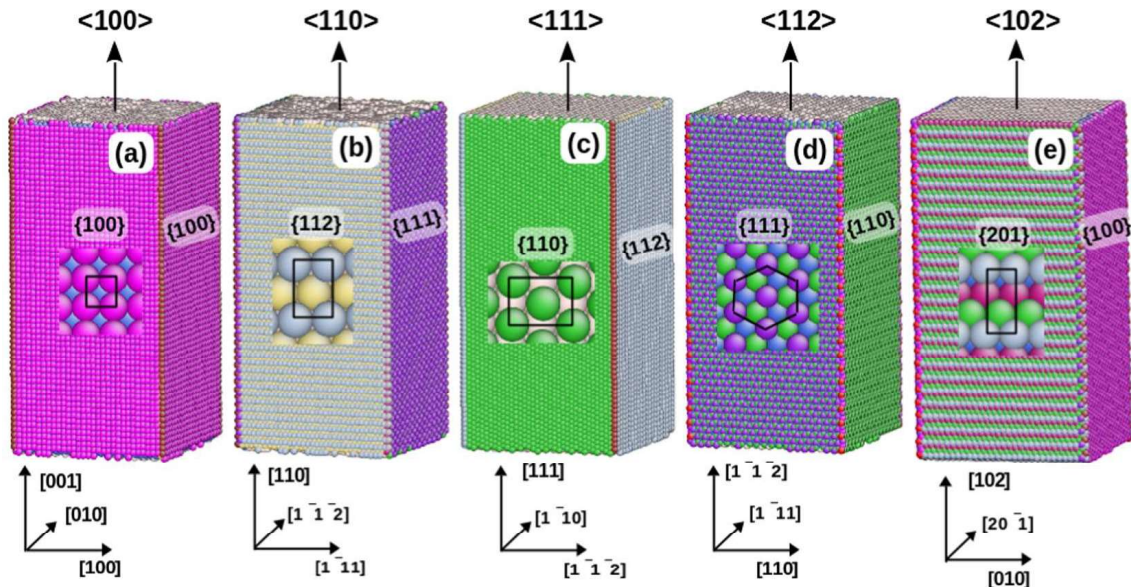
Figure 3.2: The initial orientations and surface structures of the nanowires considered in this study are shown for (a) <100>, (b) <110>, (c) <111>, (d) <112>, and (e) <102> axial orientations. The atoms are coloured according to their number of coordination number. The insets in figures show the basic unit cell of the atomic arrangement at the surface of nanowire.

has chosen different orientations on the standard stereographic triangle. It has been shown that at room temperature and conventional strain rates, the plastic deformation occurs by dislocation slip, irrespective of the single crystal orientation. Whereas, increase in strain rate and/or, decrease in temperature promoted deformation twinning and the extent of twinning depends strongly on crystal orientation (Figure 3.1). The orientations close to <001> tensile axis show extensive twinning, whereas the orientations near <110> and <111> tensile axes do not display any twinning (Figure 3.1). In order to compare the nanowire results with their bulk counterparts, five different orientations, <100>, <110>, <111>, <112> and <102> of BCC Fe nanowires falling on different regions of standard stereographic triangle have been chosen in this study. Based on the obtained results, for first time, we show that the orientation dependent deformation under the tensile and compressive loading of BCC Fe nanowires can be explained based on the twinning-antitwinning asymmetry of $1/6<111>$ partial dislocations on {112} planes. Further, the radial distribution function (RDF) analysis has been performed to examine the elastic deformation of BCC Fe nanowires with respect to orientation.
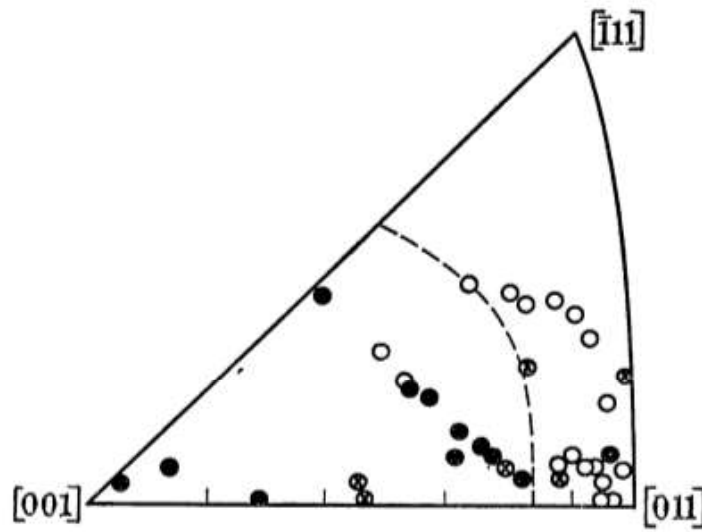
Figure 3.1: Orientation dependence of twinning behaviour in bulk iron single crystals at room temperature and dynamic strain rate of 1×10^3 s^{-1} [106]. • - twinned specimen, ○ - untwinned specimen and ⊗ - specimens with very few twins.

3.2 Simulation details

Molecular dynamics (MD) simulations have been carried out in LAMMPS package [94] employing an embedded atom method (EAM) potential for BCC Fe given by Mendelev and co-workers [75]. As discussed in Section 2.2.3, this potential is based on the framework of a

Chapter 3

Influence of orientation and mode of loading on deformation behaviour of BCC Fe nanowires

3.1 Introduction

In FCC metals, the slip occurs on {111} planes in <110> directions and the planar nature of the dislocation cores makes slip on these planes relatively easy. Further, FCC materials obey Schmid's law and there have been many experimental and atomistic simulation studies pertaining to the deformation behaviour of FCC nanowires [10, 11, 25–27]. All these studies have concluded that the orientation dependent deformation behaviour in FCC nanowires can be explained based on the Schmid factor analysis (Section 1.3.1). In BCC metals, slip occurs in <111> direction on {110}, {112} and {123} planes, and the non-planar nature of screw dislocation core makes the slip more complex. The core of 1/2<111> screw dislocations in BCC metals spreads into several non-parallel planes of <111>. As a result, the glide of a screw dislocation depends on the shear stress in slip direction along with the stress perpendicular to the slip direction (called as non-glide or non-Schmid stresses). Due to this non-glide stresses, the dislocation motion in BCC metals do not obey the Schmid's law (Section 1.3.2). As a result, the orientation dependence of deformation behaviour in Fe or any other BCC nanowires has not been understood completely. Further only two or three orientations have been investigated in previous studies [57, 59–63]. In view of this, the tensile and compressive deformation of BCC Fe nanowires has been examined for five different orientations in the present study.

In the past, Harding [106] studied the orientation dependent deformation behaviour of bulk high purity iron single crystals at different temperatures ranging from 77 K to 300 K and two different strain rates of 1×10^{-3} s^{-1} (conventional) and 1×10^{3} s^{-1} (dynamic). He

57

4.5   Conclusions

Molecular dynamics simulations have been performed to examine the size effects in $<100>$ and $<110>$ BCC Fe nanowires. Investigations on $<100>$ BCC Fe nanowires indicated the presence of two different behaviours as a function of size. The small size nanowires up to d = 11.42 nm deform by twinning at low strains followed by reorientation due to the activation of single twin system. Following the reorientation, the deformation mode shifts from twinning to slip at higher strains and this results in high ductility and failure by necking. On the other hand, the large size nanowires beyond 11.42 nm, deforms by twinning on multiple twin systems, which disrupts the reorientation process. The twin-twin interaction leads to early crack nucleation and cleavage failure resulting in lower ductility in large size nanowires. The twin growth occurs by the repeated initiation and glide of $1/6<111>$ twinning partial dislocations along the adjacent $\{112\}$ planes. The variations in twin propagation stress indicated that twin growth is easier in large size nanowires as compared to that in small size nanowires.

Contrary to $<100>$ nanowires, the size effects on $<110>$ BCC Fe nanowires were minimal. The yielding in all the nanowires occurred through the collective emission of dislocations followed by the slip of $1/2<111>$ full dislocations. With increasing plastic deformation, the accumulation of large number of straight screw dislocations has been observed irrespective of the nanowire size. Further in large size nanowires, the cross-slip has been noticed in the form of curved slip steps on the nanowire surface. However, the cross slip was not observed in small size nanowires. Finally, all the $<110>$ BCC Fe nanowires failed in ductile manner.

The variations in Young's modulus and yield strength with respect to size in $<100>$ and $<110>$ BCC Fe nanowires show contrasting behaviour. The Young's modulus and yield stress in $<100>$ orientation undergoing twinning mode of deformation decreases rapidly with increase in nanowire size up to 11.42 nm followed by gradual decrease towards saturation at larger sizes. On the other hand in $<110>$ orientation displaying deformation by slip, the Young's modulus and yield strength exhibited a rapid increase with increase in size for small size nanowires followed by saturation at larger sizes. The variations in yield strength has been explained based on the effects associated with surface stress, surface energy and number of defect nucleation sites.

total surface area of the nanowire (i.e. $4\times$ length $\times$ cross-section width) [59, 83, 136]. It can be seen that, like yield strength, the surface energy also increases rapidly in small size nanowires followed by saturation at larger sizes. The low surface energy in small size nanowires facilitates easy defect nucleation and results in lower yield strength values. On the other hand, the high surface energy in large size nanowires makes the defect nucleation more difficult and leads to higher yield strength.
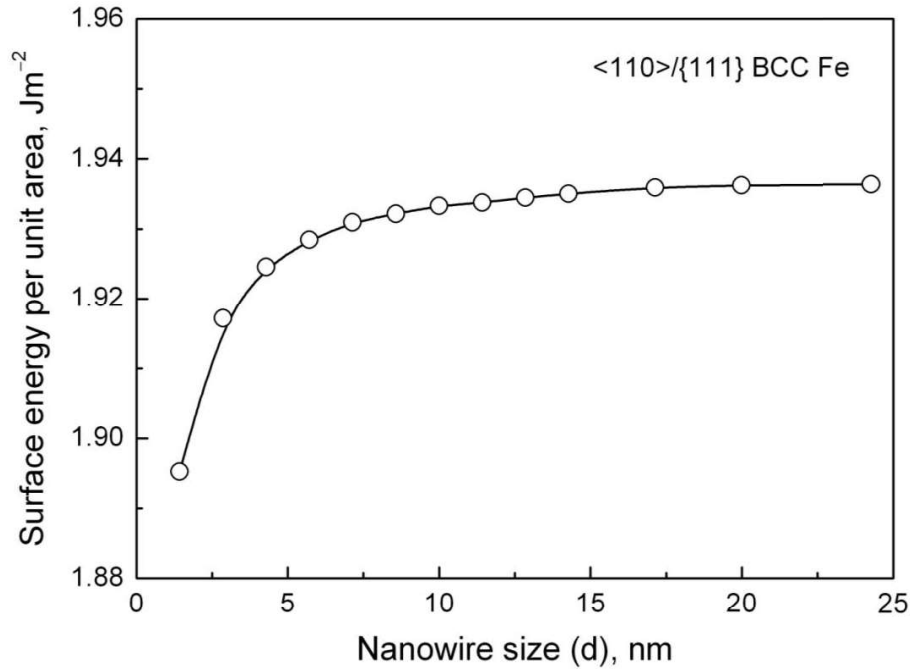
Figure 4.17: Variation of surface energy as a function of cross section width (d) for $<110>/\{111\}\{112\}$ BCC Fe nanowires at 10 K.

Depending on the surface orientations, the surface energy may increase or, decrease or, it may remains constant with increasing size or thickness [59, 83, 136]. In BCC Fe, it has been shown that the surface energy of $\{111\}$ surfaces increases with increase in film thickness followed by saturation, while the surface energy of $\{112\}$ surfaces vary insignificantly with respect to film thickness [83]. This justifies the observed increase in surface energy of $<110>$ BCC Fe nanowire, which is enclosed by $\{111\}$ and $\{112\}$ surfaces. Contrary to $\{111\}$ and $\{112\}$ surfaces, the surface energy of $\{100\}$ BCC Fe surfaces decreases with increasing thickness, and thus results in "smaller is stronger" trend in $<100>$ BCC Fe nanowires (Figure 4.2b), which is enclosed by all $\{100\}$ surfaces. Therefore, the observed variations in yield strength can be attributed to the variations in surface energy of BCC Fe nanowires.

4.4.3 Dislocation cross-slip in large size nanowires

The observed increase in number of slip steps and slip bands with increasing size indicates higher dislocation activity in large size nanowires (Figure 4.14). Further, the presence of the curved nature of slip steps in large size nanowires signifies the occurrence of cross slip (Figure 4.14c). The occurrence of cross slip in large size nanowires and its absence in small size nanowires can be explained by the mobility of screw dislocations in BCC nanopillars [132]. It has been suggested that the mobility of screw dislocations increases with increase in surface area to volume ratio, and may approach towards the mobility of edge dislocations [132]. Due to high mobility and less travel distance, the dislocations in small nanowires may easily escape to the surface without undergoing cross slip. Further, the dislocations in small size nanowires deviate from pure screw character thereby hindering their ability to cross-slip [111]. In contrast, the dislocations in large size nanowires travel higher distances, thereby by increasing their probability to cross-slip. In addition to this, the low mobility screw dislocations facilitates the pile-up and this increases the tendency to cross-slip in the large size nanowires. Similar to the present study, Kim et al. [113] demonstrated the size effect in terms of the occurrence of parallel slip lines in small size nanopillars and wavy slip lines in the large size Mo nanopillars.

4.4.4 Size dependent strength of <110> nanowires

Generally, the yield strength of metallic nanowires decreases with increasing size, thereby showing the "smaller is stronger" trend. However, the observed reverse trend of "smaller is weaker" in the present investigation is interesting. Similar trend has been reported in <110> and <111> BCC Mo nanowires [130]. This indicates that all the <110> BCC nanowires may show similar behaviour in yield strength. The smaller is weaker trend has also been observed in HCP Ti and FCC Au nanopillars [133–135] and this has been explained based on the variations in surface energy with nanopillar size in HCP Ti [135]. In general, the energy required to nucleate a dislocation (U) is the sum of unstable stacking fault energy (U_{USF}) and surface energy (U_S) i.e., $U = U_{USF} + U_S$ [59]. However, the U_{USF} doesn't change with size. Therefore, the energy required to nucleate a dislocation from the surface is directly proportional to surface energy. The surface energy of <110> BCC Fe nanowires as a function their size has been evaluated and presented in Figure 4.17. Here, the surface energy (U_S) has been evaluated as $U_S = (E_N - E_B)/A$, where E_N is the potential energy of the nanowire (periodic only along the length), E_B is the potential energy of the bulk sample (periodic in all directions) and A is the
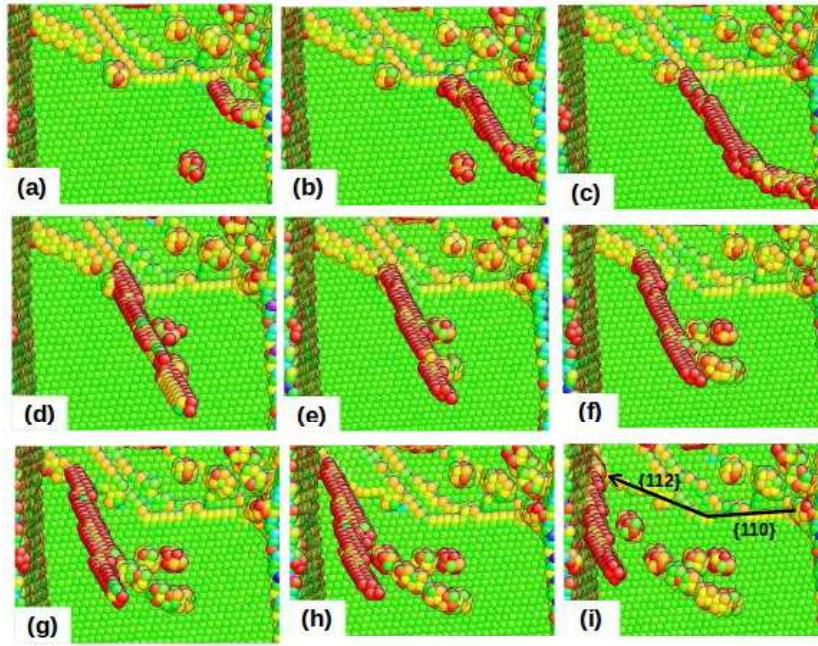
Figure 4.15: The sequential process of screw dislocation motion in large size <110> BCC Fe nanowires (d = 17.13 nm) showing cross-slip of dislocation from {110} plane to {112} plane. Creation of large number of point defects can be seen in (e-i).
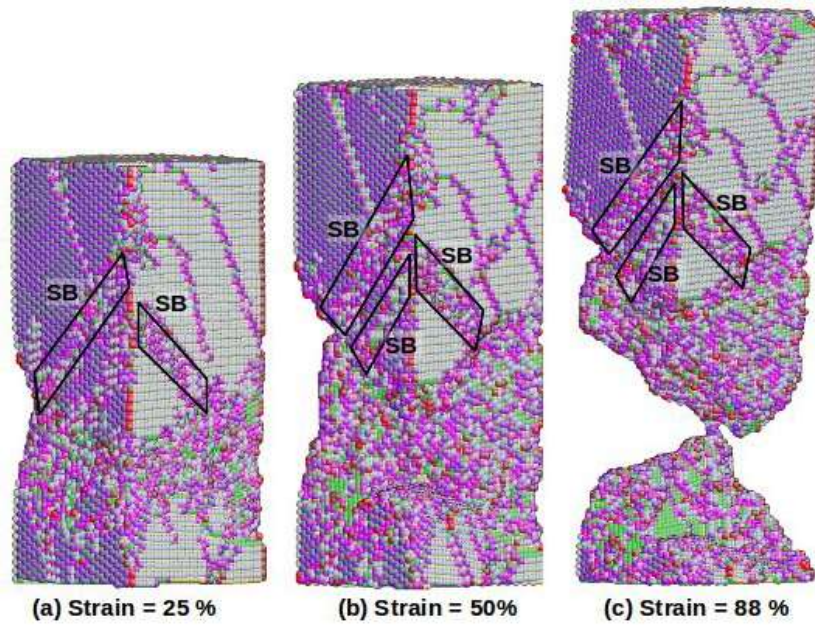
Figure 4.16: The plastic deformation behaviour in <110> BCC Fe nanowire width d = 8.5 nm as a function of strain: (a) 25%, (b) 50% and (c) 88%. The slip steps due to escape of dislocations can be seen in (a). The intersecting slip lines due to the activation of multiple slip can be seen in (b). Failure by necking can be seen in (c). The atoms are coloured according to their coordination number.
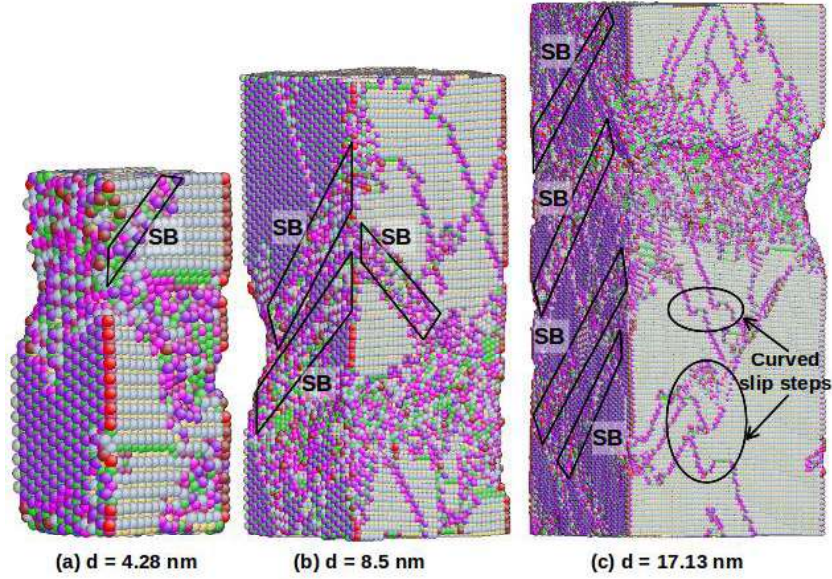
Figure 4.14: The deformation behaviour in <110> BCC Fe nanowires as a function cross-section width (a) d = 4.28, (b) 8.5 and (c) 17.13 nm at 20% strain. Increased number of slip steps (ST) and slip bands (SB) with increase in the nanowire size can be seen. Curved slip steps at large size nanowire can be seen in (c). The atoms are coloured according to their coordination number.

slip in large size nanowires. Slip steps having curved profile were not observed in small size nanowires (Figure 4.14a and b). The occurrence of cross-slip in large size nanowires is shown using sequential snapshots displaying the glide of a screw dislocation in Figure 4.15. The initial glide of screw dislocation on {110} plane can be seen in Figure 4.15a-c. With increasing deformation, the cross-slip of dislocation onto {112} plane can be seen through Figure 4.15d-i. The trace of cross-slip of dislocation from {110} to {112} plane is explicitly presented in Figure 4.15i. The cross slip of screw dislocation creates a curved/non-straight slip steps on the surface as shown in Figure 4.14c. Presence of jogs and kinks on screw dislocation can also be seen in Figure 4.15. Since, the jogs on screw dislocation have an edge orientation, the only way the screw dislocation can move along with jogs is by non-conservative motion. The non-conservative motion of dislocations leads to the creation of point defects such as vacancies and/or, interstitials. The formation of large number of point defects can be seen in Figure 4.15d-i. Similar mechanism of dislocation motion by leaving many point defects behind has been observed in BCC Fe at high stress levels in the range 0.6-1.8 GPa and it has been termed as rough and jerky motion [55]. Localisation of multiple slip events leads to gradual reduction in cross-sectional area and the early onset of necking with increase in deformation (Figures 4.16a and b). Further deformation in localized neck region results in the pronounced necking and failure as shown in Figure 4.16c.
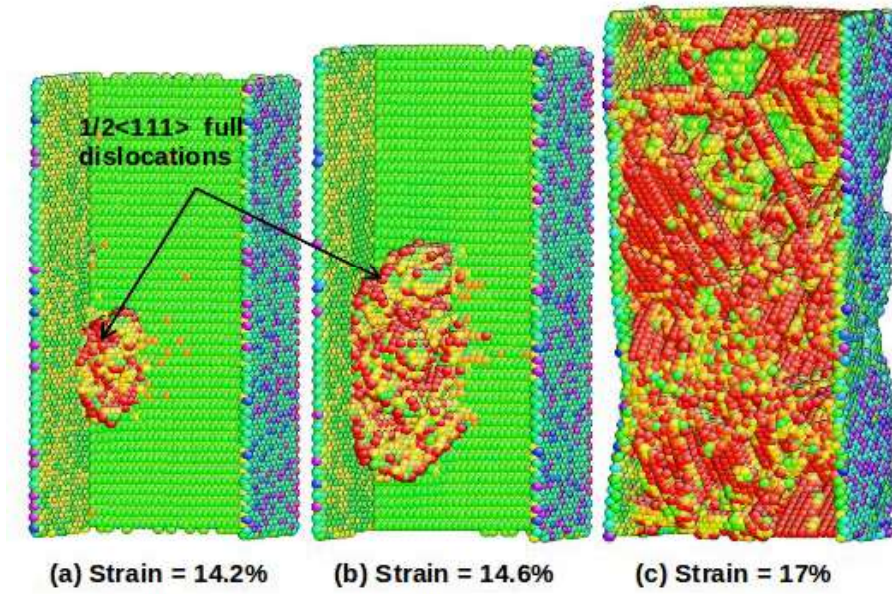
Figure 4.12: The yielding and subsequent plastic deformation behaviour in <110> BCC Fe nanowire having cross section width d = 8.5 nm. The yielding through the collective emission of dislocation loops from the corner of the nanowire can be seen in (a). Subsequent glide of dislocations loops and the pile up of straight screw dislocations can be seen in (b) and (c), respectively. The atoms are coloured according to the centro-symmetry parameter (CSP). The perfect BCC atoms and the front surface were removed for clarity.
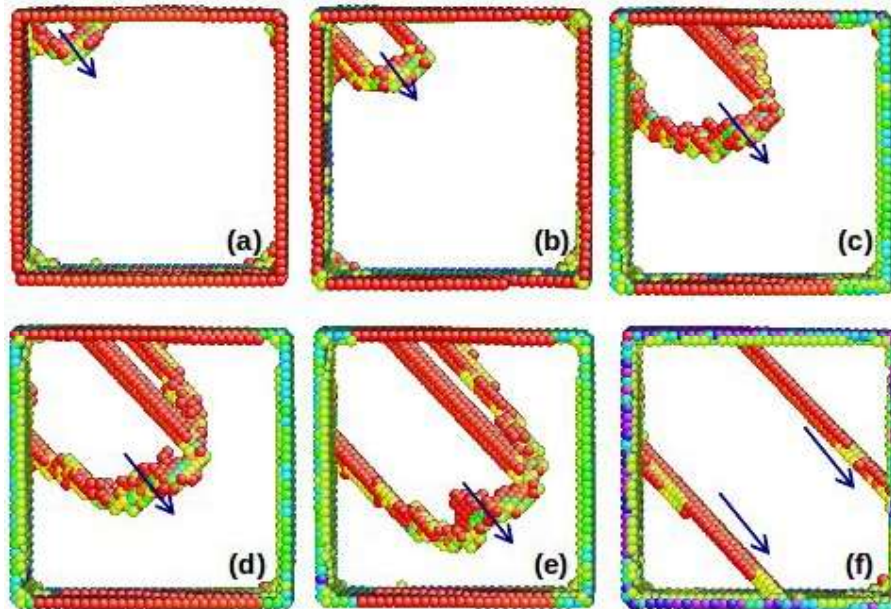
Figure 4.13: The plastic deformation in <110> BCC Fe nanowire having cross-section width d = 8.5 nm. The formation of straight screw dislocation can be seen in (a-f). The perfect BCC atoms are removed for clarity and the blue arrows indicate the Burgers vector.

94

4.4.2 Deformation and failure behaviour

The deformation behaviour in <110> BCC Fe nanowires was governed by dislocation slip mechanism irrespective of nanowire size in the range 1.42-24.27 nm. The atomic configurations following yielding and subsequent plastic deformation are typically shown for the nanowire cross section width, d = 8.5 nm in Figure 4.12. The onset of yielding is characterised by the nucleation of collective dislocation loops originating from the corner of the nanowires (Figure 4.12a). Since, there are no obstacles in the early stage of plastic deformation, avalanche of dislocations loops easily expand in multiple directions as shown in Figure 4.12b. With increase in deformation, accumulation of large number of straight screw dislocations can be seen in Figure 4.12c. The process of the accumulation of straight screw dislocations is typically shown by considering a single dislocation loop in Figure 4.13. The dislocation loops initially nucleate from the corner consist of edge as well as screw components. The blue arrow indicating the Burgers vector shown in Figure 4.13 distinguishes the edge and screw components of the dislocation loop. The dislocation analysis [104] indicated that the loop has a Burgers vector 1/2<111> describing full dislocations in BCC system. With increasing strain, the growth of dislocation loop leads to increase in the length of screw component (i.e., the straight region) as shown in Figure 4.13b-e. Since, edge dislocations in BCC metals inherently exhibit higher mobility than the screw dislocations, the edge component of mixed dislocations easily escapes to the surface. During the expansion of dislocation loop, the edge component approaching towards the surface and its annihilation at the surface can be seen in Figure 4.13e and f, respectively. As a result, only screw component of a dislocation loop remains in the nanowire (Figure 4.13f). The accumulation of screw dislocations as seen in Figure 4.12c results from this process in <110> BCC Fe nanowires. The accumulation of straight screw dislocations observed in <110> BCC Fe nanowires is in agreement with those reported in Mo and Ta nanopillars [111,113]. In BCC nanopillars, the accumulation of straight screw dislocations has been described using mesoscopic model by Groger and Vitek [131] and kinetic pile up model by Kaufmann et al. [111].

The surface morphology displaying the presence of slip steps (ST) and slip bands (SB) for different nanowire sizes are shown in Figure 4.14. A significant increase in the number of slip steps and slip bands with increasing size can be seen. In addition to above, slip steps having curved profile can also be seen in Figure 4.14c in nanowires with d > 11.42 nm. The presence of slip steps with curved profile provides an evidence for the occurrence of cross-

different behaviour of modulus in <100> and <110> directions has been attributed to the individual contributions of edges, surfaces and core to total elasticity [117]. The saturation value of Young's Modulus (203 GPa) at large sizes (Figure 4.11a) compares favourably with 210 GPa obtained using elastic constants in <110> direction of BCC Fe [16]. Similar to Young's modulus, the size dependence of yield stress in <110> nanowires also shows a rapid increase in small size nanowires followed by saturation at larger sizes (Figure 4.11b). The variation of yield strength as a function of size is in agreement with those reported recently in <110> and <111> BCC Mo nanowires [130].
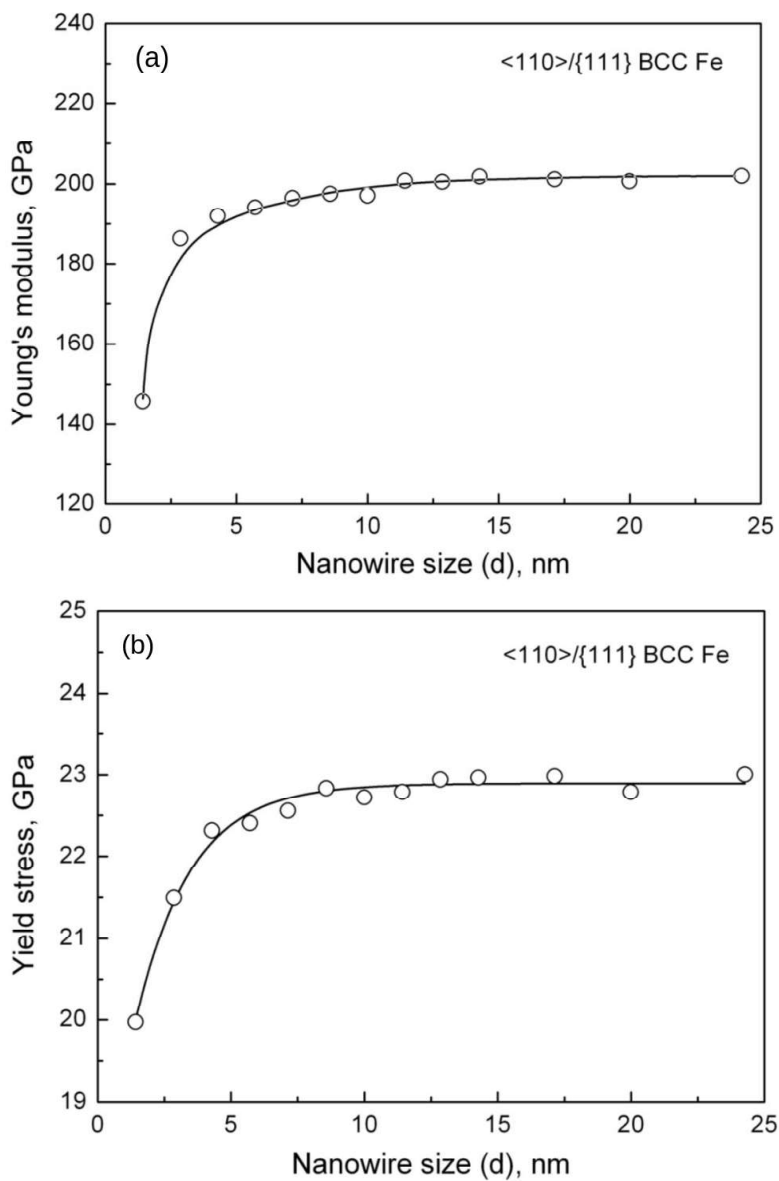
Figure 4.11: Variation of (a) Young's modulus and (b) yield strength as a function of cross section width (d) in <110> BCC Fe nanowire at 10 K.

The deformation mechanisms analysed for different nanowire sizes have been presented.

4.4.1   Stress-strain behaviour

The stress-strain curves of <110> BCC Fe nanowires with cross-section width (d) ranging from 1.42 to 24.27 nm are presented in Figure 4.10. The stress-strain behaviour of all the nanowires is characterized by initial elastic deformation up to peak stress followed by an abrupt drop to low values of stress, indicating yielding in the nanowires. The abrupt yield drop occurs at a constant strain value 14.2%, irrespective of the nanowires size. The yielding is followed by a progressive plastic deformation leading to gradual decrease in flow stress till failure. Further, a general decrease in strain to failure (ductility) with increase in nanowire size can be seen in Figure 4.10. Unlike <100> nanowires, the stress-strain curves of <110> nanowires show similar behaviour independent of nanowire size in the range 1.42 to 24.27 nm.
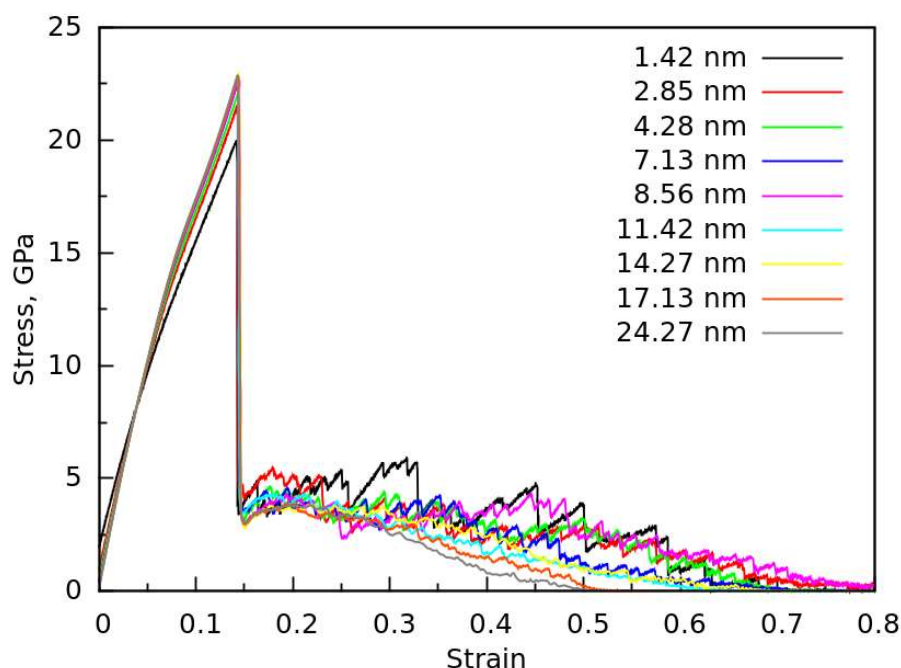
Figure 4.10: Stress-strain behaviour of <110> BCC Fe nanowires of cross-section width (d) in the range 1.42-24.27 nm at 10 K.

The variation of Young's modulus (E) with the cross-section width (d) of <110> BCC Fe nanowires is shown in Figure 4.11a. It can be seen that for small nanowires sizes, the Young's modulus increases rapidly with increase in size followed by saturation at larger sizes. The size dependence of Young's modulus in <110> nanowires is in contrast to that observed for <100> nanowire (Figure 4.2a). The variation of Young's modulus in <100> and <110> directions is consistent with that reported by Olsson et al. [117] in BCC Fe nanobeams. The

91
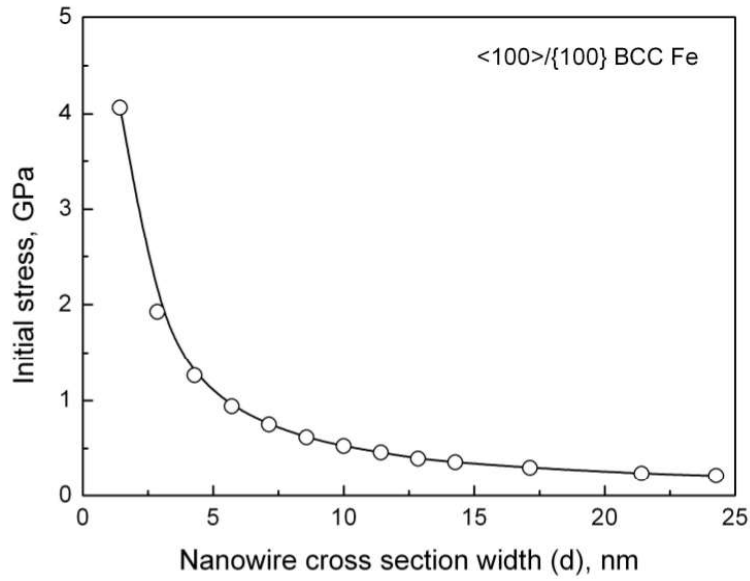
Figure 4.9: Variation of initial stress as a function of cross section width (d) for <100> BCC Fe nanowires at 10 K.

while in small size nanowires the yielding occurs only on one system. This clearly suggests that fewer sites are available for defect nucleation in small size nanowires compared to large size nanowires. The large size nanowires provide higher number of nucleation sites for twin embryos resulting in the lower values of yield strength compared to small size nanowires. The strength reduction by higher number of nucleation sites arises from the effects associated with the higher nucleation attempts and decrease in activation energy for the nucleation process with increase in the nanowire size [127, 129]. In initially defect free nanowires, the defect nucleation from the surface is preferred, and the number of nucleation sites is directly proportional to the nanowire surface area d^2, where d is the cross section width. However, due to energy considerations, the dislocations are not expected to nucleate from all corners in a slip plane. Dislocations nucleate at the corners where the energy per-unit-length of the dislocation happens to be minimum [129]. Removing one dimension from d^2 leads to a scaling of the order d [127], and this provides justification for the obtained inverse correlation between the yield strength and the nanowire cross section width (Figure 4.2b).

4.4   Size effects on dislocation slip - <110> nanowire

In this section, the influence of size on the stress-strain behaviour and deformation mechanisms in <110> BCC Fe nanowire have been presented. The variations in Young's modulus and yield stress are presented as a function of size and explained based on the surface energy calculations.

90

as a result of convergence towards the bulk value. The size dependence of twin propagation stress can be ascribed to the effects associated with decrease in the surface energy difference between the reoriented {112} and the original {100} surfaces with increasing nanowire size [122]. Small size nanowires require higher stresses for the propagation of twin boundaries due to high surface energy difference between the original <100> and the reorientated <110> nanowires. With increasing nanowire size, this surface energy difference between the original and the reoriented region decreases thereby resulting in decrease in twin propagation stress at larger sizes.

4.3.4   Size dependent strength of <100> nanowires

The size dependence of yield strength in nanomaterials can be explained based on the effects associated with surface stress induced by the broken bonds and defect nucleation sites at free surfaces [124–127]. The effect of surface stress (f) on the strength of nanowires can be estimated by obtaining the initial residual stress (r) present in the nanowire, as they are related by a simple relation r = -4f/d, where d is the nanowire width/diameter [124, 125]. The surface stress arises due to the broken bonds on the surface and results in the presence of residual stress in the nanowire core or interior. At equilibrium, the surface stress and residual stress balance each other [125]. In the present study, the presence of intrinsic residual stresses has been observed and this has been shown as the variation in initial stress with nanowire size in Figure 4.9. The initial stress has been taken as the stress in the nanowire at zero strain or before the application of any load. It can be seen that the magnitude of the initial stresses is in the order of GPa and exhibits a rapid decrease in small size nanowires followed by a gradual decrease towards zero at large nanowire sizes. In order to initiate the deformation, the applied stress must overcome the residual stresses present in the nanowires. High residual stresses contribute significantly towards higher yield stress in small size nanowires. However, in large size nanowires, such a contribution appears to be either small or negligible. Koh and Lee [128] and Sutrakar and Mahapatra [41] also observed a similar presence of initial stress in FCC metallic nanowires. These observations suggest that the contribution of surfaces to the strength of the nanowires is significant.

The other important factor, which influences the yield strength is the number of potential nucleation sites for defects [126, 127]. As observed in Figure 4.3, the yielding in large size nanowires (d > 11.42 nm) is associated with the nucleation of multiple twin embryos,

BCC Fe has a displaced structure, as a result each 1/6<111> partial dislocation in Figure 4.6 and 4.7 dissociates into two 1/12<111> partial dislocations lying on adjacent {112} planes as discussed in Chapter 3, Section 3.7.4.

The observed flow stress plateaus in the stress-strain curves results mainly from the twin growth/twin boundary migration along the nanowire axis. Therefore, the average value of the stress during the plateau regime between the strains of 0.1-0.6/0.7 in Figure 4.1a can be considered as the twin propagation stress [122]. The variation in twin propagation stress with nanowire cross section width (d) is shown in Figure 4.8. The twin propagation stress for the smallest size nanowire (d = 1.42 nm) was not considered due to very large stress fluctuations in the stress-strain curve. It can be seen that the twin propagation stress decreases rapidly with increasing size in the small size range (d < 11.42 nm) followed by saturation at larger sizes (Figure 4.8). This suggests that, once the twin nucleates, the twin growth remains easier in large size nanowires compared to that in small size nanowires. Similar variations in twin propagation stress have been observed in Au, Pd and AuPd nanowires [122]. Using the observed values of
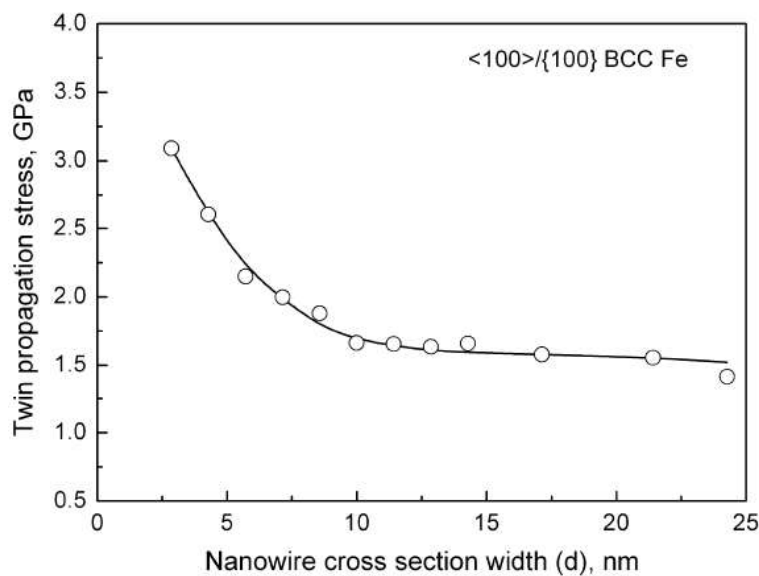
Figure 4.8: Variation of twin propagation stress as a function of cross section width (d) for <100> BCC Fe nanowires at 10 K.

twin propagation stress, the corresponding resolved shear stress for twin propagation on {112} planes has been evaluated. A systematic decrease in the resolved shear stress from 565 MPa for the nanowire with d = 2.85 nm to 146 MPa for the nanowire with d = 24.27 nm has been obtained. Experimentally, Patriarca et al. [123] reported the resolved shear stress of 114 MPa for the twin boundary migration in a considerably large size FeCr single crystal. Therefore, the observed saturation in the twin propagation stress at larger nanowire sizes can be considered

(a) d = 8.5 nm   (b) d = 17.13 nm
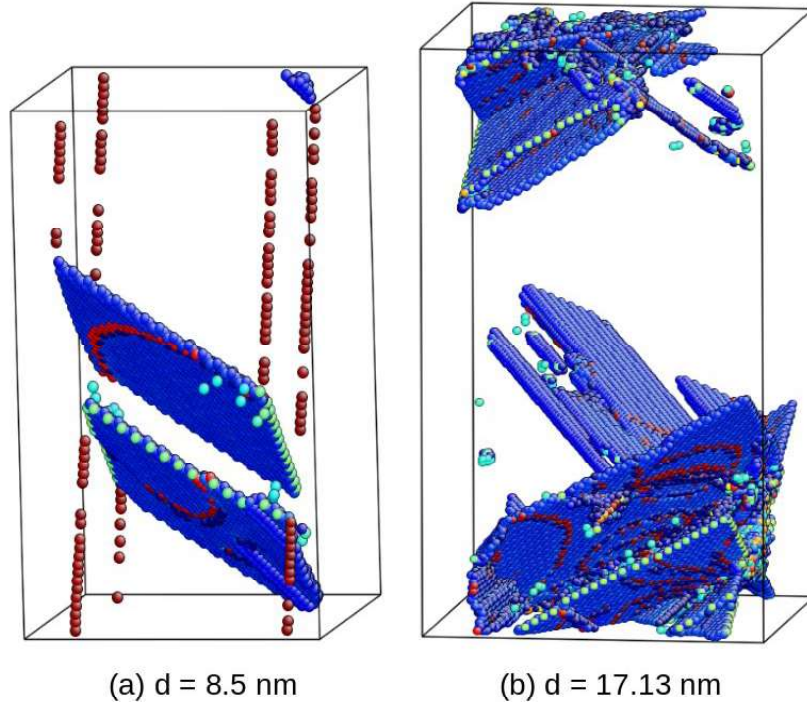
Figure 4.6: Dislocation activity along the twin boundaries in <100> BCC Fe (a) small size nanowire with d = 8.5 nm and (b) large size nanowire with d = 17.13 nm. The gliding of only one twinning partial on each twin boundary in small size nanowires and multiple twinning partials in large nanowires can be seen.

(a)   (b)   (c)   (d)
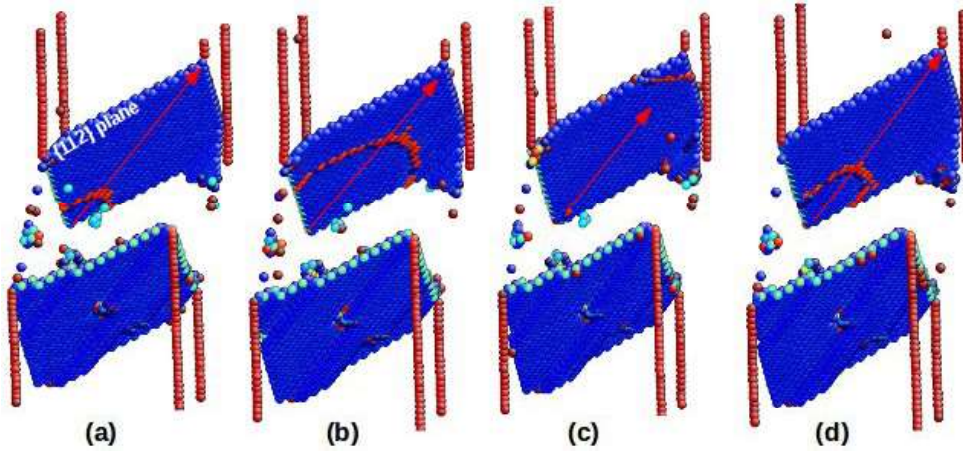
Figure 4.7: The repeated initiation and glide of 1/6<111> twinning partial dislocations along the {112} planes in small size nanowire with d = 8.5 nm showing (a) nucleation of 1/6<111> twinning partial dislocation from the nanowire corner (b) glide of twinning partial along twin boundary (c) annihilation at the opposite surface and (d) nucleation and glide of next twinning partial dislocation on adjacent {112} plane. The atoms are coloured according to centro-symmetry parameter (CSP) and the perfect BCC atoms and surfaces are removed for clarity. Blue atoms represent twin boundaries ({112} planes), red atoms are nanowire corners and pink atoms represent twinning partial dislocation. Pink arrow represents <111> direction.

tems in large size nanowires restricts the twin growth and reorientation process leading to low failure strains or ductility. The activation of multiple twin systems at the same time in large size <100> nanowires is expected because of identical Schmid factor of 0.471 on four <111>/{112} twin systems. However, the activation of only one twin system in small size nanowires is interesting and it may arise due to source truncation/source limitation as proposed in FCC nanowires [47–49]. Due to the activation of only one system in small size nanowires, the twin boundaries do not face any barriers in their movement and were able to sweep across the nanowire length, thus reorienting the initial <100> nanowire into a <110> nanowire. This reorientation facilitate the occurrence of second elastic peak and further deformation by slip leading to high values of ductility in excess of 100% in small size nanowires.

4.3.3   Twin growth and twin propagation stress

Figure 4.6 shows the glide of 1/6<111> twinning partial dislocations on twin boundaries in small and large size nanowires. The small size nanowire consist of two twin boundaries each accompanied with one 1/6<111> partial dislocation (Figure 4.6a). On the other hand the large size nanowires show multiple twin boundaries, each comprising of numerous twinning partial dislocations (Figure 4.6b). Further, the twin boundaries in large size nanowires becomes incoherent and defective due to twin-twin interactions. The incoherent and defective twin boundaries obstruct the glide of 1/6<111> partials dislocations, thus affecting the twin growth and reorientation process in large size nanowires.

The absence of obstacles and coherent structure of twin boundaries in small size nanowires makes it effective to understand the twin growth process. Figure 4.7 shows the process of twin growth in small size (d = 8.5 nm) <100> BCC Fe nanowire. It can be seen that, once the 1/6<111> twinning partial nucleates from the nanowire corner (Figure 4.7a), it propagates further on the twin boundary and gets annihilated at the opposite surface (Figure 4.7b-c). Following the annihilation, the 1/6<111> twinning partial dislocation again nucleates from the nanowire corner but on adjacent plane (Figure 4.7d) and this process repeats until the twinning partials /twin boundaries faces an obstacles. Since there are no obstacles/barriers in small size nanowire (Figure 4.6a), the twin growth process continue till the nanowire gets reorientated. Whereas in large size nanowires, there are many obstacles in the form of incoherent steps, other twin boundaries and point defects (Figure 4.6b), which disturbs the twin growth process leading to crack nucleation. Finally, it is important to note that the twin boundary in

86

The deformation and failure behaviour of <100> BCC Fe nanowires of size (d) = 17.13 nm representing large size nanowires in the range 12.84 - 24.27 nm is shown Figure 4.5. It can be seen that among many twin embryos (Figure 4.3b and 4.5a), only one of them grows into a full twin (Figure 4.5b). However, unlike the small size nanowire, the twin boundaries were not able to sweep across the length due to the interactions of multiple twins (Figure 4.5b). This twin-twin interactions results in the nucleation of a crack as shown Figure 4.5c. In BCC metals, it is known that twin-twin interactions leads to crack nucleation [116, 120]. Following crack nucleation, the propagation of crack along the twin boundary leads to decrease in flow stress and final failure by cleavage mechanism along {112} plane (Figure 4.5d). Generally in BCC metals, the {100} planes are the most likely to cleave, but it has been shown that at low temperatures, the {112} planes also cleave [121].
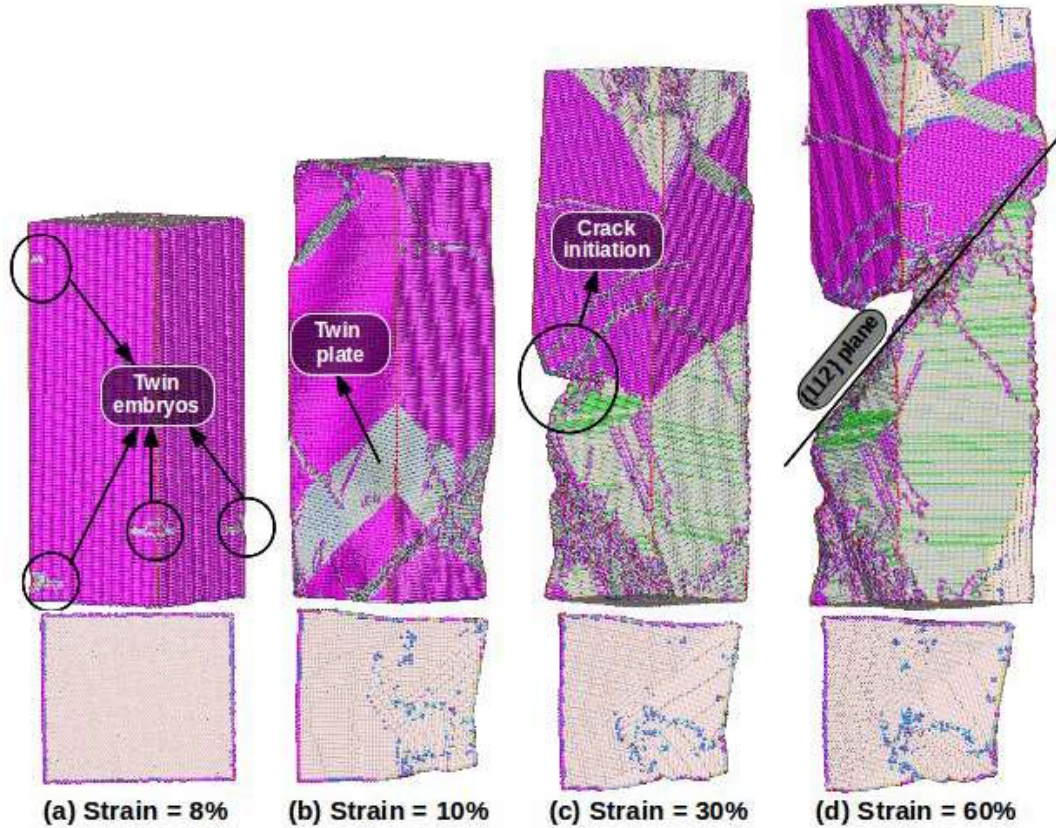
Figure 4.5: Deformation behaviour in large size <100> BCC Fe nanowires with cross section width d = 17.13 nm showing (a) yielding by nucleation of multiple twin embryos (b) growth of twin embryo into full twin plate (c) crack initiation due to twin-twin interactions (d) cleavage failure. The colour is according to the coordination number of atoms: Misty rose - 14 (perfect BCC), blue - 13, green - 10, magenta - 9 (surface), grey - 8, purple - 7 and brown - 6. Except misty rose, all other atoms are defect atoms.

The above MD simulation results shows that the activation of multiple twin sys-
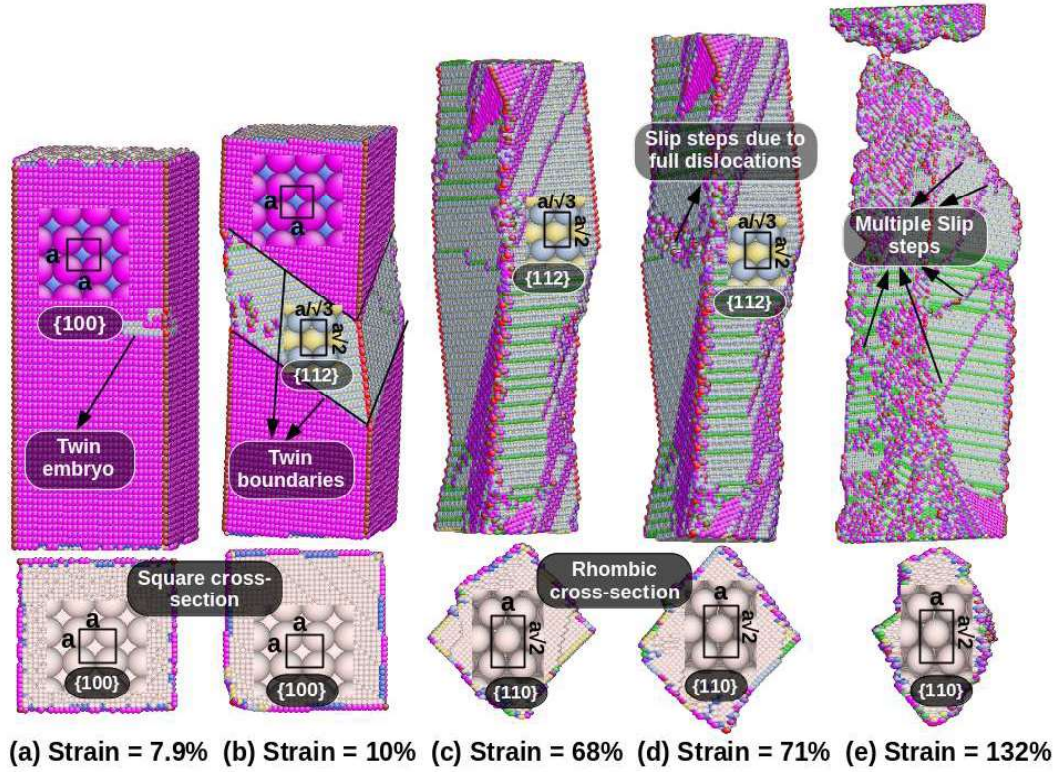
Figure 4.4: Deformation behaviour in small size <100> BCC Fe nanowire with cross section width d = 8.5 nm showing (a) yielding by nucleation of a twin embryo (b) growth of twin embryo into full twin plate (c) reorientation from <100> tensile axis to <110> (d) yielding through full dislocation in reoriented nanowire and (e) failure by necking. The colour is according to the coordination number of atoms: Misty rose - 14 (perfect BCC), blue - 13, green - 10, magenta - 9 (surface), grey - 8, purple - 7 and brown - 6. Except misty rose, all other atoms are defect atoms.

enclosed by two twin boundaries forms in the nanowire. This twin formation results in the reorientation of twinned region, which is reflected as a change in surface coordination (Figure 4.4b). With increasing deformation, the continuous growth of twin makes the twin boundaries to sweep across the nanowire length and transforms the initial <100> nanowire into a completely new configured nanowire with <110> tensile axis (Figure 4.4c). Due to this reorientation, the cross-section of the nanowire changes from square to rhombic shape (Figure 4.4b-c). With further deformation, the reoriented nanowires again undergo an elastic deformation resulting in the occurrence of a second peaks in the stress–strain curves (Figure 4.1a). Following the elastic deformation, the reoriented nanowire yields by emitting a full dislocation (Figure 4.4d) with a corresponding drop in flow stress. Further deformation in the reoriented nanowire till failure occurs by dislocation slip resulting in the formation of slip steps as seen in Figure 4.4d. Finally, the activation of slip in multiple directions leads to neck formation and failure as shown in Figure 4.4e.

84
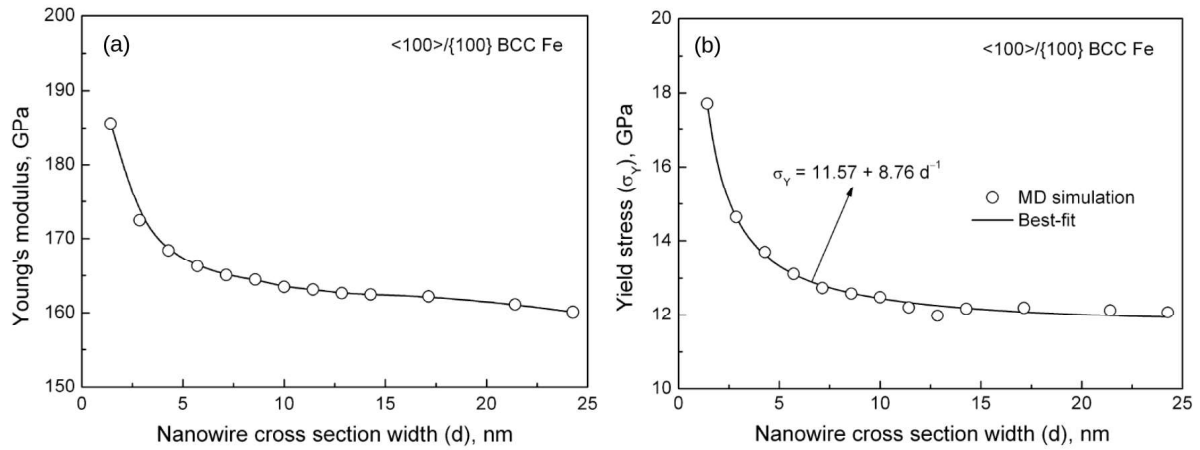
Figure 4.2: Variation of (a) Young's modulus and (b) yield strength as a function of cross section width (d) in <100> BCC Fe nanowire at 10 K.

strain behaviour (Figure 4.1). In a defect free Fe nanowire, the side corners act as the stress concentration sites and facilitate defect nucleation. This single and multiple defect nucleations in small and large size nanowires has resulted in different deformation behaviour as presented in the following;

(a) d = 8.5 nm   (b) d = 17.13 nm
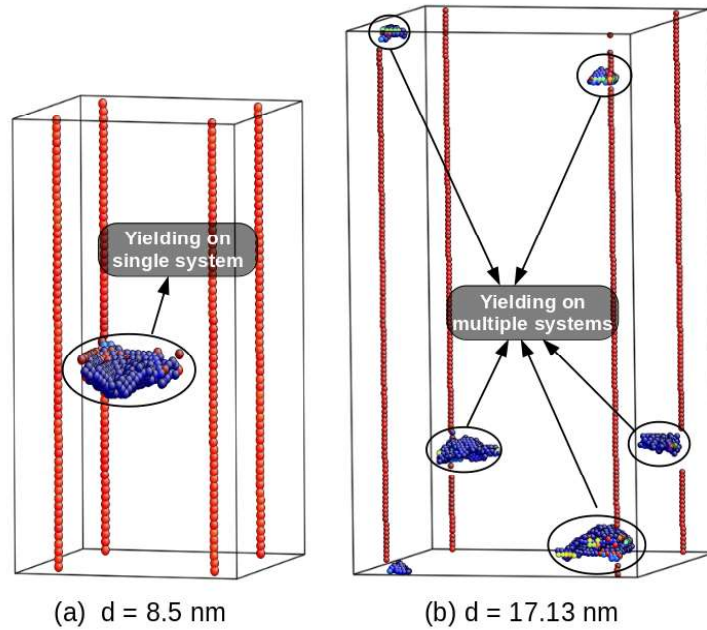
Figure 4.3: Yielding in <100> BCC Fe nanowires by the nucleation of (a) twin embryo on a single twin system in small size nanowire with d = 8.5 nm and (b) multiple twin embryos on different twin systems in large size nanowire with d = 17.13 nm.

Figure 4.4 shows the deformation and failure behaviour of <100> BCC Fe nanowires of size (d) = 8.5 nm, representing the small size nanowires in the range 1.42-11.42 nm. Following nucleation of twin embryo from the nanowire corner (Figures 4.3a and 4.4a), a full twin
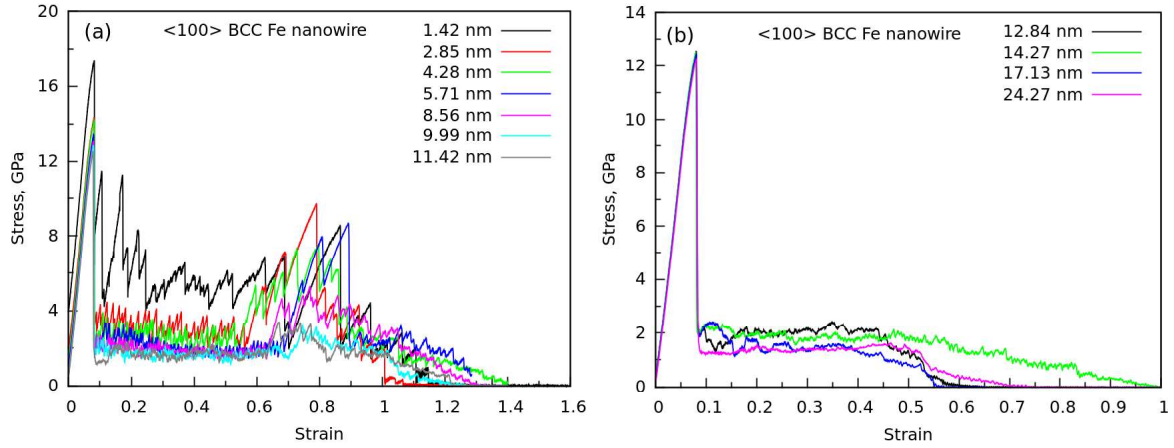
Figure 4.1: Stress-strain behaviour of <100> BCC Fe nanowires of cross-section width (d) in the range (a) 1.42-11.42 nm, and (b) 12.84-24.27 nm at 10 K.

ther, the saturated Young's modulus value of 162 GPa at larger sizes is close to the bulk value of 155 GPa reported for BCC Fe single crystal in <100> direction [16]. This suggests that with increasing size the elastic properties of BCC Fe nanowires approach towards that of bulk BCC Fe. Olsson et al. [117] revealed that the size dependence of Young's modulus arises as a consequence of the deviating elastic properties of surfaces and edges prevalent in small size nanowires. Following elastic deformation, the peak value in the stress-strain curve has been considered as the yield strength of the defect-free BCC Fe nanowire. Figure 4.2b shows the yield stress values as a function of size for <100> BCC Fe nanowires. The yield stress shows a rapid decrease with size up to d = 11.42 nm followed by a gradual decrease towards saturation at large sizes. The saturation value of yield strength is close to the reported theoretical strength of 12.6 GPa for BCC Fe in <100> direction [107, 118]. Similar decrease in yield strength followed by saturation at large size has been observed in gold nanowires by Gall et al. [119]. The decrease in yield strength (σ_Y) in BCC Fe nanowires has been correlated with cross section width (d) as $\sigma_Y = 11.57 + 8.76d^{-1}$ (Figure 4.2b).

4.3.2 Single and multiple twin dominated deformation

The defect nucleation leading to yielding in perfect <100> BCC Fe nanowires of size (d) = 8.5 nm representing the small size nanowires and d = 17.13 nm representing the large size nanowires is shown in Figure 4.3. It can be seen that in small size nanowires, the yielding occurs by the nucleation of single twin embryo (Figure 4.3a), while the nucleation of multiple twin embryos has been observed in large size nanowires (Figure 4.3b). The nucleation of twin embryos from the nanowire corners results in abrupt stress drop as observed in the stress-

4.3 Size effects on twinning - <100> nanowire

In this section, the influence of size on the stress-strain behaviour and deformation mechanisms in <100> BCC Fe nanowire have been presented. The variations in Young's modulus, yield stress and twin propagation stress obtained from stress-strain behaviour are presented as function of size and explained based on the observed deformation mechanisms. The deformation mechanisms such as yielding, number of twin systems and twin growth in different nanowire sizes have been analysed and discussed.

4.3.1 Stress-strain behaviour

The stress-strain behaviour of <100> BCC Fe nanowires of different cross-section width (d) in the range 1.42 to 24.27 nm are shown in Figure 4.1. It can be seen that irrespective of size, all the nanowires undergo an initial elastic deformation up to a peak stress followed by abrupt large drop in flow stress. Following this abrupt drop, the stress-strain behaviour of the nanowires depends strongly on the cross-section width or size. For nanowires in the small size range 1.42-11.42 nm, the flow stress exhibits uniform oscillations about a constant mean value over a wide strain range (Figure 4.1a). A noticeable decrease in the amplitude of flow stress oscillations with increase in nanowire size can also be seen in Figure 4.1a. With further increase in strain, the small size nanowires exhibited the occurrence of second linear elastic peaks followed by large stress drop and then a continuous decrease in the stress up to failure (Figure 4.1a). Contrary to this, the second elastic peaks were absent and only marginal and non-uniform flow stress oscillations occurred for large size nanowires in the range 12.84 - 24.27 nm (Figure 4.1b). Further, the large size nanowires displayed significantly lower strain to failure i.e. ductility compared to small size nanowires (Figures 4.1a and b). The significant difference in stress-strain behaviour suggests that different mechanisms are operative in small and large size <100> BCC Fe nanowires at 10 K.

The linear portion of the stress-strain curve represents the elastic deformation of nanowires and therefore, it has been used to obtain the elastic modulus (Young's modulus) of BCC nanowires as a function of size. The Young's modulus values obtained from the slope of linear stress-strain region are presented in Figure 4.2a as a function of size. A moderate change in slope towards the end region of elastic deformation has been ignored in this calculation. It can be seen that the Young's modulus exhibited a rapid decrease with increase in size for small size range followed by gradual decrease towards saturation at large nanowires (Figure 4.2a). Fur-

4.2   Simulation details

Molecular dynamics (MD) simulations have been carried out in LAMMPS package [94] employing an embedded atom method (EAM) potential for BCC Fe given by Mendelev and co-workers [75]. Mendelev EAM potential predicts a non-degenerate core structure for screw dislocations [81], which is in good agreement with density functional theory (DFT) calculations [82]. The prediction of screw dislocation core is important in order to accurately reproduce the dislocation behaviour in BCC Fe, where screw dislocations dominates the deformation.

The size effects have been studied in <100> and <110> orientations of BCC Fe nanowires. These two orientations have been chosen mainly because, the <100> and <110> nanowires represent the size effects on two different modes of deformation i.e. twinning and dislocation plasticity, respectively (Chapter 3). The <100> nanowire is enclosed by {100} side surfaces, while the <110> nanowire has {111} and {112} as side surfaces. In both the orientations, the cross-section width (d) has been varied from 1.42 to 24.27 nm at a fixed aspect ratio of 2:1 (length : diameter). This corresponds to simulating the number of atoms in the range $600 - 2.4 \times 10^6$. Periodic boundary conditions were chosen along the nanowire length direction, while the other directions were kept free in order to mimic an infinitely long nanowire.

Following the initial construction of the nanowire, energy minimization was performed by conjugate gradient (CG) method. The stable structure thus obtained was thermally equilibrated to a required temperature of 10 K in canonical ensemble (constant NVT). Velocity Verlet algorithm was used to integrate the equation of motion with a time step of 5 fs. Upon completion of the equilibration process, the deformation is carried out at constant strain rate of 1×10^8 s^{-1}. The tensile loading was applied by constantly deforming the box along the nanowire axis as described in Method -1, Section 2.6. During the loading, the atomic system was allowed to deform naturally at a constant strain rate without imposing any stress constraints in the other two directions. The stress was calculated from the Virial expression of stress (Equation 2.27), which is equivalent to a Cauchy's stress in an average sense. AtomEye package [102] was used for the visualisation of atomic snapshots with coordination number, centro-symmetry parameter and common neighbour analysis (Section 2.8).

Chapter 4

Size dependent deformation and failure behaviour of <100> and <110> BCC Fe nanowires

4.1 Introduction

Nanowires inherently possesses high surface area to volume ratio, as a result many properties of nanowires exhibit strong size effects. Size effects on deformation behaviour of FCC nanowires have been documented as a part of literature review in Section 1.3.1, where it has been shown that the size influences the modulus [31], strength [32], nucleation and character of dislocations [33], deformation mechanisms [33], defect interactions and failure behaviour [34, 35]. As the sample diameter decreases below certain size, the stress becomes so high that the deformation twinning takes over as a dominant mode of plastic deformation. However, no systematic study exists pertaining to size effects in BCC Fe nanowires. In view of this, an attempt has been made to understand the influence of size on the deformation behaviour of BCC Fe nanowires. The size effects have been studied in two different orientations, one deforming by twinning i.e. <100> orientation and the other by slip i.e. <110> orientation, thus revealing the influence of size on deformation twinning and dislocation plasticity in BCC Fe nanowires. In both the orientations, the tensile deformation and fracture behaviour as a function of cross section width (d) ranging from 1.42 to 24.27 nm has been examined. The variations in Young's modulus, yield strength and ductility as a function of nanowire size have been presented. The size dependent deformation mechanism and fracture mode have been discussed.

tion twinning dominates at all temperatures. Further, when the nanowire deform by dislocation slip mechanism, the formation of pentagonal atomic chains have been observed in the necking region of the nanowires. In nanowires with d = 0.404 and 0.807 nm, the complete transformation to the pentagonal structures has been observed at higher temperatures. The formation of pentagonal atomic chains have not been observed in nanowires that deform by twinning mechanism. Finally, the twinning to slip transition has been attributed to the coordinated nature of twinning phenomenon, which may get disturbed at small sizes and high temperatures.

tions having the same Burgers vector on adjacent parallel planes. This coordinated or coherent phenomenon of twinning may get disturbed in nanowires of less than a critical size, where the number of surface atoms remains higher than the core atoms. As a result, the twinning is not observed in ultra-thin nanowires. Similarly, increasing the temperature have the same effect as that of decreasing the nanowire size, i.e., the high temperature may also disturb the coordinated behaviour of twinning phenomenon in ultra-thin nanowires. The size dependence of twinning has also been observed in nanocrystalline materials [143]. Below certain grain size, it has been reported that the propensity for deformation twinning decreases with decreasing grain size.

The formation of pentagonal atomic chains in BCC Fe nanowires is one of the interesting observations as it exhibits a five-fold symmetry with respect to the nanowire axis and does not correspond to any of the 14 Bravais lattices. Generally, the pentagonal structure is not observed in 2-dimensional or 3-dimensional structures as it is incompatible with the translational symmetry. However, the strong evidence of pentagonal structures have been found experimentally in 1-dimensional structures such as ultra-thin Cu nanowires [42]. In agreement with experimental observations, many atomistic simulation studies have also shown the formation of pentagonal atomic chains in Cu [41, 144, 145], Al [145], Ni [145, 146], and Au [44, 147]. The pentagonal structures have also been observed in HCP Mg nanowires during the atomistic simulations studies [148, 149]. The initial transformation of the nanowire into non-crystalline structure can be understood in terms of internal atomic rearrangements to maximize the overall atomic coordination leading to an increase in cohesive energy [145]. Following disordered state, the pentagonal unit cell nucleates out of this to minimize the surface energy and grows all along the nanowire leading to long and stable pentagonal nanowire. The observed long pentagonal atomic chains remain stable during the deformation and contribute to large failure strains in small size nanowires.

5.6   Conclusions

Extensive molecular dynamics simulations have been carried out on the tensile deformation behaviour of ultra-thin <100> BCC Fe nanowires of different sizes and temperatures. The simulation results indicated that BCC Fe nanowires with cross-section width less than 3.23 nm deform by twinning mechanisms at low temperatures, while dislocation slip dominated the deformation behaviour at high temperatures. The temperature at which the nanowires show twinning to slip transition, increases with increasing size, and above d = 3.23 nm, deforma-
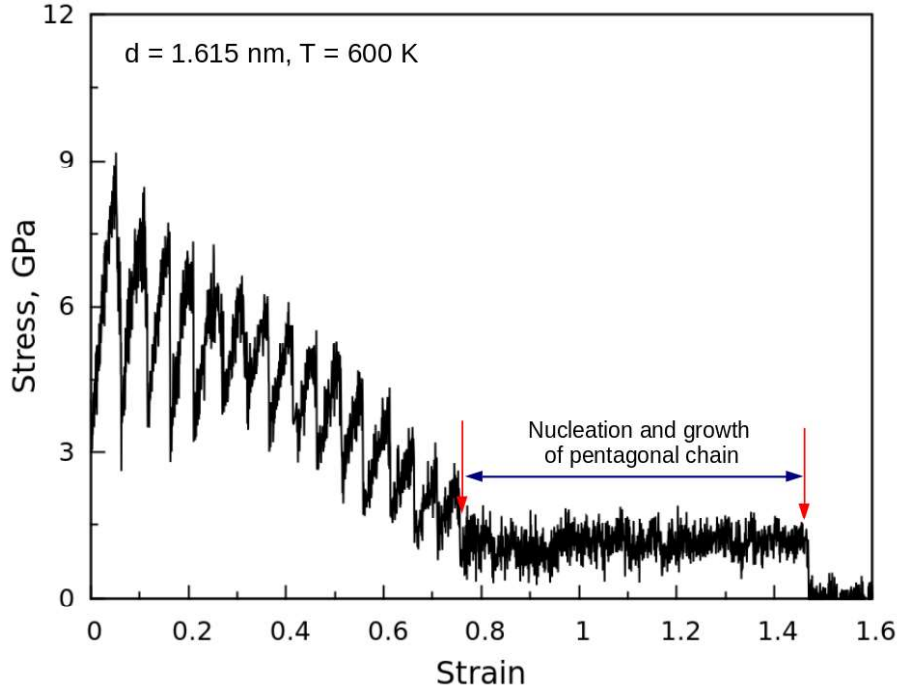
Figure 5.9: Typical stress-strain behaviour of BCC Fe nanowires with d = 1.615 exhibiting the formation of pentagonal chain at 600 K.

axis leads to constant flow stress plateau as observed in the strain range 0.77-1.47 (Figure 5.9). Thus, the formation and growth of pentagonal atomic chains facilitates high ductility in ultra-thin BCC Fe nanowires.

5.5   Discussion

All the previous studies have reported that the <100> BCC nanowires including Fe deform predominantly by twinning mechanism [59–61, 63]. Therefore, the observed twinning to slip transition with respect to temperature and size in ultrathin <100> BCC Fe nanowires is interesting. Similar twinning to slip transition has been reported in Ti micro-crystals [33]. This size dependence of twinning in Ti has been explained based on the simulated slip model. It has been suggested that a pole of screw dislocation perpendicular to the slip plane acts as a promoter for twin nucleation. Below certain critical size, the dislocations are not high enough to activate twinning and as a result, the twinning is not observed in sample size lower than 1 μm [33]. Due to the absence of initial dislocations, the same model cannot be used to explain the observed twinning to slip transition in the present investigation. However, the size dependence of twinning in ultra-thin pristine nanowires may arise due to highly coordinated nature of twinning mechanism. It is well known that the twin grows by the systematic glide of twinning disloca-
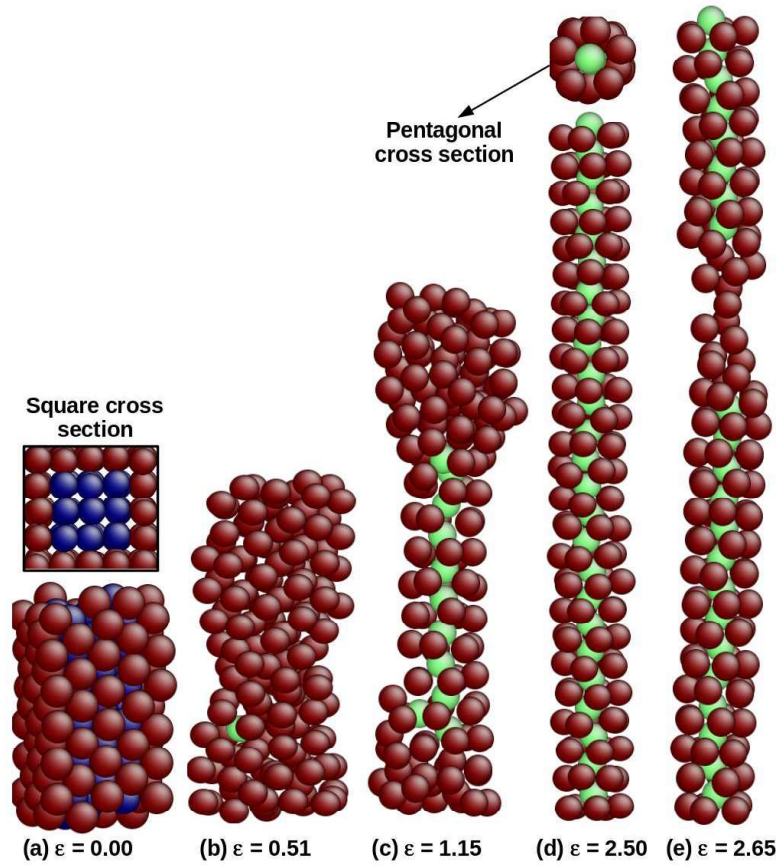
Figure 5.8: The complete transformation of BCC Fe nanowire with d = 0.807 nm into long pentagonal nanowire at 600 K: (a) Initial BCC structure, (b) the disordered structure along with nucleation of pentagonal atomic chain, (c) growth of pentagonal atomic chain (d) completely transformed into pentagonal atomic chains and (e) onset of necking and failure. The atoms are coloured according to CNA. The blue colour indicates the atoms in BCC structure, the red colour indicates the atoms in disordered structure including surfaces and light green colour indicates the atoms in pentagonal or icosahedral symmetry.

pared to 13 rings in large size nanowire with d = 1.615 nm. The combination of size and temperature resulting in complete transformation into pentagonal atomic chains have been marked as red colour filled pentagons in Figure 5.7. It can be seen that the complete transformation has been observed mainly for nanowires with d = 0.404 and 0.807 nm at high temperatures (Figure 5.7).

Typical stress-strain behaviour of BCC Fe nanowires exhibiting the formation of pentagonal chain is shown in Figure 5.9 for the case of nanowire with d = 1.615 nm at 600 K. The large flow stress oscillations in terms of sharp peaks and drops due to the continuous plastic deformation by dislocation slip can be seen up to a strain of 0.77. Each flow stress peak and drop corresponds to dislocation nucleation, propagation and annihilation. Once neck forms in the nanowire, the nucleation of pentagonal atomic structure and its growth along the nanowire

The formation of pentagonal atomic chains as a function of size and temperature is summarized in Figure 5.7. It can be seen that the pentagonal chains were observed only in conditions that are favourable for slip. However, the Figure 5.7 shows that all the nanowires that deform by slip need not exhibit the formation of pentagonal chains. The pentagonal atomic chains were not observed when the nanowire deform by twinning mechanism. Further, significant differences have been observed between the pentagonal chains formed in small and large size nanowires. In large size nanowires, the formation of pentagonal atomic chains remains limited to necking regions as observed for nanowire with d = 1.615 nm in Figure 5.6. For small sizes with d = 0.404 and 0.807 nm and at relatively higher temperatures, the nanowire completely gets transformed to pentagonal atomic chains. This is typically shown in Figure 5.8a-e for the case of nanowire with d = 0.807 nm at 600 K. With increasing strain, the progressive plastic deformation results in complete transformation of the nanowire into non-crystalline state (Figure 5.8b) followed by the nucleation of pentagonal structure out of the non-crystalline atoms (Figures 5.8c). The complete transformation of the nanowire into pentagonal atomic chains and subsequent failure at large strains are shown in Figures 5.8d and e, respectively. Further, the long pentagonal atomic chain consisted of as many as 25 pentagonal rings com-
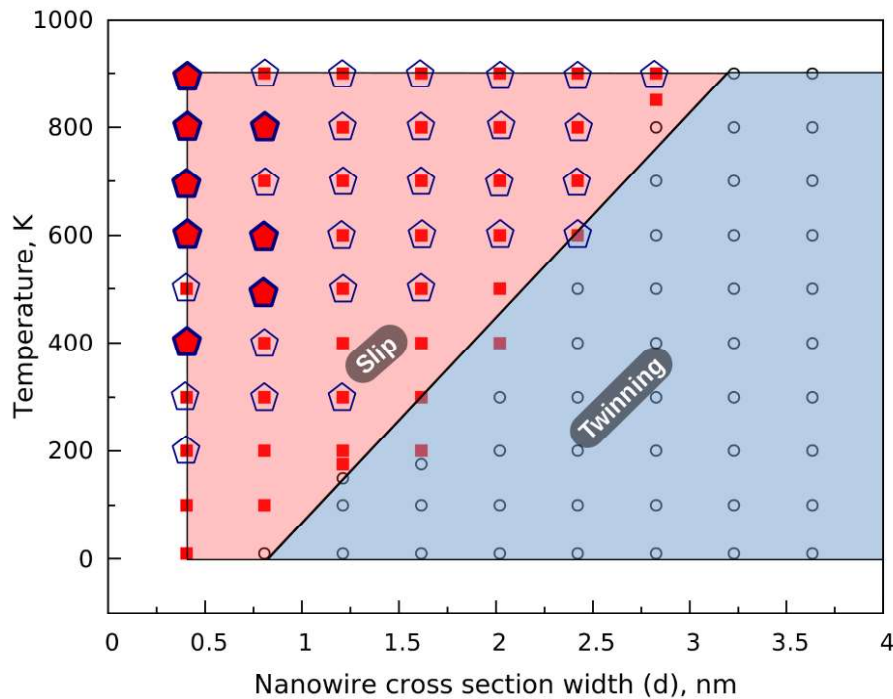
Figure 5.7: The plot highlighting the the combinations of size and temperature in which the pentagonal atomic chains were formed in BCC Fe nanowires. The symbol ⬠ indicates the observation of pentagonal atomic chain and red color filled ⬠ indicates the complete transformation of the nanowire to a pentagonal atomic chain.
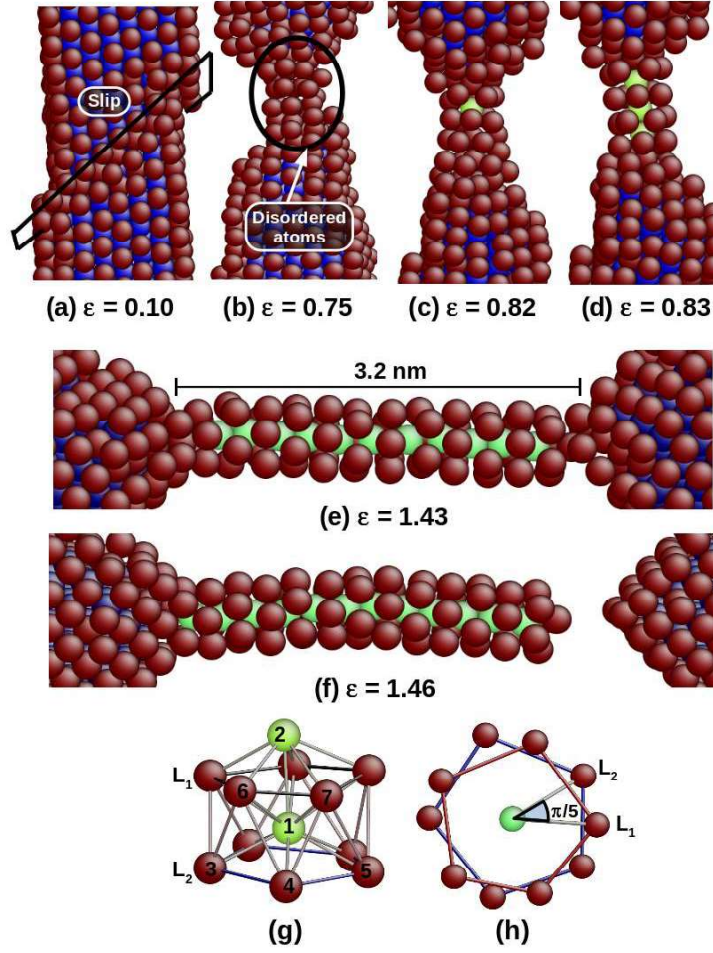
Figure 5.6: The formation of pentagonal atomic chain in the necking region of BCC Fe nanowire with d = 1.615 nm during tensile deformation at 600 K. The atoms are coloured according to CNA. The blue colour indicates the atoms in BCC structure, the red colour indicates the atoms in disordered structure including surfaces and light green colour indicates the atoms in pentagonal or icosahedral symmetry.

Table 5.1: Comparison of inter-atomic distances and the bond angles in the pentagonal unit cell of small (d = 0.807 nm) and large (d = 1.615 nm) size nanowires at 600 K with those reported based on first principles calculations. d_{ij} indicates the distance between the atoms i and j in Figure 5.6g and $\angle ijk$ indicates the bond angle between the i,j,k atoms.

Nanowire	d_{12}	d_{13}	d_{34}	d_{46}	$\angle 314$	$\angle 315$	$\angle 316$	$\angle 317$	$\angle 364$
Small (d = 0.87 nm)	2.40	2.50	2.62	2.72	62.17	110.38	65.52	111.62	57.29
Large size (d = 1.42 nm)	2.37	2.56	2.75	2.74	65.15	116.4	66.16	119.8	58.74
First principles [142]	2.16	2.31	2.39	2.51	62.4	114.2	65.8	117.5	57.00
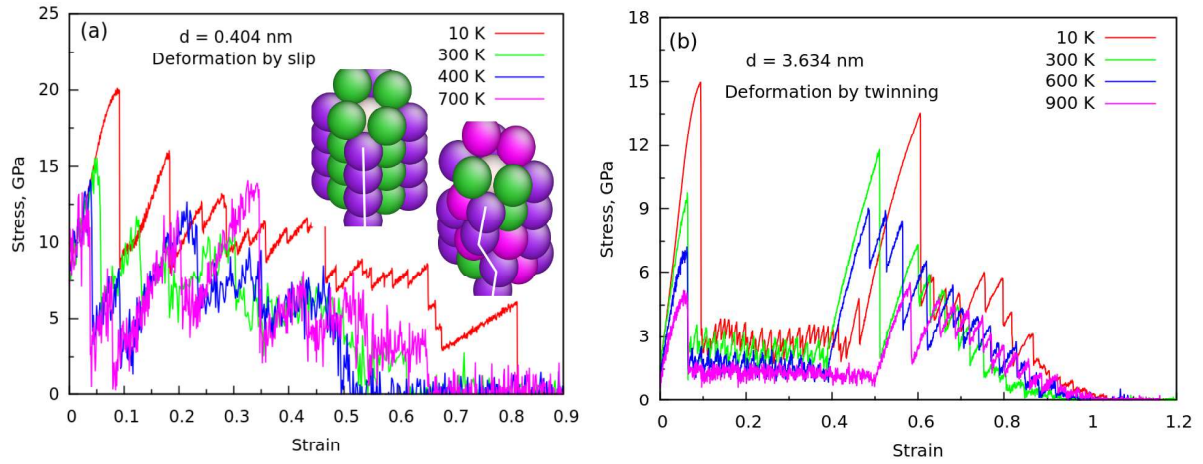
Figure 5.5: The stress-strain behaviour of <100> BCC Fe nanowires with (a) d = 0.404 and (b) d = 3.634 nm at different temperatures ranging from 10-900 K. The inset in (a) shows the relative slip between the two adjacent planes, without any dislocations during the deformation of the smallest size nanowire.

shown in Figure 5.6b. When the cross-section width of the neck region is close to few atomic spacings, some of the disordered atoms rearrange themselves and forms a pentagonal unit cell as shown in Figure 5.6c. Following this formation, the five atom rings are added successively to this structure unit by unit at the expense of disordered atoms in the necking region (Figure 5.6d). This process continue to occur until failure leading to formation of long pentagonal atomic chain at the necking region as shown in Figure 5.6e-f. The maximum length of this pentagonal atomic chain is found to be 3.2 nm and consist of 13 pentagonal rings. The formation of long pentagonal chains indicates their stability at high strains and this contributes to large plastic deformation and high ductility in ultra-thin BCC Fe nanowires. In order to obtain the detailed understanding of structural aspects of pentagonal atomic chain, a single unit cell of the long chain is analysed and presented in Figure 5.6g. It can be seen that the pentagonal chain consist of a central atom having a coordination of 10 atoms enclosed by two pentagonal rings L_1 and L_2. Thus, the long atomic atomic chain has a 1-5-1-5 stacking sequence with successive pentagonal rings L_1 and L_2 rotated by $\pi/5$ (Figure 5.6h). This structure is known as staggered pentagon and has 12 atoms in each unit cell. The stability of staggered pentagonal structure in Fe is confirmed by Sen et al. [142] using first principle calculations. The relevant inter-atomic distances and bond angles in pentagonal unit cell of small (d = 0.807 nm) and large size (d = 1.615 nm) nanowire at 600 K are listed in Table 5.1. It can seen that the values obtained in the present investigation are in close agreement with those calculated by Sen et al. [142] for free pentagonal nanowires.
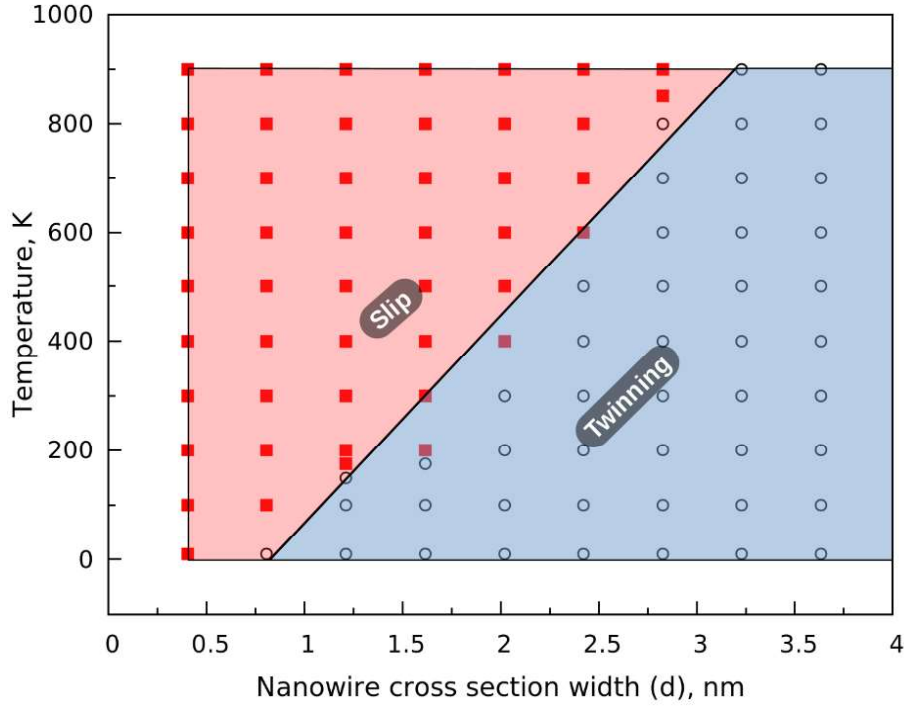
Figure 5.4: The deformation mechanisms map showing the regions dominated by twinning and slip with respect to nanowires size and temperature.

terms of the jerky flow behaviour during plastic deformation (Figure 5.5a). In all other sizes, where slip dominates, 1/2<111> full dislocations have been observed as shown in the bottom row in Figure 5.3. For nanowire size of 3.23 nm and above, twinning to slip transition has not been observed, and deformation by twinning has been noticed irrespective of temperature. This is also reflected in the flow stress plateaus and occurrence of second elastic peak following reorientation in stress-strain behaviour typically shown in Figure 5.5b for d = 3.634 nm in the temperature range 10-900 K . The analysis of atomic configurations for nanowire size with d = 3.634 nm also indicated the dominance of twinning at all temperatures examined.

5.4   Formation of pentagonal atomic chains

In ultra-thin nanowires that deform by dislocation slip mechanism (Figure 5.4) formation of pentagonal atomic chains have been observed at the place of necking. As a representative, Figure 5.6 demonstrates the formation of pentagonal atomic chains during tensile deformation of BCC Fe nanowire with d = 1.615 nm at 600 K. Initially, the nanowire undergoes yielding followed by an extensive plastic deformation dominated by the slip of 1/2<111> full dislocations (Figure 5.6a). With increasing strain, the plastic deformation occurs on multiple slip systems and leads to the formation of necking with disordered or non-crystalline atomic structure as
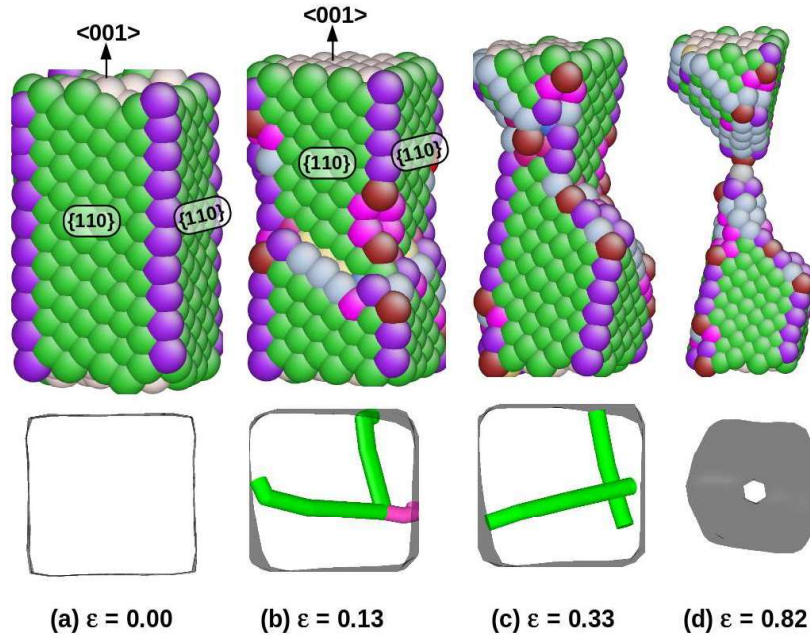
Figure 5.3: The deformation behaviour by dislocation slip under the tensile loading of <100> BCC Fe nanowire with d = 1.615 nm at 300 K. The atoms are coloured according to their coordination number. It can be seen that the surface orientation remains same till failure. The bottom row is the view along the nanowire axis showing the 1/2<111> (green lines) and <100> dislocations (magenta lines).

5.4. The deformation mechanisms map separating the two different regions of twinning and slip modes of deformation with respect to size and temperature are marked in Figure 5.4. It can be clearly seen that the temperature at which the nanowires show twinning to slip transition increases with increase in nanowire size. In other words, at each temperature, there is a critical size below which twinning cannot occur. At low sizes and high temperatures, the slip mode dominates, while at high sizes and low temperatures, deformation twinning is promoted. These results clearly suggest that the BCC Fe nanowires with d < 3.23 nm undergoes twinning to slip transition with increasing temperature. The different modes of deformation are also reflected in respective stress-strain behaviour of the nanowires (Figure 5.1). In case of twinning mode of deformation, a plateau in the flow stress is generally observed, and the occurrence of second elastic peak suggests twinning followed by reorientation [59]. On the other hand, deformation dominated by full dislocation slip results in continuous decrease in flow stress along with jerky flow [59].

In the lowest nanowire size of d = 0.404 nm, even though the deformation by slip is occurred at all temperature, but dislocations have not been observed. Instead of dislocations, the relative slip between the two adjacent slip planes has been observed as shown in the inset of Figure 5.5a. The deformation by slip has also been reflected in the stress-strain curves in
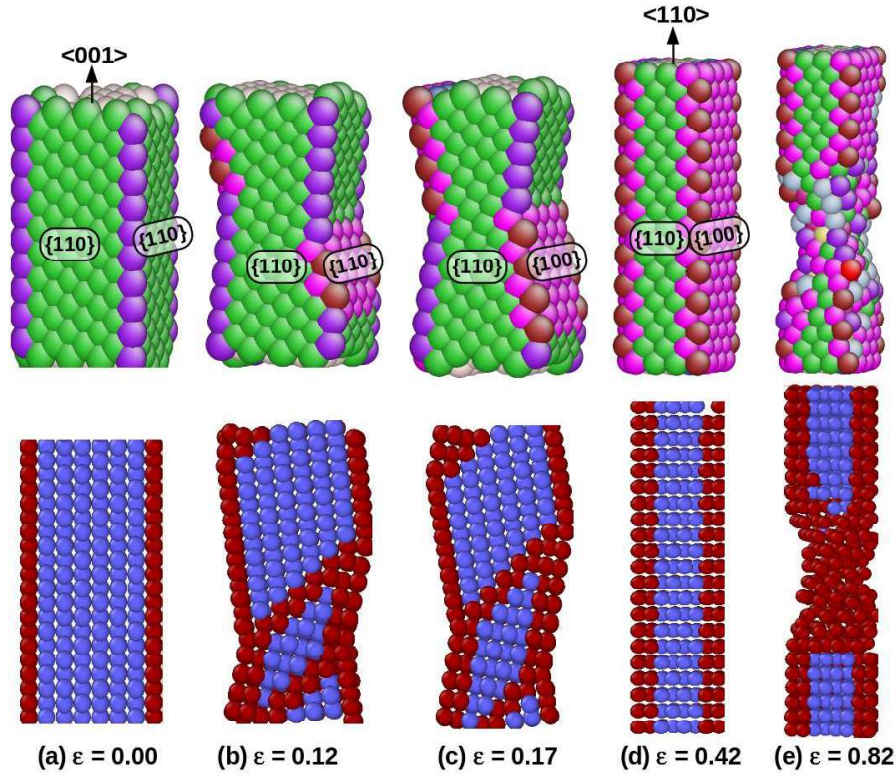
Figure 5.2: The typical deformation behaviour by twinning mechanism under the tensile loading of <100> BCC Fe nanowire with d = 1.615 nm at the lowest temperature of 10 K. The snapshots in the top row are coloured according to the atom's coordination number and indicates the changes in surface orientation due to deformation twinning. In the bottom row, the colour is according to the common neighbour analysis and it clearly shows the presence of twin boundaries.

Contrary to deformation by twinning at low temperatures, deformation dominated by dislocation slip at relatively higher temperatures of 200 K and above is shown for 300 K in Figure 5.3 as an example. The perfect nanowire (Figure 5.3a) yields by nucleation of 1/2<111> full dislocations and with increasing strain, dislocations glide on their respective slip planes and finally annihilate at the opposite surface. As a result of deformation by full dislocation slip, the slip steps have been observed on the surface of the nanowire (Figure 5.3b-c). Absence of surface reorientation clearly indicates that no twinning occurs at 200 K and above. The discrete events of nucleation, glide and annihilation of dislocations is responsible for the observed jerky flow in the stress-strain curve (Figure 5.1b). Following plastic deformation, the nanowire fails by shear along the dominant slip plane at relatively lower values of strain (Figure 5.3d).

In order to demonstrate the combined influence of size and temperature on twinning to slip transition in <100> BCC Fe nanowires, the results obtained for different sizes in the range 0.404 to 3.634 nm and for temperatures ranging from 10 to 900 K are shown in Figure
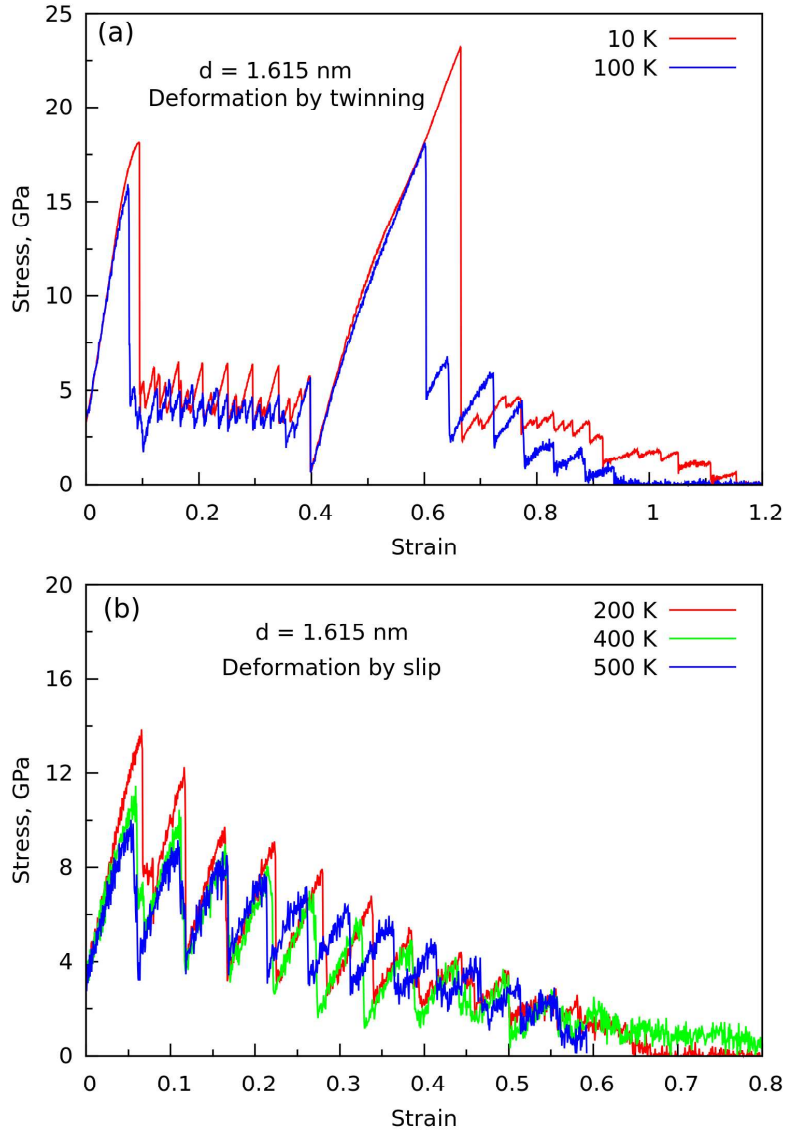
Figure 5.1: The stress-strain behaviour of <100> BCC Fe nanowires with d = 1.615 nm at (a) low (10-100 K) and (b) high (200 - 500 K) temperatures.

but fluctuating flow stress about a mean value in the strain range 0.1-0.4. Once the twin completely sweeps the <100> nanowires, orientation of the nanowire changes to <110> tensile axis having {100} and {110} as side surfaces (Figure 5.2d). It can be clearly seen that the new <110> reoriented nanowire is completely defect free and with increasing deformation, it undergoes an elastic deformation once again as reflected in the occurrence of second elastic peak in the stress-strain curve (Figure 5.1a). Following the second elastic deformation, the reoriented nanowire deforms by full dislocation slip leading to neck formation and final failure (Figure 5.2e) at relatively higher values of strain to failure. For nanowires of size d = 1.615 nm, similar stress-strain behaviour and deformation dominated by twinning mechanism have been observed up to 150 K.

performed at a constant strain rate of 1×10^8 s^{-1} along the axis of the nanowire. At each size and temperature conditions, five independent MD simulations with different random number seeds have been performed to make statistically meaningful conclusions. The average stress was calculated from the Virial expression (Section 2.7). The visualization of atomic configurations was performed using AtomEye [102] and OVITO [103] packages with coordination number and common neighbour analysis (CNA). The CNA method has been used to distinguish the atoms in crystalline, non-crystalline and pentagonal or icosahedral environment.

5.3   Twinning to slip transition

Figure 5.1 shows stress-strain behaviour of <100> BCC Fe nanowires with d = 1.615 nm at different temperatures ranging from 10 to 500 K. It can be seen that at all temperatures, the nanowires undergo an initial elastic deformation up to a peak stress followed by an abrupt drop in flow stress due to yielding. Following yielding, the stress-strain behaviour of the nanowires depends strongly on the temperature. At low temperatures of 10 and 100 K, the stress-strain behaviour during plastic deformation exhibits uniform flow stress oscillations about a constant mean value up to a strain of 0.4 (Figure 5.1a). Following this, the nanowires display second elastic peak followed by stress drop and continuous decrease in stress till failure. On the other-hand, at high temperatures i.e. at 200 K and above, the nanowires don't show any second elastic peak (Figure 5.1b). During plastic deformation, a continuous decrease in stress with large fluctuations (jerky flow) till failure has been observed (Figure 5.1b). The observed significant difference in the stress-strain behaviour clearly suggests that different deformation mechanisms are operative at low (i.e. 10 and 100 K) and high (i.e., at 200 K and above) temperatures during tensile deformation in <100> BCC Fe nanowires.

In order to understand the difference in stress-strain behaviour, the atomic configurations have been analysed as a function of strain at various temperatures. Figure 5.2 shows the deformation behaviour of <100> BCC Fe nanowire with d = 1.615 nm at the lowest temperature of 10 K. It has been observed that the initially perfect nanowire (Figure 5.2a) yields by the nucleation of a twin embryo, which is associated with an abrupt drop in flow stress. Following this, the twin embryo becomes a full twin enclosed by two twin boundaries (Figure 5.2b). With increasing strain, the twin grows along the axis of the nanowire (Figure 5.2c) and progressively reorients the nanowire within the twinned region. The growth of twins by repeated nucleation and glide of 1/6<111> twinning partials on the twin boundaries is responsible for the constant

(quanta of conductance), where e is the electron charge and h is the Planck's constant [138]. The linear atomic chains have been observed experimentally during the stretching of Au and Cu nanowires [138–140] and display conductance close to G_0. Similarly, Gonzalez et al. [42] observed the formation of pentagonal chains during the stretching of Cu nanowires which exhibited the conductance of $4.5G_0$. During tensile deformation, the ultra-thin Au nanowires have been found to exhibit a zigzag shape, which remains stable even if the load is relieved [141]. It has been postulated that the competition between optimal internal packing and minimal surface energy is the main driving force behind these morphological structures at ultra-thin sizes [43]. However, the deformation mechanisms and the associated morphological changes in ultra-thin BCC nanowires have not been explored. For the first time, we report the formation of long pentagonal atomic chains during the tensile deformation of ultra thin BCC Fe nanowires using molecular dynamics simulations. Extensive MD simulations have been performed on <100> BCC Fe nanowires with different cross section width varying from 0.404 to 3.634 nm at temperatures ranging from 10 to 900 K. The range of nanowire size and temperatures over which the pentagonal atomic chains have formed have been described.

5.2 Simulation details

Molecular dynamics (MD) simulations have been performed using LAMMPS package [94] employing an embedded atom method (EAM) potential for BCC Fe given by Mendelev and co-workers [75]. BCC Fe nanowires oriented in <100> axial direction with {110} as side surfaces were considered in this study. MD simulations have been performed on nanowires with cross-section width (d) ranging from 0.404 to 3.634 nm. For each nanowire cross section width, the simulations have been performed at different temperatures ranging from 10 to 900 K. In all nanowires, the length (l) was twice the cross- section width (d). Periodic boundary conditions were chosen along the nanowire length direction, while the other directions were kept free in order to mimic an infinitely long nanowire. After the initial construction of nanowire, energy minimization was performed by conjugate gradient method to obtain a stable structure. To put the sample at the required temperature, all the atoms have been assigned initial velocities according to the Gaussian distribution. Following this, the nanowire system was thermally equilibrated to a required temperature for 125 ps in canonical ensemble using Nose-Hoover thermostat. The velocity verlet algorithm was used to integrate the equations of motion with a time step of 5 femto seconds. Following thermal equilibration, the tensile deformation was

Chapter 5

Twinning to slip transition and formation of pentagonal atomic chains in ultra-thin <100> BCC Fe nanowires

5.1 Introduction

In bulk metals, the conventional understanding is that twinning occurs only at low temperatures, while the plastic deformation is dominated by the slip of dislocations at high temperatures. Molecular dynamics simulations studies [60–62] including the present work (Chapters 3 and 4) have shown that the <100> BCC Fe nanowires deforms by twinning mechanism at 10 K. However, the temperature dependence of this twinning behaviour has not been investigated in Fe or any other BCC nanowires. Further, previous studies on FCC nanowires have shown that with decreasing size there exist a clear transition from full dislocation slip to twinning/partial dislocations [33,36,37] (Section 1.3.1). Contrary to this, Yu et al. [137] demonstrated a reverse transition from twinning at higher sizes to full dislocation slip at smaller sizes in HCP Ti. Using in-situ experiments, deformation twinning has been observed in HCP Ti single crystal of size 1 μm and above. Below this size, twinning is entirely replaced by the slip of dislocations [137]. These observations strongly suggest that there is a size limit below which twinning does not occur in HCP Ti. In this context, it is important to understand how the size and temperature influences the twinning behaviour in BCC nanowires.

It has been shown that the deformation mechanisms in nanowires of cross-section width in the order of few atomic spacing is different from thick nanowires. The formation of linear, pentagonal, single shell, multi-shell and other weird atomic chains have been observed during the deformation of ultra-thin FCC nanowires [41–45]. Further, the formation of all these atomic chains has been associated with conductance in multiples of $G_0 = 2e^2/h$

$<111>$ BCC Fe nanowires undergo ductile-brittle transition at 400 K. Below this temperature, the nanowires yield through the nucleation of a sharp crack and fails in a brittle manner, whereas at high temperatures, the nucleation of multiple $1/2<111>$ dislocations associated with significant plastic deformation leads to ductile failure. At the transition temperature of 400 K, the nanowire yields through the nucleation of crack, but fails in ductile manner due to dislocation nucleations from crack tip. Further, it has been observed that the transition temperature increases with increasing the nanowire size and strain rate.

The ductile-brittle transition in $<111>$ BCC Fe nanowires results from the relative variations of yield and fracture stresses as well as slip behaviour with respect to temperature. Above the transition temperature of 400 K, the lower values of yield stress compared to fracture stress facilitates yielding by the nucleation of dislocations and significant plastic deformation before ductile failure. This is well supported by the occurrence of wavy glide and dislocation multiplications at high temperatures. Below the transition temperature, the lower values of fracture stress than the yield stress leads to yielding by crack nucleation and brittle failure with negligible dislocation activity in the nanowires. Further, at high temperatures, it has been observed that the nanowire surfaces aid in dislocation multiplication mechanism and also in dissociation of immobile dislocations.

nm, it has been observed at 450 K (Figure 6.10b). Similarly, the simulations performed with the circular cross-section nanowire of 8.5 nm diameter yields a transition temperature of 550 K (Figure 6.10c), which is higher than that observed for the square cross-section nanowire. These results also indicate that the circular cross-section nanowires attains higher yield strength values, and as a result, the yield stress versus temperature curve in Figure 6.9 crosses the fracture stress versus temperature curve at relatively higher temperature compared to the square cross-section nanowire. However, it must be noted that the qualitative behaviour of the stress-strain curve, defect nucleation and deformation mechanisms in circular cross-section nanowires is same as that of the square cross-section nanowires.
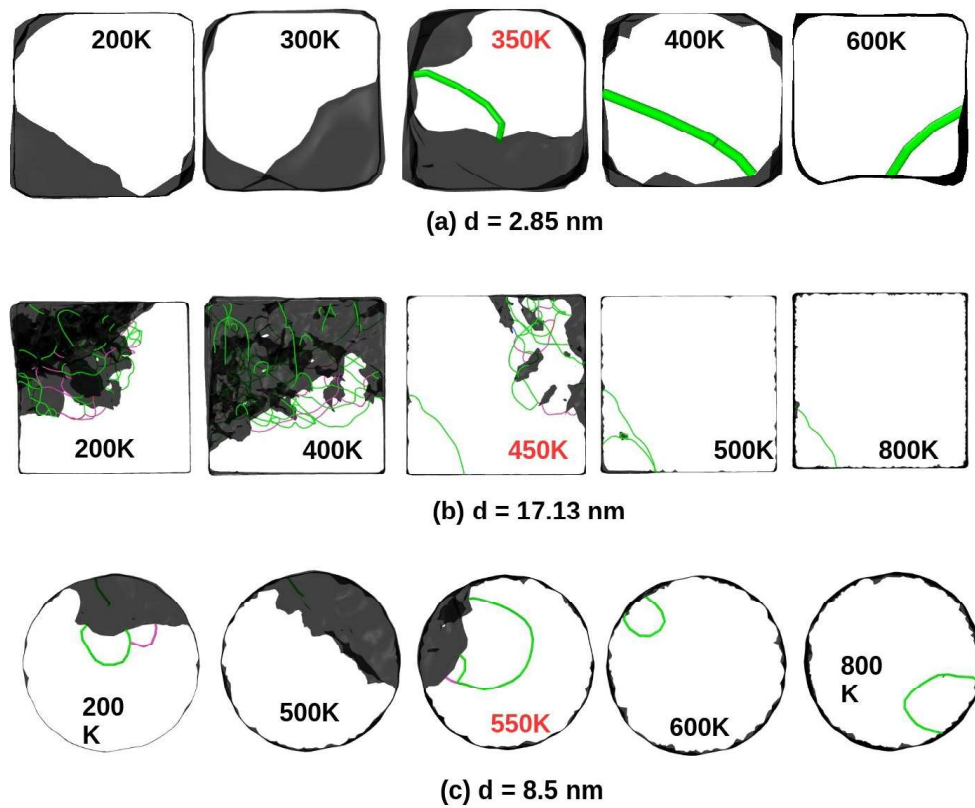
Figure 6.10: Defect nucleation in square cross-section nanowires of (a) low and (b) high size with respect to temperature. Defect nucleation in circular cross-section nanowire of d = 8.5 nm with respect to temperature is shown in (c). The transition temperature in each case has been highlighted in red colour. The colour code details are described in Figure 6.3 caption.

6.8   Conclusions

Temperature dependent deformation and failure behaviour of $<111>$ BCC Fe nanowires has been investigated by molecular dynamics simulations. The simulation results indicate that
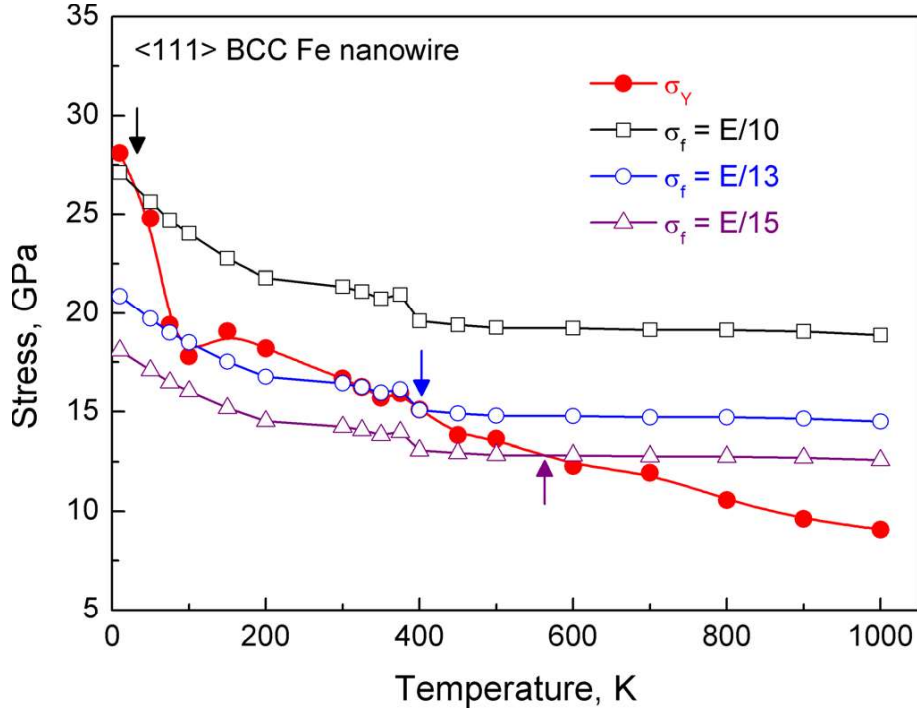
Figure 6.9: Variations of yield stress as a function of temperature along with fracture stresses (σ_f) approximated to E/10, E/13, and E/15.

independent slip systems (Figure 6.4). On the other hand, when the nanowires show ductile behaviour, the wavy glide is extensively observed as depicted in Figures 6.5 and 6.7. In the case of wavy glide, the requirement of five independent slip systems is naturally met and this induces significant plastic deformation leading to ductile fracture.

Finally, it is interesting to note that the ductile-brittle transition observed in the <111> BCC Fe nanowire is absent in <100> and <110> nanowires (Chapter 3 and 4). The <100> and <110> BCC Fe nanowires undergo significant plastic deformation and fails via ductile mode even at the lowest temperature of 10 K. The activation of multiple slip systems satisfying the von-Mises criterion even at 10 K in <110> BCC Fe nanowires lead to gross plastic deformation and high ductility. In <100> BCC Fe nanowire, different deformation mechanisms of twinning and reorientation at 10 K results in high ductility. Apart from orientation, the nanowire size and shape also play an important role on the deformation mechanisms. In order to reveal the influence of size on the observed ductile-brittle transition, further MD simulations have been carried out on two different nanowire sizes of 2.85 and 17.13 nm representing lower and higher sizes, respectively. The results indicate that the ductile-brittle transition temperature increases with increasing nanowire size. For the nanowire of cross-section width (d) = 2.85 nm, the transition has been observed at 350 K (Figure 6.10a), whereas for nanowires with d = 17.13

also been carried out at a strain rate of 1×10^9 s^{-1}. A transition temperature of 450 K observed for 1×10^9 s^{-1} clearly indicates that the ductile-brittle transition temperature (DBTT) increases with increasing strain rate in the Fe nanowire. The higher transition temperatures than the bulk counterparts observed in the present investigation can be ascribed as a consequence of high strain rates used in MD simulations.

The ductile to brittle transition behaviour can be explained based on the relative variations of yield and fracture stresses with respect to temperature. It is known that Young's modulus (E) is related to the perfect or fracture strength σ_f of a material through the relation $\sigma_f = (E\gamma_s/a_0)^{1/2}$, where γ_s is surface energy of the fractured surfaces and a_0 is inter-atomic spacing [13, 16]. By making a reasonable approximation of $\gamma_s = Ea_0/20$, a rough estimate of strength in terms of Young's modulus shows that σ_f varies between E/4 and E/15 depending on material and test conditions [13, 16]. The variations of yield strength and σ_f (obtained by E/10, E/13, and E/15) as a function of temperature are shown in Figure 6.9. It can be clearly seen that σ_f is less sensitive to temperature compared to yield stress and as a result, all the three σ_f curves cross over yield strength at different temperatures. The temperatures of cross-over for E/10, E/13, and E/15 have been obtained as 40 K, 400 K, and 570 K, respectively (Figure 6.9). The temperature at which the fracture stress crosses the yield strength is considered as brittle-ductile transition temperature. Below the transition temperature, the fracture stress is either lower or close to yield stress and this leads to fracture before yielding. Above the transition temperature, fracture stress is much higher than the yield stress and this result in yielding, significant plastic deformation, and ductile failure. From the above comparison, it is clear that σ_f values evaluated as E/13 crosses the yield strength at 400 K as observed in the MD simulations (Figure 6.9). Therefore, σ_f = E/13 can be assumed to represent the ductile to brittle transition behaviour of <111> BCC Fe nanowire.

In a single phase BCC Fe-Co alloy, Johnston et al. [165] have shown that the change in fracture behaviour is primarily associated with a change in slip behaviour and the yield stress plays a secondary role. In the BCC Fe-Co alloy, it has been shown that when the deformation is restricted to a planar glide, the alloy failed in brittle manner, whereas the wavy glide induces the ductile behaviour [165]. This correlation has been ascribed to the requirement of at least five independent slip systems to induce a small and homogeneous strain, that is, von-Mises criterion. In the present study, it has been observed that when the nanowires failed in brittle manner, a few dislocations present at the crack tip have been associated with only one or two

nanowires and bulk single crystals [65]. In nanowires, yielding results from the nucleation of defects, whereas movement of existing dislocations leads to yielding in the bulk single crystals. The presence of a hump or concave down region in the yield stress-temperature curve at about 100 K (Figure 6.2b) is in agreement with the experimental observations reported for the pure bulk single crystal of BCC Fe [158–161]. However, the occurrence of hump in the bulk single crystal has been observed in the temperature range 200-250 K. Further, it has been shown that this hump disappears in Fe specimens doped with a small amount of carbon atoms [158, 159]. These studies indicate that the hump is intrinsic to pure BCC Fe lattice. Guyot and Dorn [162] have suggested that this hump in flow stress is due to the double hump shape of Peierls potential in BCC lattice. Interestingly, the Mendelev EAM potential also shows the double hump Peierls potential for BCC Fe [163]. Therefore, the hump in yield stress versus temperature curve observed in the present investigation can be attributed to the double hump shape of the Peierls potential.

6.7.2 Ductile-brittle transition

Influence of temperature on tensile deformation of<111> BCC Fe nanowire clearly indicated that the nanowires yield through the nucleation of a sharp cracks and fail in brittle manner at low temperatures (10-375 K), whereas nucleation of multiple dislocations at yielding followed by significant plastic deformation leads to ductile failure at high temperatures (450-1000 K). At 400 K, the nanowire yielded by crack nucleation and reasonable dislocation activity at the crack tip resulted in ductile failure. The above failure behaviour with respect to temperature is also reflected in the tensile ductility. BCC Fe nanowires displayed negligible plastic strain at low temperatures (10-375 K) followed by a rapid increase in the accumulated plastic strain in the temperature range 375-500 K and high but nearly constant plastic strain above 500 K. These observations clearly suggest that BCC Fe nanowires display ductile-brittle transition at 400 K. Similar ductile-brittle transition has been observed in bulk single crystal BCC Fe [150]. However, the transition temperature of 400 K observed in nanowires is significantly higher than 130 K reported for the strain rate 4.46×10^{-5} s^{-1} in bulk single crystal BCC Fe [150]. An increase in transition temperature to 154 K with the increase in strain rate to 4.46×10^{-3} s^{-1} has also been reported [150]. Based on the detailed investigation, the ductile to brittle transition in BCC Fe has been successfully modeled as a function of strain rate [164]. A transition temperature of 320 K has been predicted for the strain rate 1×10^3 s^{-1} in BCC Fe [164]. In order to examine the strain rate dependence of ductile-brittle transition in Fe nanowires, MD simulations have
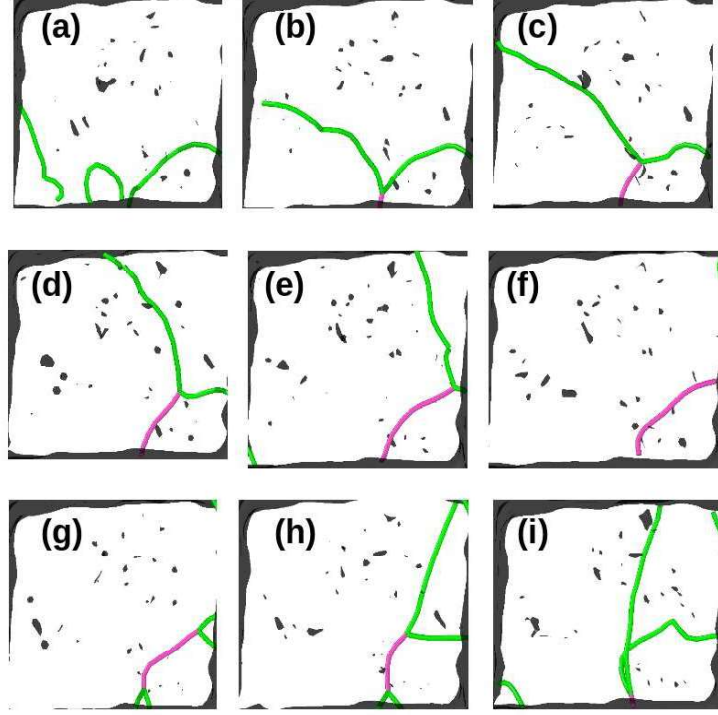
Figure 6.8: Surface assisted formation and dissociation of <100> immobile dislocations through two 1/2<111> mobile dislocations at high temperatures. The green lines indicate the dislocations with the Burgers vector 1/2<111> and the magenta lines represent the dislocations with the Burgers vector <100>.

the dissociation of immobile dislocations in BCC nanowires.

6.7 Discussion

6.7.1 Temperature dependence of yield stress

In BCC/FCC metallic nanowires, the variations in yield stress (σ_Y) with temperature (T) follow either $\sigma_Y = A - BT$ or $\sigma_Y = A - B\sqrt{T}$ relation depending upon the inter-atomic potential used in MD simulations [10, 157]. In BCC Fe nanowires, it has been shown that the yield stress follows $\sigma_Y = A - B\sqrt{T}$ relation with Mendelev EAM potential [65]. In agreement with above observation, the observed decrease in yield stress with the increase in temperature in the present study followed the relation $\sigma_Y = 26.8 - 0.58\sqrt{T}$. It can be seen that the observed temperature dependence of yield stress in BCC Fe nanowires (Figure 6.2b) is different from their bulk single crystal counterparts. In bulk single crystals, the yield stress generally saturates above a critical temperature [158–161]. In BCC Fe nanowires, saturation in yield stress has not been observed. This difference in behaviour essentially arises from the difference in yielding events in BCC Fe

dislocations (Section 1.3.2). Using dislocation dynamics simulations, it has been shown that the surface controlled dislocation multiplication occurs only when the screw dislocation mobility is much lower than that of edge dislocation. When the mobility of edge and screw dislocations is equal, the complete dislocation gets annihilated at the surface and the dislocation multiplication does not occur [53].

6.6   Dissociation of immobile dislocation

It has been observed that the deformation behaviour of <111> BCC Fe nanowires is dominated by the slip of 1/2<111> mobile dislocations at high temperatures (450-1000 K). In addition to 1/2<111> dislocations, <100> immobile dislocations have also been observed. The different stages of the formation and dissociation of <100> immobile dislocation emanating from the interactions of two 1/2<111> mobile dislocations are shown in Figure 6.8. Initially, two 1/2<111> dislocations nucleate from the nanowire surface and attract towards each other (Figure 6.8a). With increasing strain, part of these two dislocations combine and form a <100> immobile dislocation (Figure 6.8b). Subsequent glide of these mobile dislocations at Y-junction leads to a zipping process, which increases the length of the immobile dislocation (Figures 6.8c and 6.8d). Following completion of zipping process, long <100> immobile dislocation is obtained (Figures 6.8e and 6.8f). The formation of <100> dislocation has also been observed during the compressive deformation of <100> BCC Fe nanopillars [56]. Generally, it is assumed that <100> dislocation is highly stable and immobile and aids in the nucleation of micro-cracks in BCC metals [16]. Contrary to this, it has been observed in the present study that <100> dislocation is not stable during the deformation of nanowires and dissociates into two mobile dislocations with Burgers vector 1/2<111> as shown in Figures 6.8g- 6.8i. The dissociation/unzipping process of <100> dislocations initiates from the surface of the nanowire through the formation of two Y-junctions (Figure 6.8g) and with increasing deformation, one of the Y-junction penetrates towards the other end of the dislocation (Figures 6.8h and 6.8i). According to Frank's criterion, the dissociation of <100> dislocation is difficult to be observed as this reaction leads to the increase in energy (i.e., $b_1^2 < b_2^2 + b_3^2$, where b_1 is the Burgers vector of immobile dislocation and b_2 and b_3 are the Burgers vector of dissociated dislocations). However, this dislocation reaction becomes feasible at high energy or stresses in the order of GPa as observed in the present study. Since the nanowire surfaces can act as local stress raisers, it is reasonable to conclude that the surfaces of the nanowires/nanopillars provide a source for

It can be seen that when a mixed dislocation nucleates from the nanowire corner (Figure 6.7a), it align itself to a straight screw configuration with further glide (Figure 6.7b). This straight screw dislocation glides through the kink-pair mechanism, where the kinks nucleate from the nanowire surfaces. When the kinks having different orientations nucleated from two different surfaces move towards each other, a cusp develops at their intersection point on the straight screw dislocation (Figure 6.7b and 6.7c). With increasing deformation, the radius of curvature of the cusp decreases (as observed from the nanowire axial direction, i.e., top view) and it appears like a dislocation loop as shown in Figure 6.7c. As the loop grows with strain, the edge component of the loop reaches the nearby nanowire surface and this creates three independent screw dislocations in the nanowire (Figures 6.7d and 6.7e).
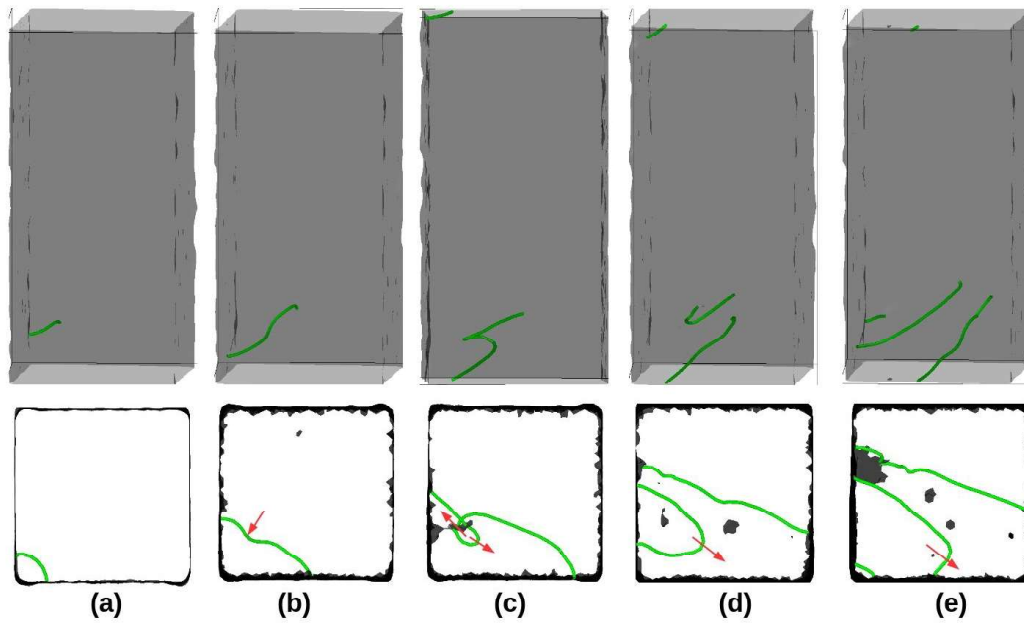
Figure 6.7: A special dislocation multiplication mechanism observed in <111> Fe nanowires at high temperatures in the range 450-1000 K. The green lines indicate dislocations with Burgers vector 1/2<111>. The black regions indicate nanowire surfaces. The arrow marks indicate the direction of dislocation motion.

The mechanism of kink nucleation and glide from the nanowire surface resulting in dislocation multiplication into three independent dislocations has been shown in Mo nanopillars by Weinberger and Cai [52] using a combination of MD and dislocation dynamics simulations (Section 1.3.2, Figure 1.20). It has been suggested that a similar dislocation multiplication will be operating in other BCC nanowires [10] as observed in the present study. This observation further supports the applicability of Mendelev EAM potential for understanding deformation behaviour in BCC Fe nanowires. For the operation of this special dislocation multiplication mechanism, Lee et al. [53] laid down necessary conditions on the mobility of edge and screw

corners glide with the increase in plastic deformation on their respective glide planes (mainly {110} type) and eventually escape to the surface (Figures 6.5b and 6.5c). The continuous nucleation and glide of dislocations on interacting glide planes leads to the formation of well defined necking (Figure 6.5d) and the nanowires fail in ductile manner at significantly higher plastic strains. Interestingly at high temperatures of 900 and 1000 K, it has been observed that the disordered atoms in the neck region rearrange themselves and forms the pentagonal atomic chain as shown in Figure 6.6. The atomic chain consists of a central atom sandwiched between the two pentagonal rings, where each pentagonal ring consists of 5 atoms (Figure 6.6). The formation of pentagonal atomic chains in <111> BCC Fe of cross-section width (d) as large as 8.5 nm is interesting, because, in <100> BCC Fe nanowires the pentagonal atomic chains have been observed only at very small sizes below 3.23 nm (Chapter 5). The transformation of perfect BCC lattice into the pentagonal structure has been described in terms of energy minimization [43] as discussed in Chapter 5.

(a) **(b)**
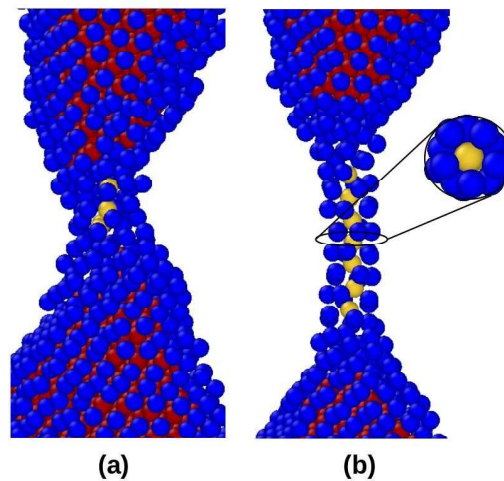
Figure 6.6: Formation of pentagonal atomic chain in the necking region during deformation of <111> Fe nanowires with d = 8.5 nm at 900 K. The red colour represents perfect BCC atoms, blue colour indicates the atoms in the non-crystalline structure, and yellow indicates the atoms in five fold symmetry.

6.5   Dislocation multiplication at high temperatures

In bulk materials, the dislocations generally multiply by the well known Frank-Read mechanism. However, the Frank-read mechanism no longer operates when the size is reduced to nanoscale. A special dislocation multiplication mechanism operating during plastic deformation of <111> BCC Fe nanowires at high temperatures (450-1000 K) is shown in Figure 6.7.
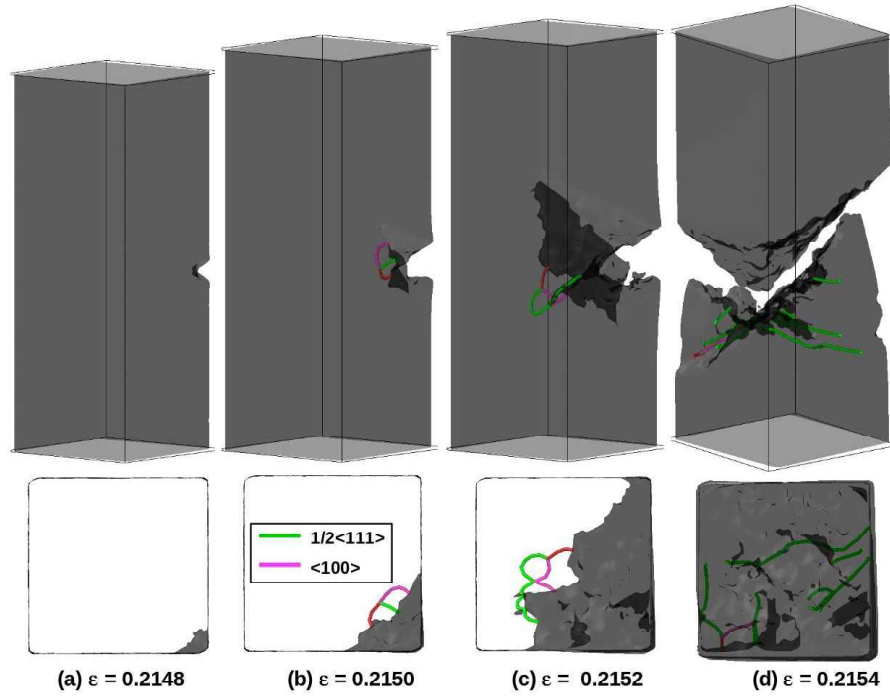
Figure 6.4: Atomic snapshots as a function of total strain at 50 K representing deformation behavior of <111> Fe nanowires at low temperatures in the range 10-375 K. The colour code details are described in Figure 6.3 caption.
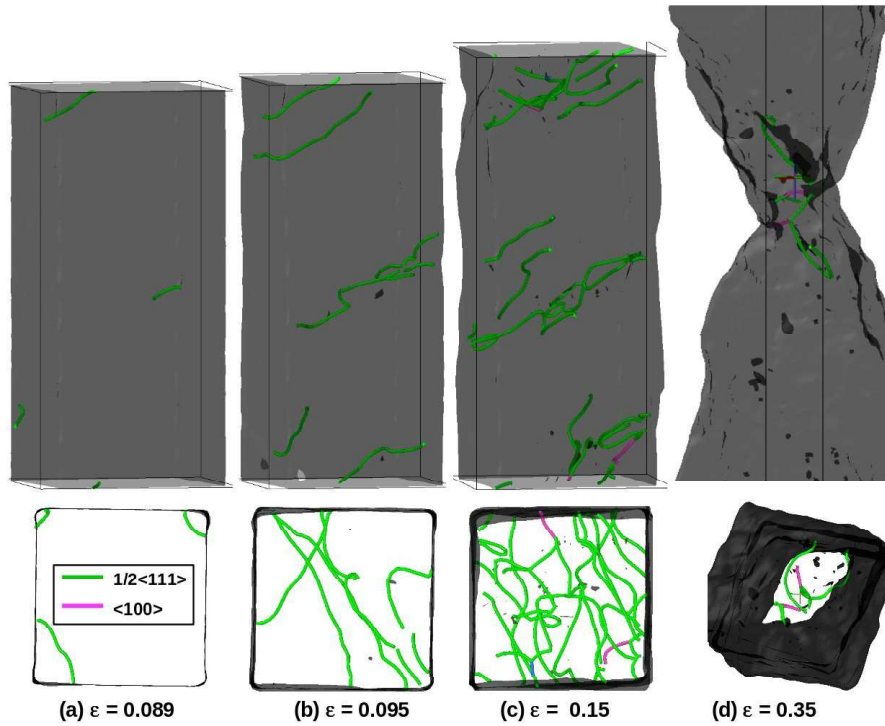
Figure 6.5: Atomic snapshots as a function of total strain at 700 K representing deformation behaviour of <111> Fe nanowires at high temperatures in the range 450-1000 K. The colour code details are described in Figure 6.3 caption.
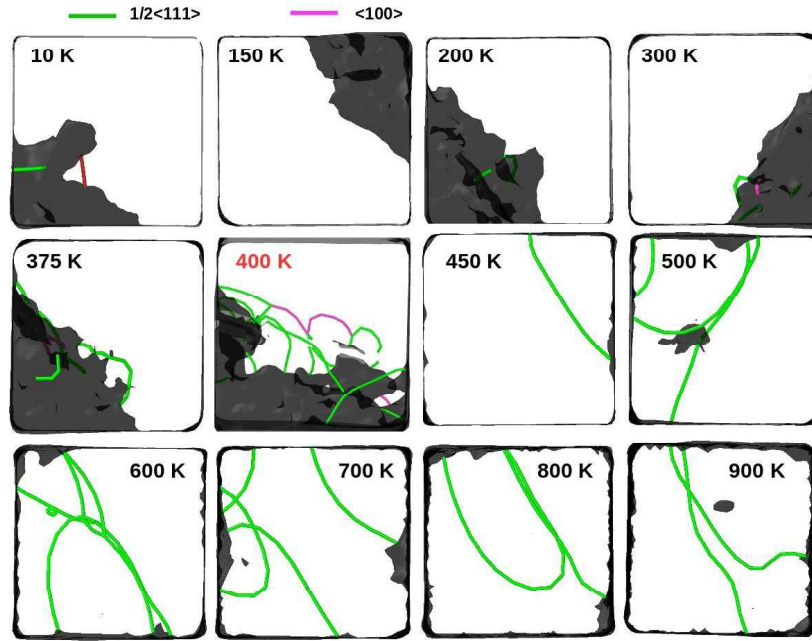
Figure 6.3: Defect nucleation at yielding in <111> BCC Fe nanowires at different temperatures. The green lines indicate the dislocations with the Burgers vector 1/2<111>, the magenta lines represent the dislocations with the Burgers vector <100>, and the dislocations with the unknown/unidentified Burgers vector are shown by red lines. The black regions indicate defective surfaces such as cracks.

any plastic deformation (Figure 6.4). These observations clearly suggest that <111> BCC Fe nanowires fail in brittle manner in the temperature range 10-350 K and the peak stress in the stress-strain curves reflects the fracture strength of the nanowires. At 400 K, apart from yielding through nucleation of crack, several mobile 1/2<111> and immobile <100> dislocations near crack tip have been observed (Figure 6.3). With increasing deformation, the crack gets blunted by dislocation activity and as a result, the nanowire at 400 K exhibits considerable plastic deformation and fails in ductile manner at high strains.

Contrary to crack nucleation at low temperatures, the nanowires yield through the nucleation of multiple 1/2<111> dislocations at high temperatures in the range 450-1000 K (Figure 6.3). Therefore, the peak stresses in the stress-strain curves at high temperatures necessarily indicate stress for the nucleation of dislocations in an otherwise perfect nanowire. At high temperatures, yielding through dislocation nucleation followed by plastic deformation results in flow stress drop to non-zero values (Figure 6.1b). The atomic configurations representing typical yielding and plastic deformation of nanowires at high temperatures (450-1000 K) are shown for 700 K in Figure 6.5. The yielding by the nucleation of dislocations from the nanowire corner can be seen in Figure 6.5a. It can also be seen that the dislocations nucleated from the
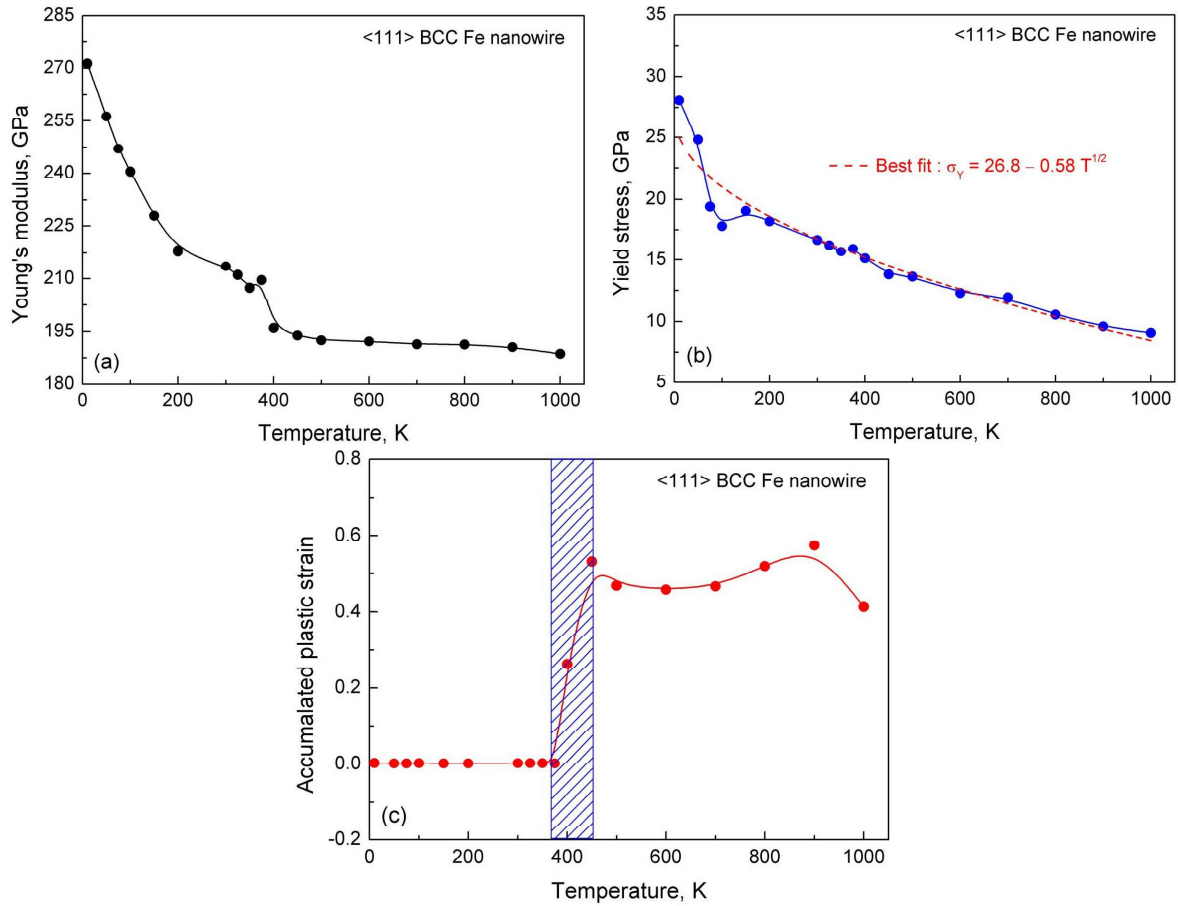
Figure 6.2: Variations of (a) Young's modulus, (b) yield stress, and (c) accumulated plastic strain as a function of temperature for <111> BCC Fe nanowires. Temperature (T) dependence of yield stress σ_Y obeying $\sigma_Y = A - B\sqrt{T}$ with A = 26.8 and B = 0.58 is superimposed as the broken line in (b). The blue dashed region in (c) shows a ductile to brittle transition regime. The center of this regime has been taken as the transition temperature.

temperature of 400 K, the nanowire yields primarily through the nucleation of crack associated with many mobile 1/2<111> and immobile <100> dislocations in the vicinity of the crack (Figure 6.3). At temperatures higher than 400 K, the nanowires yielded only by the nucleation of multiple 1/2<111> dislocations. In the temperature range 450-1000 K, no crack nucleation has been observed. The atomic snapshots as function of strain at 50 K representing the deformation behaviour of <111> BCC Fe nanowires at low temperatures is shown in Figure 6.4. It can be seen that the crack nucleates from the corner of the nanowires without any dislocations at the tip (Figure 6.4a) and grows rapidly along the direction at 45° angle with the loading axis (Figures 6.4b and 6.4c). During crack growth, a few 1/2<111> and <100> dislocations in the vicinity of crack tip can be seen in Figures 6.4b and 6.4c. The growing crack reaches the opposite surface within a short strain interval and the nanowire fails abruptly without showing

119

The variations in Young's modulus, yield stress, and the accumulated plastic strain before failure as function of temperature are shown in Figures 6.2a-6.2c. In the presence of non-linear elastic deformation, the values of Young's modulus at different temperatures have been evaluated from the slope of initial linear elastic regime i.e. the slope of stress-strain curves for $\varepsilon < 0.04$. Below this strain, the stress-strain curve is nearly linear for all temperatures. The non-linear portion at high elastic strains ($\varepsilon > 0.04$) has been neglected for Young's modulus calculations. It can be seen that Young's modulus decreases rapidly up to 400 K followed by saturation at higher temperatures (Figure 6.2a). The variations in yield stress with respect to temperature exhibited a rapid decrease in yield stress up to 100 K followed by a gradual decrease with the increase in temperature (Figure 6.2b). At about 100 K, a hump in yield stress or a concave down region can be seen in Figure 6.2b. Temperature (T) dependence of yield stress (σ_Y) obeying $\sigma_Y = A - B\sqrt{T}$ with A = 26.8 and B = 0.58 is superimposed as the broken line in Figure 6.2b. The yield stress values at all temperatures have been observed to be consistently lower than the theoretical strength of 27.6 GPa reported for <111> BCC Fe [107]. It is interesting to observe that apart from insignificant flow stress (Figure 6.1a), the nanowires exhibit a negligible plastic strain during tensile deformation at low temperatures in the range 10-375 K (Figure 6.2c). A significant increase in the accumulated plastic strain with the increase in temperature from 375 to 500 K can be seen in Figure 6.2c. Beyond 500 K, the plastic strain remains nearly constant. The accumulated plastic strain is obtained from stress-strain curves as total strain to failure minus elastic strain (strain to yielding). The negligible amount of accumulated plastic strain obtained at lower temperatures arises from crack nucleation and growth till separation into two pieces. At higher temperatures, significant plastic deformation leading to failure results in higher values of accumulated plastic strain. From the variations in accumulated plastic strain before failure with temperature, it is clear that <111> BCC Fe nanowires undergo ductile-brittle transition with 400 K as a transition temperature (Figure 6.2c).

6.4 Deformation behaviour and failure mechanisms

In order to understand the variations in stress-strain behaviour, the atomic configurations have been analysed using OVITO as a function of strain at different temperatures. Figure 6.3 shows the top view of nanowires during yielding at various temperatures. It can be seen that at low temperatures (10-375 K), yielding in the nanowires occurs mainly through the nucleation of a sharp crack with negligible dislocation activity at the crack tip (Figure 6.3). At transition

may be due to the weird behaviour of surface atoms at low temperatures or it may arise from the inter-atomic potential. Following elastic deformation up to peak stress, yielding results in abrupt drop in flow stress in all the nanowires. The yield stress values have been obtained as the values of peak stress in the stress-strain curve. Following yielding, the <111> BCC Fe nanowires display two different behaviours during plastic deformation as shown for low (10-375 K) and high (400-1000 K) temperatures in Figures 6.1a and 6.1b, respectively. At low temperatures, the flow stress abruptly drops to zero indicating insignificant plastic deformation and sudden failure in the nanowires (Figure 6.1a). On the other hand, the flow stress dropping to non-zero value followed by jerky flow and gradual decrease in flow stress during plastic deformation suggests ductile nature of nanowires at high temperatures (Figure 6.1b).
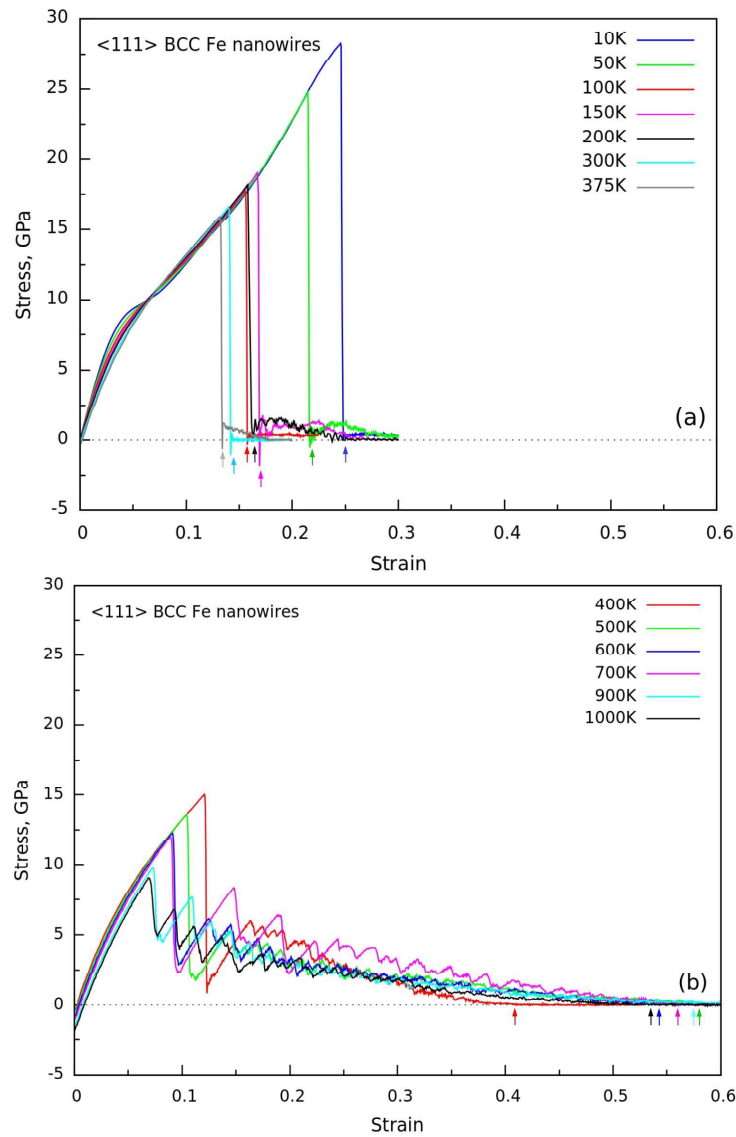
Figure 6.1: Stress-strain behaviour of <111> BCC Fe nanowires at (a) low (10-375 K) and (b) high (400-1000 K) temperatures. The failure locations have been marked by arrows.

6.2 Simulation details

MD simulations were performed in LAMMPS package [94] employing an EAM potential for BCC Fe given by Mendelev and co-workers [75]. BCC Fe nanowires of square cross-section width (d) = 8.5 nm and oriented in <111> axial direction with {110} and {112} side surfaces were created by generating atomic positions corresponding to the bulk Fe. Correspondingly, the simulation box contained about 110000 Fe atoms arranged in BCC lattice. The length (l) was twice the cross section width (d) of the nanowire. Periodic boundary conditions were chosen along the length direction, whereas the other two directions were kept free. After the initial construction of the nanowire, the energy minimization was performed by a conjugate gradient (CG) method to obtain a relaxed structure with equilibrium atomic positions corresponding to the nanowire. The minimization has been carried out until the energy change between two successive iterations divided by the initial energy is less than 10^{-6}. To put the sample at the required temperature, all the atoms have been assigned initial velocities according to the Gaussian distribution. Following this, the nanowire system was thermally equilibrated to a required temperature for 125 ps in canonical ensemble (constant NVT). The temperature is controlled with Nose-Hoover thermostat with a damping constant of 500 fs for all temperatures. This value of damping constant has ensured that the temperature fluctuations are always lower than 1% during simulation irrespective of test temperature. The velocity verlet algorithm has been used to integrate the equations of motion with a time step of 5 fs.

Following thermal equilibration, the tensile deformation was performed at a constant strain rate of 1×10^8 s^{-1} along the axis of the nanowire. In order to reveal the brittle to ductile transition temperature, the atomistic simulations have been performed at different temperatures in the range 10-1000 K. The simulations at each temperature have been repeated five times, with a different random number seed for velocity distribution each time. The visualization of atomic configurations was performed using OVITO [103].

6.3 Stress-strain behaviour

Figure 6.1 shows stress-strain behaviour of <111> BCC Fe nanowires at various temperatures ranging from 10 to 1000 K. It can be seen that all the nanowires undergo an elastic deformation and exhibit non-linear behaviour at high strains. Further, during elastic deformation at 10 and 50 K, a bump appears in the stress-strain curve at a strain value of 0.04-0.05. This bump

Chapter 6

Ductile-brittle transition in <111> BCC Fe nanowires

6.1   Introduction

It is well known that the BCC materials are generally difficult to deform at low temperatures giving rise to brittle fracture, while at high temperature they deform easily and fail by ductile mode. As a result, most of the BCC materials show a ductile to brittle transition (DBT) with respect to temperature. For example, the bulk single crystal BCC Fe exhibits DBT with decreasing temperature [150]. The temperature for DBT in the bulk BCC Fe single crystal has been found to vary in the range 130-154 K depending on the strain rate. In addition to single crystal BCC Fe, Fe-9%Cr and Fe based ferritic steels also exhibit the DBT [151, 152]. At nanoscale, the DBT with respect to temperature has been observed in semiconductor nanowires such as GaN [153], ZnO [154], and Si [155]. Similar transition has also been reported in Cu nanowires with respect to size [34, 35] and Ag nanowires with respect to the strain rate [156]. In this context, it is important to examine the possibility of similar ductile to brittle transition in BCC nanowires. In chapter 3, it has been shown that, among the five different orientations of BCC Fe nanowires, the <100>, <110>, <112> and <102> orientations show significant plastic deformation even at 10 K, while the <111> nanowire show negligible plastic deformation. In view of this, <111> orientation has been chosen to study the ductile-brittle transition in BCC Fe nanowires. MD simulations have been performed on tensile deformation of <111> BCC Fe nanowires at different temperatures ranging from 10 to 1000 K. Special attention has been paid towards the amount of accumulated plastic strain, nature of yielding and final failure. The influence of cross-section size, shape and applied strain rate on the DBT has also been described in this chapter.

the presence of dislocations in BCC Fe nanowire mainly influences the twinning mechanism. The deformation by slip of dislocations is preferred over twinning in the presence of dislocations. Further, the deformation in <100> nanowire with multiple twist boundaries indicated that, increasing the dislocation density increases the contribution of slip and delays/prevents the occurrence of twinning. The present study may explain the absence of deformation twinning in bulk materials, which inherently contains many dislocations.

Molecular dynamics simulations performed on twinned BCC Fe nanopillars indicated that the twin boundaries have a contrasting role under tensile and compressive loadings. Under tensile loading, the yield stress has been almost independent of twin boundary spacing, while under compressive loading, the yield stress showed strong dependence on twin boundary spacing. This contrasting behaviour in yield stress has been explained by repulsive force offered by the twin boundaries. Under tensile loading, deformation is dominated by the twin growth/twin boundary migration, where the initial twin boundary offers negligible repulsive force on the nucleation of twinning partials. Due to this, yield stress varies marginally as a function of twin boundary spacing. In addition to twinning, minor activity of full dislocations and twin-twin interactions of <021> type have been observed during tensile deformation. It has been found that the edge of the curved twin boundary can acts as a source for the emission of full dislocations. The deformation under compressive loading is dominated by the slip of full dislocations, where the twin boundaries offer a strong repulsive force for the nucleation of full dislocations. This leads to the observed strong dependence of yield stress on twin boundary spacing. The dislocation-twin boundary interactions obtained under the compressive deformation of twinned nanopillars revealed that the dislocation can either directly transmit without any deviation in slip plane or it can transmit on symmetrical slip plane in the neighbouring grain.

are comparable for small spacing (i.e. nanopillars having three and five twin boundaries) and lower, for large spacing (Figure 7.8a-b). This difference in yield stress between perfect and twinned nanopillars may arise mainly from the structure of twin boundary in BCC Fe. With Mendelev EAM potential, the twin boundary in BCC Fe has a displaced or isosceles structure [20, 21], where the upper grain is displaced with respect to the lower grain parallel to the boundary plane by the vector 1/12<111>. In twinned nanopillars, this extra step can acts as a nucleation site for a twin embryo, while in perfect nanopillars, the twin embryo nucleates from the corner. Due to this extra step, the defect nucleation in the twinned nanopillars is easier than in perfect nanopillar. Under compressive loading, the observed low yield stress values for higher twin boundary spacing (i.e. nanopillars with one and two twin boundaries) can arise from the presence of such step. Further, the observed yield stress values for low twin boundary spacing (i.e. nanopillars with three and five twin boundaries) comparable to perfect nanopillar can be ascribed to the combined effects associated with repulsive force and step.

The most important aspect of atomistic simulations is the reliability of inter-atomic potential. Therefore, it is important to understand that up to what degree the predictions made in the present investigation differ with potential. Cao [61] in his study on shape memory and pseudo-elasticity of <100> BCC Fe nanowires has shown that under tensile deformation, the qualitative stress-strain behaviour and deformation behaviour by twinning doesn't vary significantly with Mendelev [75] and Chamati [72] potentials. However, these two potentials predict different values of yield stress [61]. On similar lines, the quantitative values of yield stress predicted in the present investigation may vary with inter-atomic potential, but the qualitative aspects may not change significantly.

7.3 Conclusions

Molecular dynamics simulations have been performed on the deformation behaviour of BCC Fe nanowires containing twist and twin boundaries. The results indicate that the twist boundaries in BCC Fe contain a network of dislocations. In <100> nanowire dislocation network has square shape, while in <110> nanowire it has hexagonal shape. The MD simulation results on the tensile deformation of <100> BCC Fe nanowires containing twist boundary indicated that the deformation proceeds through slip of dislocations at small strains followed by twinning at higher strains. On the other hand, the deformation in <110> BCC Fe nanowires containing twist boundary is dominated by the slip of dislocations at all strains. These results suggest that

and subsequent plastic deformation mechanisms under tensile and compressive loadings. The observed deformation mechanisms are summarised schematically in Figure 7.21. Since the deformation under tensile loading is dominated by the twinning partial dislocations (Figures 7.9 -7.12), the glide plane and the Burgers vector of this partials can either have an inclination or parallel with respect to twin boundary (Figure 7.21a). In case of an inclination, the repulsive force on the partial dislocations is smaller than that of full dislocations and as a result, the yield stress under tensile loading exhibits weaker dependence on twin boundary spacing. In other case, where the glide plane and the Burgers vector of partial dislocations are parallel to twin boundaries (Figure 7.21a), the twin boundary spacing has a insignificant role on yield stress due to negligible repulsive force [182, 196]. On the other hand, when the deformation is dominated by full dislocations under compressive loading (Figures 7.14 and 7.15), the slip plane and the Burgers vector of full dislocations have an inclination with respect to the twin boundary (Figure 7.21b). This mode of deformation is known as hard mode in FCC nanopillars [182]. In this mode, the twin boundaries exert strong repulsive force on full dislocations and also influence the resistance to dislocation slip. The repulsive force on the dislocations increases upon decreasing twin boundary spacing and as a result, the yield stress increases with the decrease in twin boundary spacing.
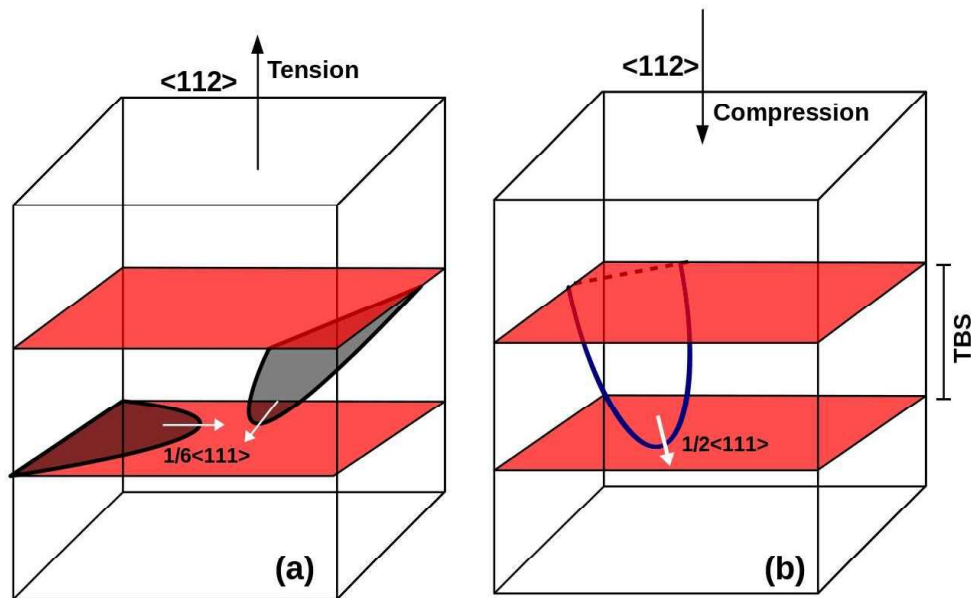
Figure 7.21: Schematic of the observed deformation mechanisms under (a) tensile and (b) compressive deformation of BCC Fe nanopillars.

The yield stress of twinned nanopillars under tensile loading is much lower than the yield stress of perfect nanopillar (Figure 7.7a-b), while in compression the strength values

154

the neighbouring grain (Figure 7.19). In BCC metals, three {112} and three {110} planes have the same <111> zone axis (Figure 7.20a). Interestingly, this arrangement of glide planes remains same across the twin boundary (Figure 7.20b). In view of this similarity in slip planes, dislocation once passes through the twin boundary can either glide on symmetrical plane or can directly comes out in the neighbouring grain without any deviation in the glide plane. The inserted atomic snapshots in Figure 7.20b shows that that the observed slip lines in Figures 7.18 and 7.19 are parallel to {112} planes. The geometrical arrangement of glide plane (Figure 7.20b) indicates that the observed dislocation-twin boundary interactions in the present study are on expected lines in BCC metals.
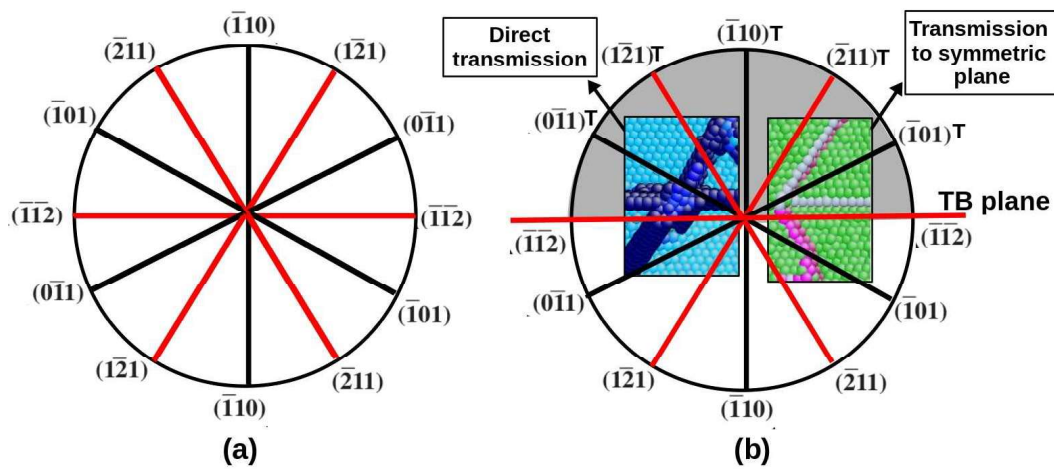
Figure 7.20: The arrangement of three {110} and three {112} planes having the same <111> zone axis in (a) perfect and (b) across the twin boundary in twinned BCC crystals.

7.2.9   Effect of twin boundary spacing on yield stress

The yield stress as a function of twin boundary spacing exhibiting contrasting behaviour under tensile and compressive loadings has been observed in BCC Fe nanopillars. During tensile deformation, the yield stress displays negligible variation with respect to twin boundary spacing (Figure 7.7b), while a significant decrease in yield strength with increasing twin boundary spacing has been observed under compressive loading (Figure 7.8b). The observed variations in yield stress with respect to twin boundary spacing under tensile and compressive loadings are in agreement with those reported in twinned FCC nanopillars [183–186]. In twinned FCC nanopillars, the strengthening and negligible influence of twin boundary spacing was explained using the hard and soft modes of deformation [182, 196]. In BCC Fe nanopillars, this contrasting behaviour in the yield stress variations can arise mainly from the difference in yielding

153

grows with deformation (Figure 7.18a). Once the part of the dislocations reaches the twin boundary, the dislocation line becomes parallel to the intersection line of the glide plane and twin boundary (Figure 7.18b). With increasing strain, this dislocation passes through the twin boundary and glides on the plane parallel to the initial glide plane (Figure 7.18c). In addition to full dislocation directly transmitting through the twin boundary (Figure 7.18), another operating mechanism of dislocation transmission across the twin boundary is shown in Figure 7.19. In this case, the dislocation comes out of the twin boundary and glides on a plane symmetrical to the initial glide plane (Figure 7.19a-c).
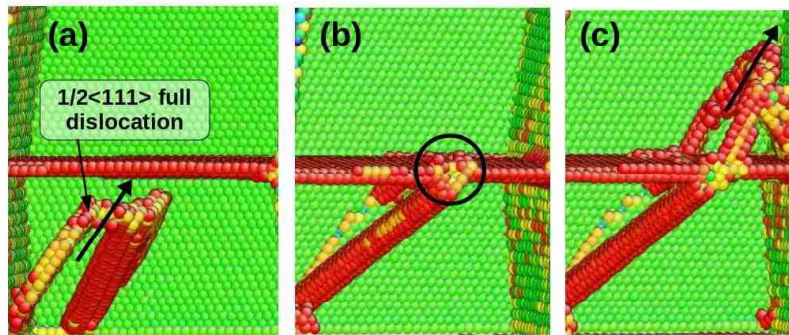
Figure 7.18: Dislocation-twin boundary interaction showing direct transmission of dislocation across the twin boundary. The viewing direction is <111> and the atoms are coloured according to the centro-symmetry parameter. The perfect BCC atoms and the front surface are removed for clarity.
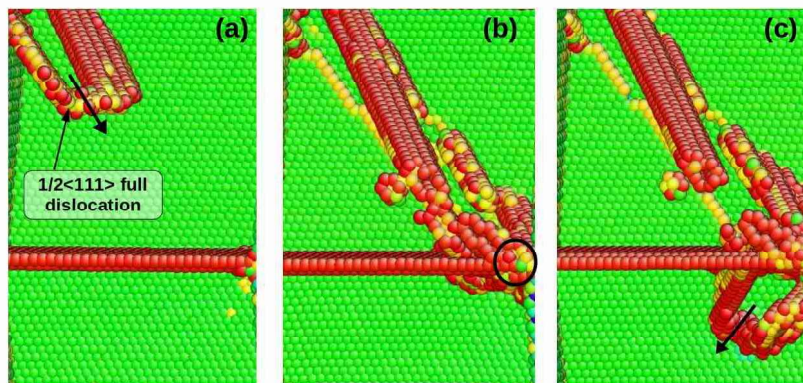
Figure 7.19: Dislocation-twin boundary interaction showing the symmetrical transmission of dislocation across the twin boundary. The viewing direction is <111> and the atoms are coloured according to the centro-symmetry parameter. The perfect BCC atoms and the front surface are removed for clarity.

Dislocation-twin boundary interactions during the compressive deformation of BCC Fe nanopillars reveal that the dislocation can either directly transmits through twin boundary without any deviation in glide plane (Figure 7.18) or it can transmits to symmetrical plane in
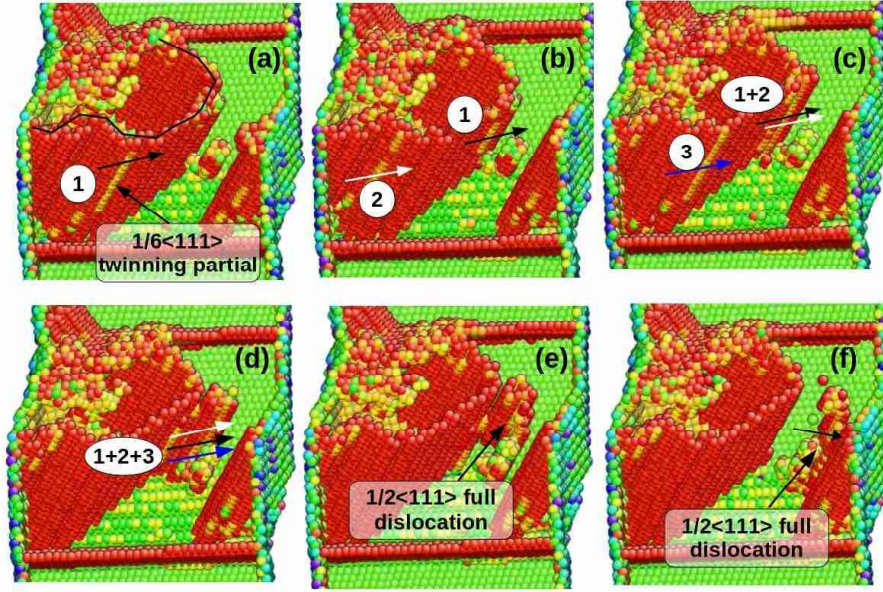
Figure 7.17: Process of full dislocation nucleation from the edge of curved twin boundary during tensile deformation of twinned BCC Fe nanopillar. The atoms are coloured according to the centro-symmetry parameter. The perfect BCC atoms and the front surface are removed for clarity.

the edge of the twin boundary. The nucleation of dislocation from the edge of the curved twin boundary is associated with the reduction in the thickness of twin (Figure 7.17a-f). The dislocation nucleation from the edge of curved twin boundary observed in the present investigation (Figure 7.17) is in agreement with those obtained experimentally by Hull [195] in bulk BCC Fe. In BCC metals, the twin boundary or the twin-matrix interface can have different shapes such as lenticular, flame-like structure and complicated fine structure of serrations [120]. The edges or the serrations can acts as a stress concentration site. In order to relieve this localised stress, full dislocation nucleates from the edges of the curved twin boundary and glide on {110} plane [195].

7.2.8 Dislocation-twin interactions

As the deformation of twinned nanopillars under the compressive loading is dominated by the full dislocations, it can offer an insight into dislocation-twin boundary interactions. In the present investigation, the dislocation-twin interactions have been observed for all the nanopillars under compressive loading. The direct transmission of $1/2<111>$ full dislocation across the twin boundary without any deviation in glide plane is shown in Figure 7.18. Initially, $1/2<111>$ full dislocation loop nucleates from the corner of nanopillar during yielding and
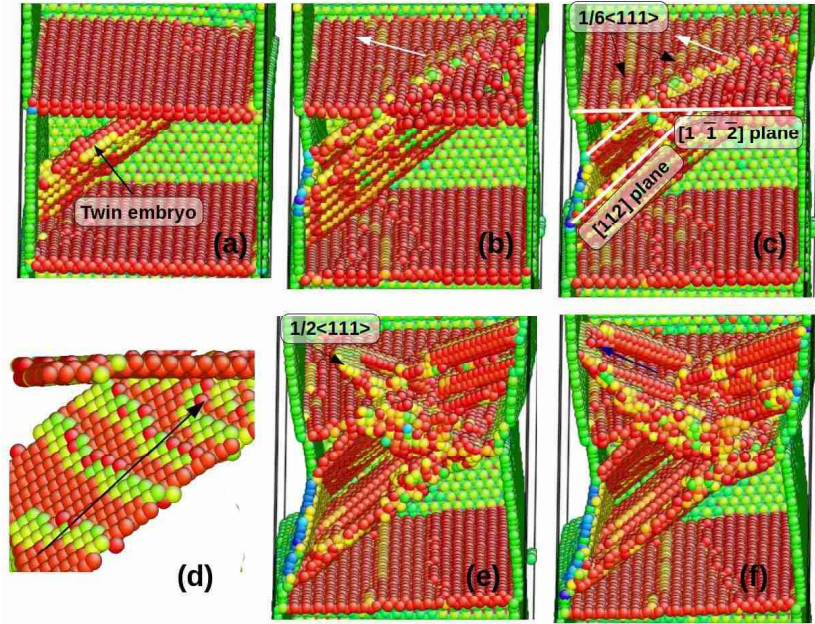
Figure 7.16: Twin-twin interaction under the tensile loading of twinned BCC Fe nanopillars. The nucleated twin on [112] plane interacts with the initial twin boundary on [1$\bar{1}\bar{2}$] plane and produces a <012> type twin-twin intersection. <012> twin-twin intersection is obtained as the cross product of (112) and (1-1-2). The full dislocation emission from the twin-twin interaction can be seen in (c) and (d). The atoms are coloured according to the centro-symmetry parameter. The perfect BCC atoms and the front surface are removed for clarity.

7.2.7   Twin boundary as a dislocation source

Under the tensile deformation of twinned BCC Fe nanopillars, it has been observed that the nucleated twin boundary can often be of curved nature and edge of this curved twin boundary can acts as a source for nucleation of full dislocations. Figure 7.17 shows pictorial view of full dislocation emission from the curved twin boundary. Initially, 1/6<111> partial dislocation labelled as '1' nucleates and glides along the curved twin boundary (Figure 7.17a). The motion of this partial dislocation is prevented at the edge of the twin boundary, and at the same time, another partial dislocation labelled as '2' nucleates and approaches towards the edge of twin boundary (Figure 7.17b). These two partial dislocations combine and form a 1/3<111> partial dislocation labelled as '1 + 2' in Figure 7.17c. With a small increase in strain, one more 1/6<111> partial dislocation labelled as '3' gets nucleated, and its subsequent glide and combination with the existing combined 1/3<111> partial dislocation leads to the formation of 1/2<111> full dislocation as shown in Figure 7.17d. Thus, the nucleation of three successive partial dislocations and their pile up at the edge of the twin boundary leads to the formation of full dislocation. The 1/2 <111> full dislocation glide on {110} plane and moves away from

three and five twin boundaries, accrual of comparatively smaller screw dislocations have been noticed (Figure 7.15c and d). Furthermore, due to dislocation blockage by twin boundaries, the formation of hairpin-like dislocations has been observed during compressive deformation of twinned nanopillars with higher number of twin boundaries (Figure 7.15d). The dislocations that glide in hairpin-like configuration are known as hairpin dislocations and this kind of dislocations have also been observed in twinned FCC nanocrystalline materials [193].

7.2.6   Twin-twin interactions

As the deformation under tensile loading of twinned nanopillars is dominated by twinning mechanism, it can offer an insight into twin-twin interactions. Figure 7.16 shows twin-twin interactions under tensile loading of twinned nanopillars observed in the present study. Initially, the twin embryo consisting of many partial dislocations nucleates from the corner of the nanopillar and propagates towards the initial twin boundary (Figure 7.16a). The nucleated twin on [112] plane interacts with initial twin boundary on $[1\bar{1}\bar{2}]$ plane and produces $<012>$ twin-twin intersection (Figure 7.16b). In all the nanopillars undergoing twinning, $<012>$ type twin-twin intersections have been observed. In BCC metals, the twin-twin interactions have been classified based on their common line of intersection [194]. The observed $<021>$ type twin intersection is in agreement with the fact that in BCC metals, there are only five types of probable twin-twin intersections, namely $<011>$, $<012>$, $<113>$, $<111>$ and $<135>$ [194]. Among these five intersections, Ojha et al. [191] characterised $<110>$, $<113>$ and $<210>$ type twin-twin intersections in BCC Fe using experiments and molecular dynamics simulations. Due to twin-twin interaction, the formation of the twinning partials gliding along the twin boundary can be seen in Figure 7.16b and c. The other possibility of twin-twin interactions arise from the pile-ups and combination of twinning partial dislocations (Figure 7.16d). During deformation, the gliding twinning partials along the nucleated twin boundary pile-up against the initial twin boundary (Figure 7.16d). Following the pile-ups, three of twinning partials combine and form a full dislocation (Figure 7.16e). Upon increasing strain, the lattice near the twin-twin intersection is highly distorted (Figure 7.16f). The full dislocations thus nucleated, glide on the plane symmetrical with respect to the plane of nucleated deformation twin.

(a) ε = 0.08   **(b) ε = 0.082**   **(c) ε = 0.084**

Figure 7.14: Deformation behaviour of BCC Fe nanopillar containing two twin boundaries under the compressive loading. The atoms are coloured according to the centro-symmetry parameter. The perfect BCC atoms and the front surface are removed for clarity.

tion motion. With increase in stress, the blocked dislocation penetrates the twin boundary and comes out as a loop in the next grain (Figure 7.14c). During this process of nucleation and propagation, the accumulation of large of number of straight screw dislocations can be seen at higher strains in all the nanopillars (Figure 7.15a-d). The accumulation process of straight screw dislocations in BCC nanowires has also been demonstrated in <110> BCC Fe nanowire (Chapter 4). In nanopillars containing one and two twin boundaries, accumulation of long and straight screw dislocations has been observed (Figure 7.15a and b), while nanopillars having

(a)   **(b)**   **(c)**   **(d)**
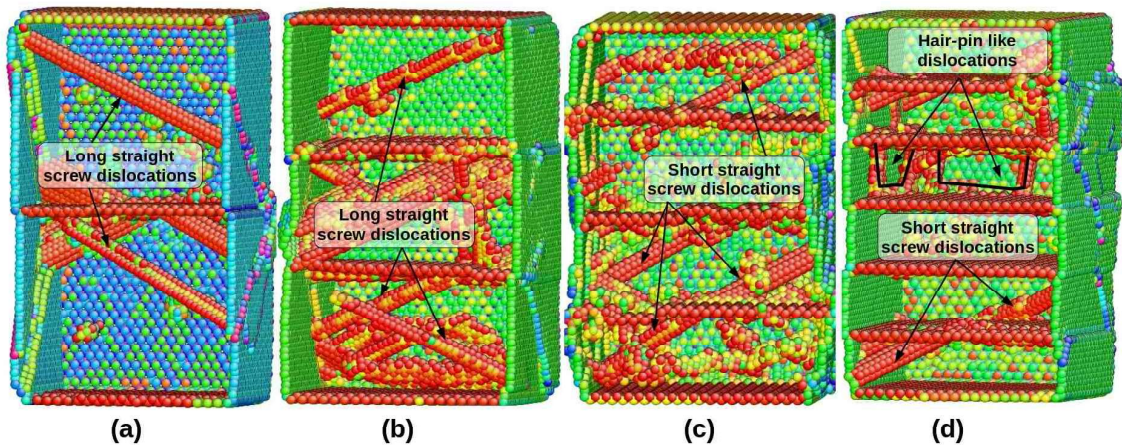
Figure 7.15: Accumulation of straight screw dislocations in the twinned BCC Fe nanopillars under the compressive loading. The atoms are coloured according to the centro-symmetry parameter. The perfect BCC atoms and the front surface are removed for clarity.

148

7.2.5 Deformation behaviour under compression

In contrast to twinning under tensile loading, the deformation behaviour under compressive loading of perfect and twinned BCC Fe nanopillars is dominated mainly by the slip of full dislocations. Figure 7.13 shows the deformation behaviour of perfect BCC Fe nanopillar oriented in <112> axis under compressive loading. It can be seen that the yielding occurs by the nucleation of 1/2<111> full dislocations from the corner of the nanopillar (Figure 7.13a). Following yielding, the plastic deformation is entirely dominated by the slip of full dislocations. Due to glide of 1/2<111> screw dislocations, the straight and curved slip steps were observed on surface of the nanopillar (Figure 7.13b). Furthermore, the formation of large number of point defects can be seen in Figure 7.13b. The non-conservative motion of dislocations leads to the creation of point defects such as vacancies and/or interstitials.
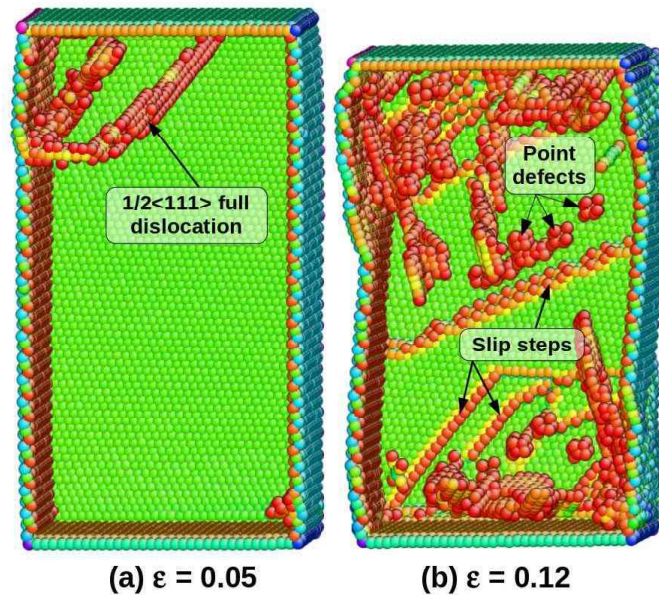
Figure 7.13: Deformation behaviour of perfect <112> BCC Fe nanopillar under compressive loading. The atoms are coloured according to the centro-symmetry parameter. The perfect BCC atoms and the front surface are removed for clarity.

The typical atomic configurations representing plastic deformation under compressive loading of twinned nanopillars containing two twin boundaries are shown in Figure 7.14. The onset of yielding is characterised by the nucleation of dislocation loop originating from the corner of the nanopillar (Figure 7.14a). The DXA analysis [104] indicated that the dislocation loop has a Burgers vector 1/2<111> representing full dislocations in BCC system. Following nucleation, the dislocation loop expands in diameter and the part of the loop is annihilated at the free surface, while the remaining part is blocked at twin boundary (Figure 7.14b). This indicates that the twin boundaries in BCC Fe nanopillars are effective barriers for disloca-

nanopillar axis (Figure 7.9d). Although, the overall deformation is dominated by twinning mechanism (Figure 7.9d), minor activity of full dislocation slip is also observed in the neighbouring grain (Figure 7.9c). However, this full dislocation slip contributes negligibly to the overall strain.

Similar to nanopillar having a single twin boundary, deformation through twinning has occurred in nanopillars containing higher number of twin boundaries (Figure 7.12). However, few important differences were noticed in nanopillars containing two, three and five twin boundaries. It can be seen that in nanopillar containing two twin boundaries, the twinning occurs only in two grains and no activity of slip is observed in any grain (Figure 7.12a). Moreover, the operative twin systems in these two grains are symmetrical with respect to twin boundary. In contrast, in nanopillars containing three and five twin boundaries, considerable activity of full dislocations is also observed (Figure 7.12b and c). This full dislocation activity is aided mainly by twin-twin interactions. Furthermore, the change in twin boundary spacing increases with increase in the number of twin boundaries and in nanopillars containing five twin boundaries, the twin boundary spacing has become uneven due to continuous glide of parallel twinning partials (Figure 7.12c). Upon increasing strain, the deformation is mainly concentrated at the twin boundaries in all the nanopillars, leading to the occurrence of necking close to one of the twin boundaries (Figure 7.12).
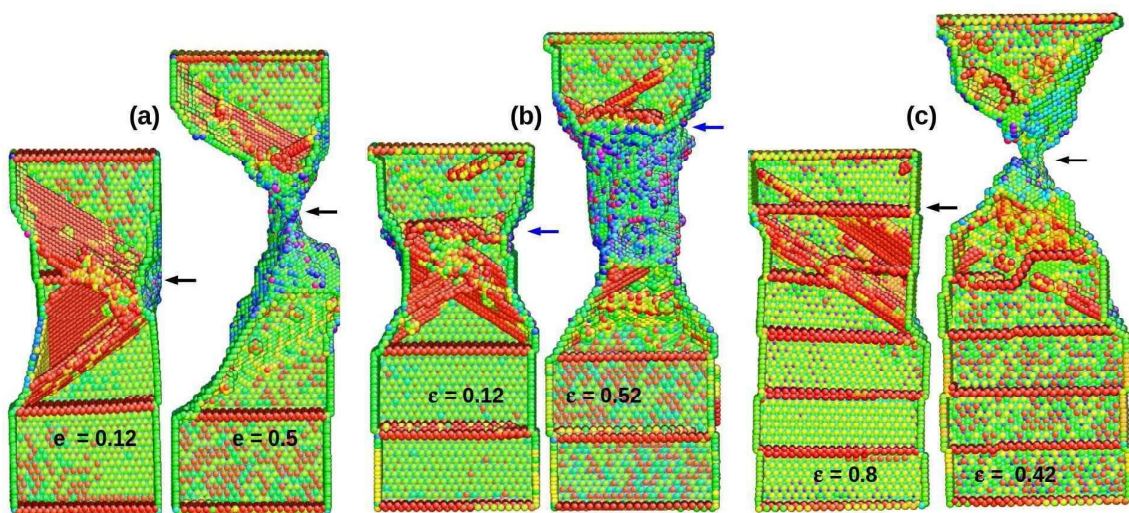
Figure 7.12: Deformation behaviour of BCC Fe nanopillars containing (a) two, (b) three and (c) five twin boundaries. The atoms are coloured according to the centro-symmetry parameter. The perfect BCC atoms and the front surface are removed for clarity.

location nucleates on {112} plane from the corner of the nanowire with a stacking fault behind (Figure 7.10a). Upon increasing deformation, this partial dislocation glides further in <111> direction (Figure 7.10b) and an additional 1/6<111> partial dislocations nucleates from the intersection of the surface and stacking fault as shown in Figure 7.10b and c. When twin front reaches the opposite surface, the twin embryo eventually becomes full twin enclosed by two {112} twin boundaries (Figure 7.10d). Following this, the twin grows along the nanowire axis by the successive nucleation and glide of 1/6<111> partial dislocations on adjacent {112} planes. Figure 7.11 shows the migration of initial twin boundary due to glide of 1/6<111> partial dislocations, which leads to change in twin boundary spacing. Each nucleation, glide and annihilation of 1/6<111> partial dislocation displaces the twin boundary by one layer. As a result of repeated nucleation and glide, the twin boundary migrates marginally along the
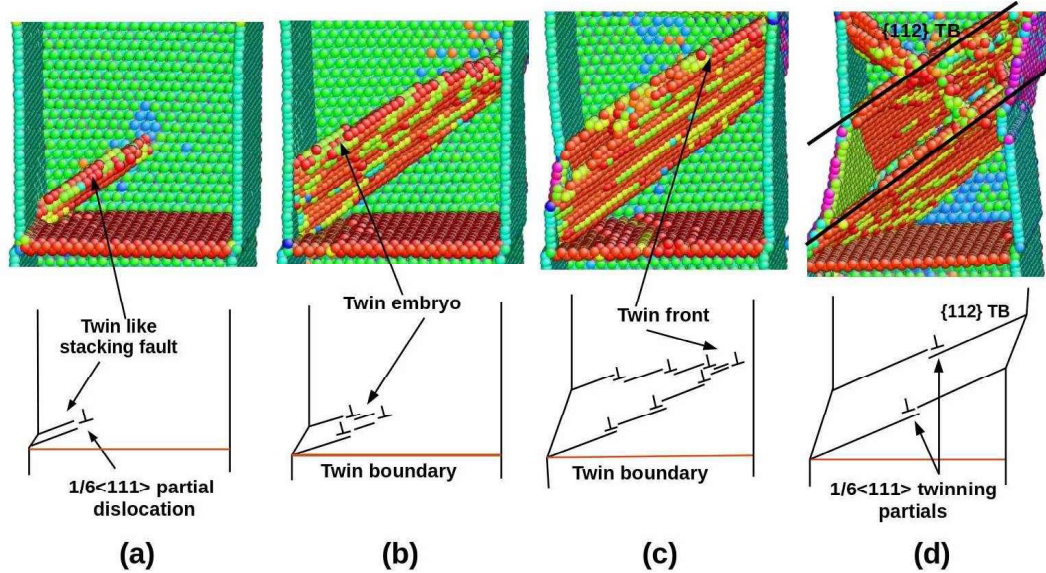
Figure 7.10: The detail process of twin embryo nucleation to twin boundary formation. The 2-D view of twin nucleation and growth is shown schematically in lower figures. The atoms are coloured according to the centro-symmetry parameter.
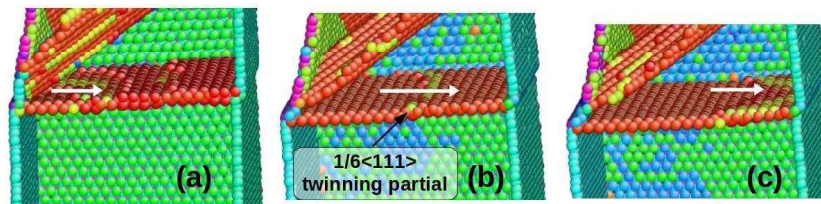
Figure 7.11: Typical glide of partial dislocations along the existing twin boundary. The continuous nucleation and glide of partial dislocations migrating the initial twin boundary is shown. The atoms are coloured according to the centro-symmetry parameter. The perfect BCC atoms and the front surface are removed for clarity.

or marginally higher (with five twin boundaries) than that in the perfect nanopillar (Figure 7.8b). In general, under compressive loading, all the nanopillars displayed large oscillations and gradual decrease in flow stress with progressive plastic deformation (Figure 7.8a).

7.2.4 Deformation behaviour under tensile loading

The evolution of atomic configurations at various stages of deformation during the tensile loading of the <112> perfect and twinned BCC Fe nanopillars has been analysed using centro-symmetry parameter. In Chapter 3, it has been shown that the deformation behaviour of perfect <112> BCC Fe nanowires is dominated by the deformation twinning along with the minor activity of dislocation slip. Similar to the perfect <112> nanopillar, the deformation in twinned nanopillars is also dominated by the twinning and associated partial dislocation mechanism. Figure 7.9 shows the deformation behaviour under the tensile loading of BCC Fe nanopillar containing a single twin boundary. The nanopillar yields by the nucleation of a twin embryo from the intersection of surface and the existing twin boundary (Figure 7.9a). Similar yielding behaviour was observed in nanopillars containing higher number of twin boundaries. With small increase in strain, the nucleation and glide of 1/6 <111> partial dislocation along the initial twin boundary can be seen in Figure 7.9b. The glide of partial dislocation leads to the migration of initial twin boundary and thereby changes the twin boundary spacing (Figure 7.9c and d). The detailed mechanism of twin boundary formation and the migration of initial twin boundary are shown in Figures 7.10 and 7.11 respectively. Initially the 1/6<111> partial dis-
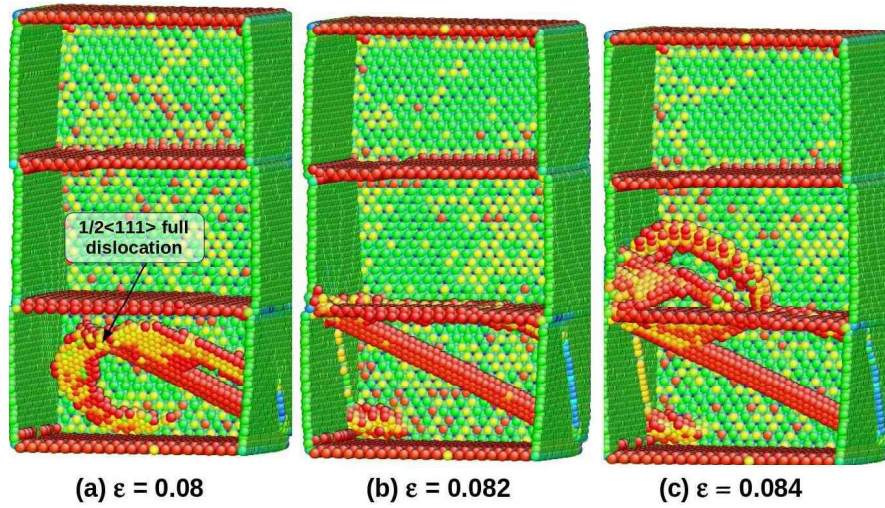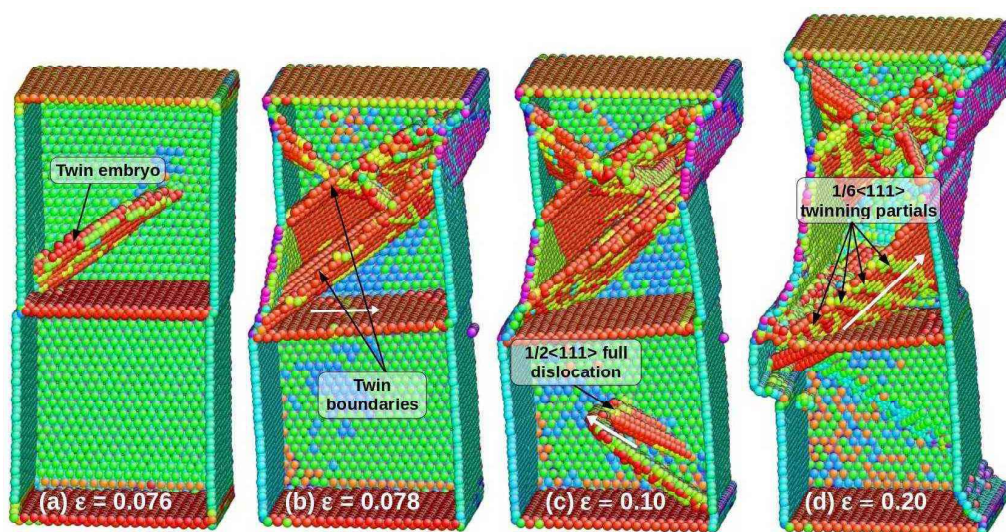

Figure 7.9: The deformation behaviour of BCC Fe nanopillar containing single twin boundary under tensile loading. The atoms are coloured according to the centro-symmetry parameter. The perfect BCC atoms and the front surface are removed for clarity.

linear elastic deformation, while the twinned nanopillars display linear elastic deformation at small strains followed by non-linear elastic deformation at high strains. In addition to this, the perfect nanopillar exhibited higher elastic modulus than those observed for twinned nanopillars. Following elastic deformation, the nanopillars displayed yielding characterised by an abrupt drop in flow stress. However, the drop in flow stress during yielding under compressive loading (Figure 7.8a) has been significantly lower than those under tensile loading (Figure 7.7a). Under compressive deformation, decrease in yield stress in the presence of a single twin boundary followed by an increase in yield stress with increase in the number of twin boundaries has been observed. Finally, the yield stress attains a value closer (with three twin boundaries)
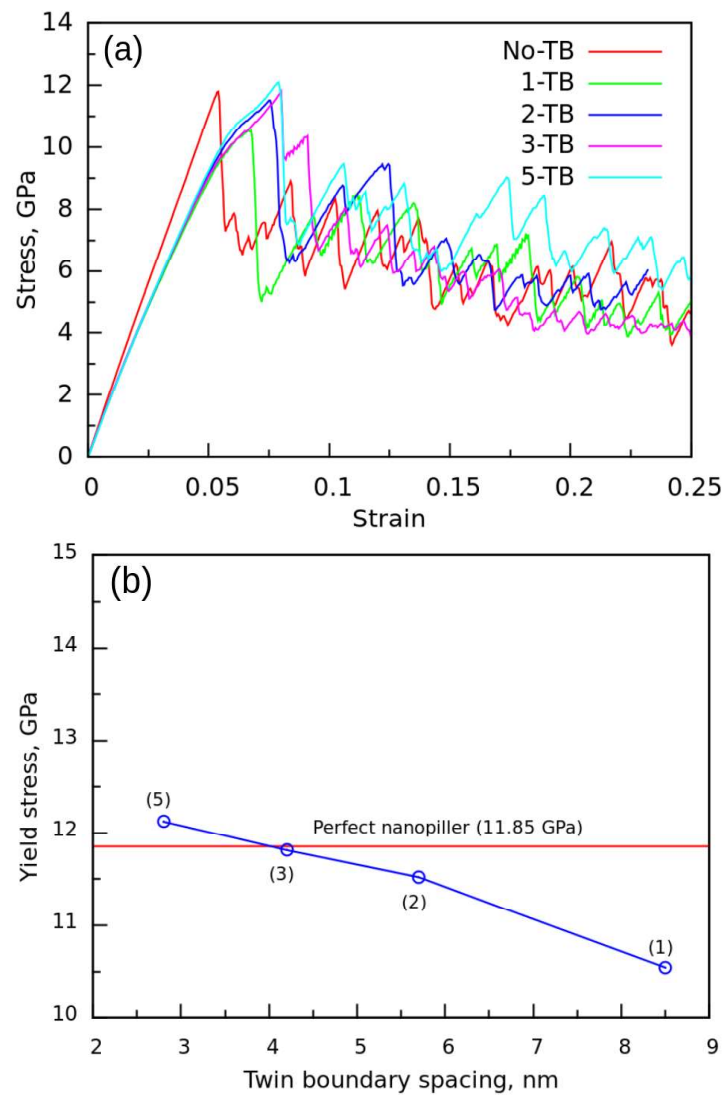
Figure 7.8: (a) Compressive stress-strain behaviour of perfect <112> and twinned BCC Fe nanopillars containing one, two, three and five twin boundaries. (b) Variation of yield stress as a function of twin boundary (TB) spacing under compressive loading. The yield stress of perfect <112> nanopillar is indicated by red line and the number of twin boundaries is shown in brackets in (b).

up to large strains. Contrary to this, the nanopillars containing one and two twin boundaries displayed a gradual decrease in the flow stress with increase in plastic deformation. A rapid decrease in flow stress with increase in plastic strain was observed for nanopillars having three and five twin boundaries. Further, the nanopillars having three and five twin boundaries shows higher flow stress with significant fluctuations at low plastic strains. A general decrease in strain to failure has been obtained in the twinned nanopillars compared to that in the perfect nanopillar.
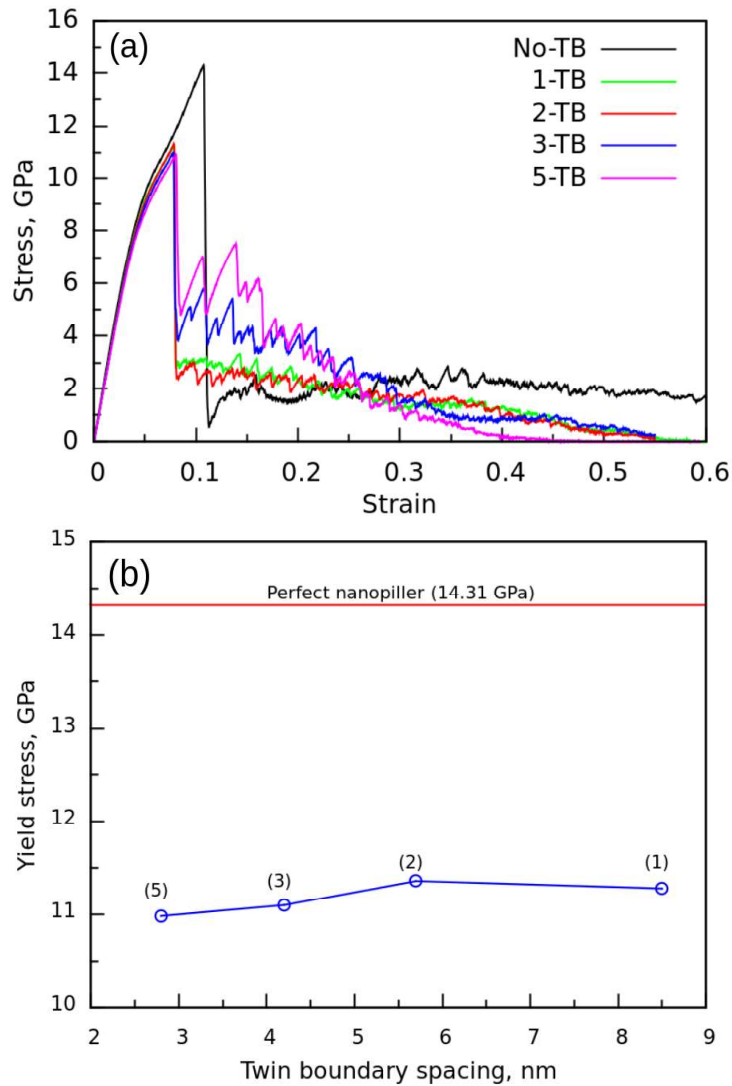
Figure 7.7: (a) Tensile stress-strain behaviour of perfect <112> and twinned BCC Fe nanopillars containing one, two, three and five twin boundaries. (b) Variation of yield stress as a function of twin boundary (TB) spacing in BCC Fe nanopillars under tensile loading. The yield stress of perfect <112> nanopillar is indicated by red line and the number of twin boundaries is shown in small brackets.

Figure 7.8a shows the stress-strain behaviour of perfect and twinned BCC Fe nanopillars under compressive loading. It can be seen that the defect free nanopillar exhibits perfect

different twin boundary spacings considered in this study along with perfect nanopillar are shown in Figure 7.6. Upon completion of equilibrium process, the deformation under tensile and compressive loadings was carried out in a displacement controlled mode at a constant strain rate of 1×10^8 s^{-1} by imposing displacements to atoms along the nanopillar length that varied linearly from zero at the bottom to a maximum value at the top layer.
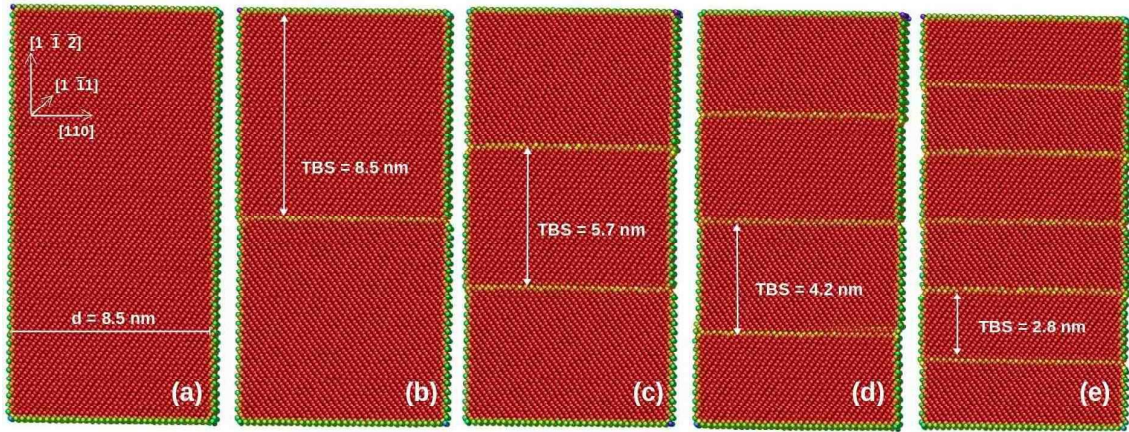
Figure 7.6: The initial configuration of (a) perfect BCC Fe nanopillar and the nanopillar consisting of (b) one (c) two (d) three and (e) five twin boundaries. The corresponding twin boundary spacings (TBS) of 8.5, 5.7, 4.2 and 2.8 nm are shown. The atoms are coloured according to the centro-symmetry parameter.

7.2.3 Stress-strain behaviour

The stress-strain behaviour of BCC Fe nanopillars under tensile loading containing one, two, three and five twin boundaries along with the perfect nanopillar is shown in Figure 7.7a. All the nanopillars exhibited linear elastic deformation at small strains followed by non-linearity at higher strains, i.e. $\varepsilon > 0.05$. The modulus evaluated from the linear elastic regime displayed insignificant variations and this indicated that the elastic modulus is not influenced by the presence of twin boundaries. Following elastic deformation, the large and abrupt drop in flow stress signifying the occurrence of yielding in the perfect and twinned nanopillars is seen in Figure 7.7a. In BCC Fe, introduction of twin boundaries resulted in the significant reduction in yield stress compared to that in perfect nanopillar. Similarly, a decrease in the strain to yielding has also been observed in the twinned nanopillars. The yield stress exhibited only marginal variation with respect to twin boundary spacing as shown in Figure 7.7b. For comparison, the yield stress of perfect nanopillar is shown as horizontal line in Figure 7.7b. Following yielding, the perfect nanopillar exhibited nearly a constant and low flow stress during plastic deformation

the twin boundary in BCC system possesses higher energy than the corresponding twin boundary in FCC system [18]. In view of different interface energies and twin boundary structures, the effect of twin boundaries in BCC systems may be different than that in FCC systems. In view of this, an attempt has been made in the present investigation to study the influence of twin boundaries on the deformation behaviour under tensile and compressive loadings in BCC nanopillars using atomistic simulations.

An examination of the deformation behaviour of twinned nanopillars also offers valuable insights into twin-twin and dislocation-twin interactions. In FCC metals, the dislocation-twin boundary and twin-twin interactions are well understood, and can be described by the notation of double Thompson tetrahedron [188, 189]. The absence of such simplified notation and non-planer core of screw dislocations along with the presence of twinning-antitwinning sense on {112} planes make it difficult to understand the dislocations-twin boundary interactions in BCC metals. There are only a couple of studies pertaining to the dislocation-twin and twin-twin interactions in BCC metals [190–192]. In view of the above observations, the present study is aimed at understanding the role of twin boundaries and the mechanisms responsible for strengthening or softening behaviour in BCC Fe nanopillars. It is also aimed at characterising the twin-twin and dislocation-twin interactions observed during the deformation.

7.2.2 Simulations details

In order to create twinned nanopillars, the following procedure was adopted. Initially, the single crystal BCC Fe nanopillars of square cross section width (d) = 8.5 nm and consisting of about 110,000 atoms oriented in <112> axial direction with {110} and {111} as side surfaces was constructed. The nanopillar length (l) was twice the cross section width (d). Then, the twin boundaries were introduced by rotating one part of the crystal with respect to other by 180° around <112> axis. Following the rotation, the twin boundary forms at their interface on {112} plane. The formed twin boundary is equivalent to a twist boundary lying on {112} plane with a twist angle of 180° (Figure 7.1). Similar procedure was followed to create more number of twin boundaries. The model system was equilibrated to a temperature of 10 K in NVT ensemble. In all the nanopillars, no periodic boundary conditions were used in any direction. Following the relaxation, the twin boundary having displaced structure was observed [20, 21]. The nanopillars containing one, two, three and five twin boundaries resulted in the twin boundary spacings of 8.5, 5.7, 4.2 and 2.8 nm, respectively. The BCC Fe nanopillars with

7.2 Influence of twin boundaries

7.2.1 Introduction

In recent years, the twinned nanopillars or nanowires have attracted a considerable attention in view of their superior physical properties as compared to perfect defect free nanowires. The twinned nanopillars contain a series of twin boundaries with specified spacing between the boundaries. Twin boundary possesses high symmetry and lowest interface energy among all the grain boundaries. The low energy of twin boundaries results in a number of superior properties over conventional grain boundaries. For example, the twin boundaries enhance the strength without loss of ductility [172–174], improve fracture toughness and crack resistance [175–177], and increase corrosion resistance and strain rate sensitivity [178]. Moreover, the twin boundaries possess high thermal and mechanical stability [179,180] and high electrical conductivity [181]. The superior mechanical properties of twinned nanopillars have been attributed to unique deformation mechanisms operating in the presence of twin boundaries [182]. In view of this, the materials containing high density of twin boundaries have attracted huge interest among materials scientists and engineers.

Several experimental and molecular dynamics (MD) simulation studies have been performed to understand the influence of twin boundaries on the strength and deformation behaviour in FCC nanopillars/nanowires [183–187]. Using MD simulations, Cao et al. [183] have shown that in FCC nanopillars, the twin boundaries serve as the strong obstacles for dislocations motion. As a result, the decrease in twin boundary spacing increases the yield strength in orthogonally twinned Cu nanopillars. Apart from obstacle to dislocation motion, the twin boundaries also serve as dislocation source once they lose their coherency at large plastic deformation [183]. This nature of twin boundaries as a dislocation source and also as a glide plane contributes to the improvement in tensile ductility. In addition to orthogonally twinned FCC nanopillars, the increase in yield stress is also observed in slanted and vertically twinned FCC nanopillars [186, 187]. Using MD simulations and in-situ experiments, the deformation mechanisms responsible for superior properties and the associated dislocation-twin boundary interactions have been well characterised in FCC nanopillars.

Most of the studies reported in the literature have been performed on twinned FCC nanopillars and little attention has been paid to characterise the mechanical behaviour of twinned BCC nanowires/nanopillars. Because of the different atomic densities and stacking sequence,

7.1.6 Deformation of <110> nanowire with twist boundary

The deformation behaviour of <110> BCC Fe nanowire containing twist grain boundary is shown in Figure 7.5 at 10 K. It can be seen that the yielding in the nanowire occurs by the nucleation of 1/2<111> dislocation loops from the intersection of surface and dislocation network (Figure 7.5a). The yielding by full dislocation nucleation causes a large drop in flow stress and the subsequent plastic deformation is dominated by dislocation slip (Figure 7.5b). With increasing deformation, the dislocations nucleated during the yielding interact with each other and finally move to the surface (Figure 7.5c). Unlike the <100> nanowire with a twist boundary, the <110> nanowire never becomes dislocation free and also, the twinning is not observed at any strain. These results show that the deformation by slip in <110> nanowire with a twist boundary is similar to that of perfect <110> BCC Fe nanowire (Chapter 3). Further, the presence of initial dislocations in <110> nanowire has negligible effect on the deformation behaviour.
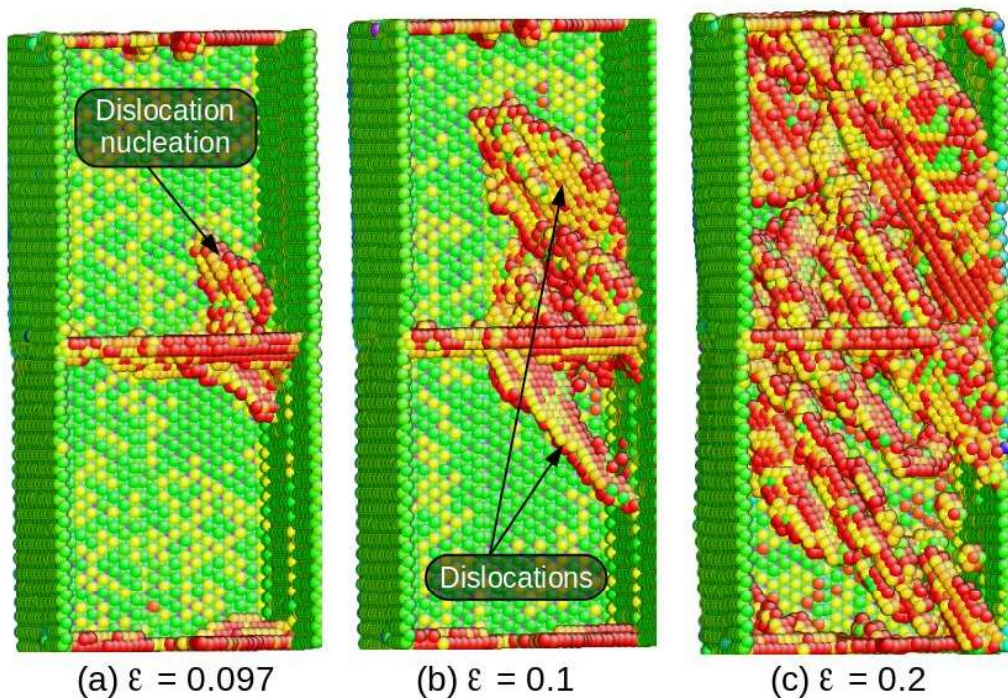
Figure 7.5: The deformation behaviour of <110> BCC Fe nanowire containing twist boundary (TWB) under tensile loading showing (a) yielding by dislocation nucleation and (b-c) subsequent plastic deformation by slip mode.

138

peak of 96.6 nm at $\varepsilon = 0.051$ (Figure 7.4b) to 37.5 nm at $\varepsilon = 0.08$ (Figure 7.4c). The continuous split and escape of dislocations leave the nanowire in a dislocation-free state (Figure 7.4d) with a few point defects. At this stage, an increase in plastic strain makes the nanowire to undergo second elastic deformation with peak stress value of 8.6 GPa followed by an abrupt drop. This abrupt drop due to the yielding of dislocation-free nanowire takes place by the nucleation of two-layer twin embryo from the slip step as shown in Figure 7.4e. With increasing plastic deformation, the two layer twin embryo becomes a full twin enclosed by two twin boundaries as shown in Figure 7.4f. This twin boundaries move away from each other (Figure 7.4g) by the repeated initiation and glide of 1/6<111> twinning partial dislocations resulting in the constant flow stress with some oscillations in the strain range 0.15-0.6 (Figure 7.3a). Due to the presence of point defects generated by the movement of 1/2<111> dislocations during initial deformation by slip mode, the twin boundary migration or twin growth process is impeded and as a result, the nanowire does not undergo full reorientation and fails by shearing along the {112} twin boundary plane (Figure 7.4h).

The above results indicate that the nanowire containing a twist boundary deforms by slip at small strains ($\varepsilon < 0.15$) followed by twinning at large strains. The simulations performed on <100> nanowire with multiple twist boundaries also indicated similar deformation behaviour. However, in this case the deformation by slip mode has extended to large strains. In Chapter 3, it has been demonstrated that the <100> BCC Fe nanowires deform by twinning mechanism at all strains. Thus, the presence of initial dislocations has dominant effect on twinning mechanism in nanowires. The deformation by slip of dislocations is preferred over twinning in the presence of dislocations or dislocation networks. Further the deformation in <100> nanowire with multiple twist boundaries suggest that increasing the dislocation density increases the contribution of slip and delays/prevents the occurrence of twinning. In qualitative agreement with present study, recently Zepeda-Ruiz et al. [171], while the probing the limits of plasticity, have shown the defect free Ta deforms purely by twinning mechanism, while the same crystal with initial dislocation loops doesn't show any twinning but deforms exclusively through the slip of dislocations. Further, it has been shown that apart from initial dislocations or initial micro-structure, temperature and strain rate also play an important role on deformation twinning in nanowires [171]. The present study also substantiates the absence of extensive deformation twinning in bulk materials, which inherently contain very high density of dislocations.
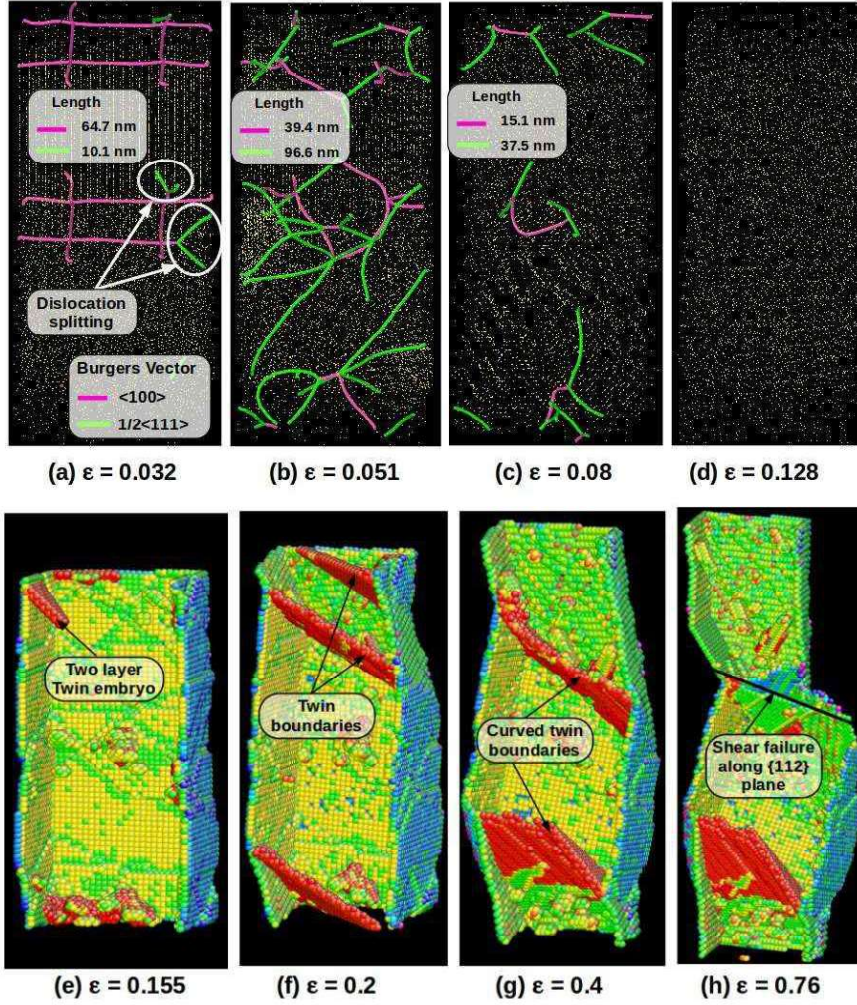
Figure 7.4: Deformation behaviour of <100> BCC Fe nanowire containing twist boundary (TWB) under tensile loading. In figures (a)-(d), only dislocations are shown using OVITO. In figures (e)-(h), the atoms are coloured according to the centro-symmetry parameter. The perfect BCC Fe atoms and surfaces are removed for clarity.

move away from the initial network (Figure 7.4b). The continuous splitting of <100> dislocations increases the total length of 1/2<111> glissile dislocations from 10.1 nm at yielding ($\varepsilon = 0.032$) to 96.6 nm at $\varepsilon = 0.051$ with corresponding decrease in the length of <100> sessile dislocations. Energetically, the splitting of <100> dislocations is difficult to be observed at low stresses due to increase in energy, i.e. $a^2 < 3a^2/4 + 3a^2/4$, where a lattice parameter. However, this dislocation reaction becomes feasible at high stresses typically in the order of GPa as observed in the present study. The continuous splitting of <100> network dislocations followed by glide of resultant dislocations and their escape to surface leads to small elastic peaks and flow stress drops at low strains in the range 0.04-0.15 (Figure 7.3a). The presence of high surface and image stresses aided by small size facilitates dislocations to escape from the nanowire. As a result, the total length of 1/2<111> glissile dislocations also decreases from a

136
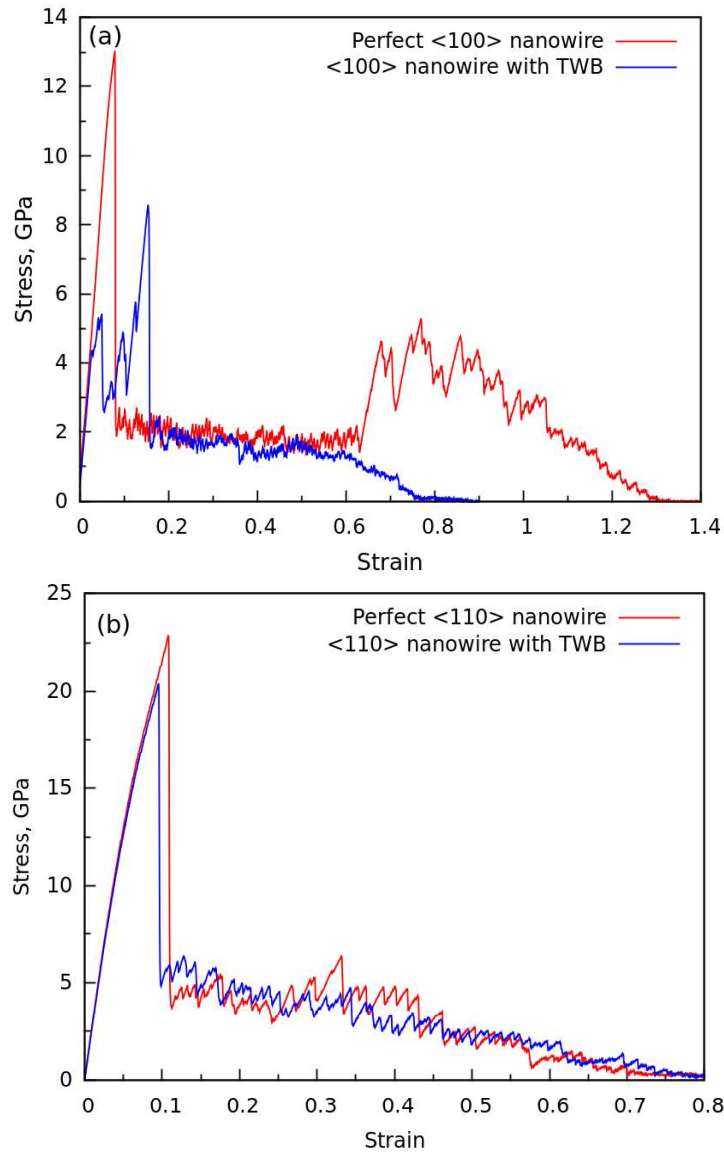
Figure 7.3: Stress-strain behaviour of (a) <100> and (b) <110> BCC Fe nanowire with and without twist boundary (TWB).

7.1.5   Deformation of <100> nanowire with twist boundary

The deformation behaviour of <100> BCC Fe nanowire with twist boundary is shown in Figure 7.4 at 10 K. During elastic deformation, no change has been observed in the structure of initial dislocation network. Following the elastic deformation, the yielding in the nanowire occurs by the splitting of <100> type screw dislocations into two 1/2<111> dislocations (Figure 7.4a). As a result, the total length of <100> dislocations decreases from 68.7 to 64.7 nm at the expense of 1/2<111> dislocations (Figure 7.4a). The splitting of sessile screw dislocations initiates from the surface of the nanowire and penetrates towards the dislocation junction. With increasing plastic strain, more and more sessile dislocations splits into glissile dislocations and

the tension at the triple nodes and the preference of 1/2<111> type segments to lie along the potential valley parallel to <111> direction [166]. Similar hexagonal structure for {110} twist grain boundaries has been reported in MD simulation studies [166, 168] and also observed experimentally using TEM by Ohr and Beshers [169]. A TEM observation made by Ohr and Beshers [169] revealed that the small angle {110} TWGBs contains a hexagonal dislocation network with three sets of dislocation segments. The burgers vector of a dislocations in a hexagonal network satisfy the relation $b_1 + b_2 = b_3$ at the junction. The dislocation networks at the TWGBs were formed as a result of mismatch strain at the interface during relaxation [170].

7.1.4 Stress-strain behaviour

The stress-strain behaviour under the tensile loading of <100> and <110> BCC Fe nanowires containing a twist boundary is shown in Figure 7.3a and 7.3b, respectively. The stress-strain behaviour of the respective perfect and defect free nanowires has been superimposed. It can be seen that both the <100> and <110> nanowires with twist boundary displayed lower yield strength as compared to their perfect nanowires, but the difference is significant in the case of <100> nanowire, while it is marginal for <110> nanowire. Following the elastic deformation, <100> nanowire yields with a corresponding flow stress drop from 5.3 GPa to 2.3 GPa (Figure 7.3a), whereas the yield drop was significant from 16.2 GPa to 4.1 GPa in <110> nanowire (Figure 7.3b). However in perfect nanowires, the yield drop was significant for both the cases. Therefore, the small yield drop of <100> nanowire with a twist boundary is different from the corresponding perfect nanowire. Following the initial yielding, the two nanowires containing a twist boundary exhibited contrasting flow behaviour during plastic deformation. The <100> nanowire having a twist boundary exhibited large flow stress fluctuations at low strains in the range 0.04 - 0.15 followed by a second elastic peak and large yield drop from 8.6 GPa to 1.7 GPa at $\varepsilon = 0.15$ (Figure 7.3a). After the second yield drop, the flow stress was constant with mean value of 1.8 GPa up to $\varepsilon = 0.50$ followed by decrease in flow stress till failure. Contrary to this, the <110> nanowire with a twist boundary exhibit continuous decreases in flow stress till failure (Figure 7.3b). Finally, the <100> nanowire with twist boundary has shown significantly lower strain to failure than the perfect nanowire, while <110> case, no significant difference in failure strain has been noticed. These results shows that the overall stress-strain behaviour of <100> nanowire with a twist boundary is different from the corresponding perfect nanowire, while it is same for <110> orientation.

randomly to all the atoms according to finite temperature Maxwell distribution and then the system is equilibrated to a temperature of 10 K in canonical ensemble (constant NVT). The velocity verlet algorithm was used to integrate the equation of motion with a time step of 5 fs. Upon completion of the equilibration process, the tensile deformation was carried out at constant engineering strain rate of 1×10^8 s^{-1} along the nanowire axis. The average stress is calculated from the Virial expression (Section 2.7). The visualisation of atomic structure is accomplished using AtomEye [102] and OVITO [103] packages.

7.1.3 Structure of twist boundaries

Figure 7.2 shows a dislocation network formed after relaxation at 10 K in <100> and <110> BCC Fe nanowires. It can be seen that the dislocation network in <100> nanowire has square structure (four fold symmetry) and contains a junctions formed by four <100> type sessile screw dislocations (b_1, b_2, b_3, b_4 in Figure 7.2a). Similar square shape structure has been reported by Hetherly et al. [167] in BCC Fe. The burger vectors of dislocations at the junction satisfy the relation $b_1 + b_2 = b_3 + b_4$. On the other hand, the dislocation network in <110> nanowire has a hexagonal structure (three fold symmetry) and contains junctions formed by two 1/2<111> glissile screw dislocations (b_1, b_2 in Figure 7.2b) and one <100> sessile screw dislocation (b_3 in Figure 7.2b). Further, the 1/2<111> dislocation segments on {110} twist grain boundary contain many kinks. These kinks arises as a result of the competition between

(a) {100} TWGB   (b) {110} TWGB
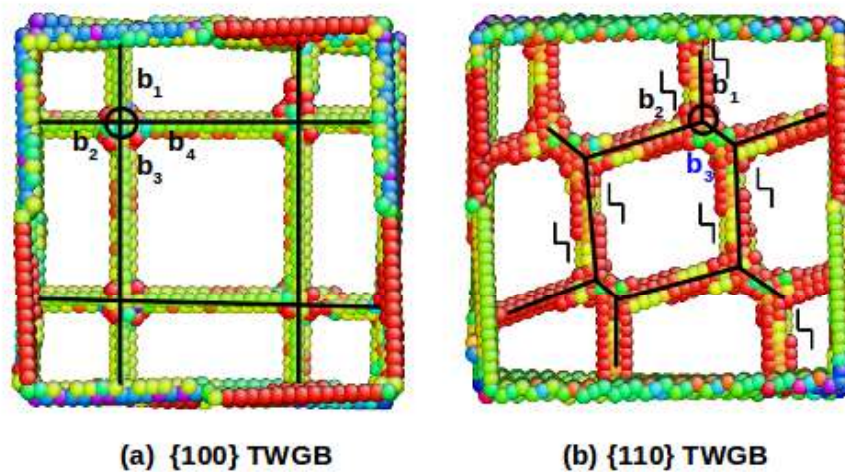
Figure 7.2: The structure of dislocations network in BCC Fe nanowires. (a) Square shape in <100> and (b) hexagonal shape in <110> nanowire. The atoms are coloured according to their centro-symmetry parameter. The perfect BCC atoms are removed for clarity and only the defect atoms are shown.

plasticity, respectively.

7.1.2   Simulation details

Molecular dynamics simulations have been carried out in LAMMPS package [94] employing EAM potential for BCC Fe given by Mendelev and co-workers [75] has been chosen to describe the interaction between Fe atoms. Initially, the single crystal BCC Fe nanowires of square cross section width (d) = 8.5 nm and consisting of about 110, 000 atoms oriented in <100> and <100> direction were considered. The length (l) was twice the cross section width (d). Following this, the nanowires were divided into two equal grains, upper and lower (Figure 7.1). In order to create a twist grain boundary (TWGB), the upper grain is rotated by an angle $+2^o$ and lower grain by -2° around the nanowire axis (Figure 7.1), i.e. <100> axis for <100> nanowire, and <110> axis for <100> nanowire. The procedure for creating the twist grain boundaries is schematically shown in Figure 7.1. The twist angle of $+2^o$ has been chosen in order to compare the structure of twist grain boundary with previous MD simulations [167, 168]. Upon relaxation, a screw dislocation network was spontaneously formed at the interface (Figure 7.1).
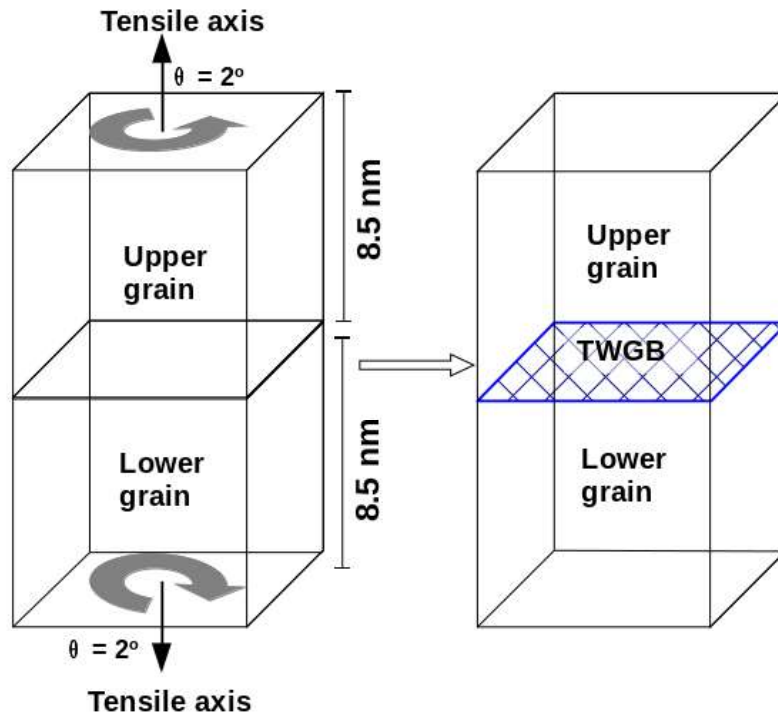
Figure 7.1: Schematic showing the creation of twist grain boundary(TWGB) in <100> and <110> BCC Fe nanowires.

Following the creation of twist grain boundary , the initial velocities were assigned

Chapter 7

Influence of twist and twin boundaries on deformation behaviour of BCC Fe nanowires

The last couple of chapters have been focussed on the deformation behaviour of perfect or defect free BCC Fe nanowires. This chapter deals with the deformation behaviour of BCC Fe nanowires following the introduction of two different types of grain boundaries, one is twist boundaries and the other is twin boundaries. The influence of single and/or multiple boundaries on the strength values and deformation mechanisms has been described.

7.1 Influence of twist boundaries

7.1.1 Introduction

In general, the plastic deformation of any material critically depends on the presence of dislocations/dislocation density. It is well known that the low angle twist boundaries consist of a network of dislocations arranged in a specific structure [166]. Therefore, investigating the deformation behaviour of nanowires consisting of low angle twist boundaries provide valuable insights into how the presence of initial dislocations influences the deformation mechanisms in nanowires. In Chapter 3, it has been shown that the <100>, <112> and <102> BCC Fe nanowires deform by twinning mechanism. However, it is not clear whether the deformation by twinning still continue to occur in the presence of initial dislocations in the nanowires. In view of this, the present study is aimed at understanding the influence of twist boundary on deformation behaviour of BCC Fe nanowires. The influence of twist boundary has been studied in two different orientations, one deforming by twinning (<100>) and the other by slip (<110>), thereby revealing the influence of initial dislocations on deformation twinning and dislocation

and $\{111\}$ as side surfaces increases initially with increasing size and then saturates at larger sizes. This has been attributed to the increase in surface energy of $<110>/\{111\}\{112\}$ nanowire. However, the surface energy of same $<110>$ oriented nanowire with $\{110\}$ and $\{100\}$ as side surfaces decreases with increasing size and this may result in different variations in yield strength as a function of size. Therefore, the variation of yield strength as a function of size in $<110>/\{110\}\{100\}$ nanowire needs to be investigated. This investigation is expected to bring out the role of side surfaces in BCC Fe nanowires.

- It has been shown that the ultra-thin BCC Fe nanowires of size below 3.23 nm undergo slip mode of deformation and exhibits the formation of pentagonal atomic chains under tensile loading. The stability of such pentagonal atomic chains needs to be verified using Ab-initio density functional theory calculations.

- In the present study, the twin boundaries have been introduced perpendicular to the loading axis i.e., transverse or orthogonal twin boundaries. The role of twin boundaries introduced parallel to the loading axis (longitudinal) is to be examined for complete understanding.

- The deformation behaviour of nanocrystalline BCC Fe at different grain sizes is another interesting area of research, where there is a need to establish a critical grain size at which the strength is maximum in nanocrystalline BCC Fe. These suggested investigation is expected to bring out the regimes of Hall-Petch and inverse Hall-Petch relations of flow stress vs. grain size. However, this study requires large computational resources particularly for large grain sizes.

Influence of twin boundaries: Molecular dynamics simulations performed on twinned BCC Fe nanopillars indicated that the twin boundaries have a contrasting role under tensile and compressive loadings (Chapter 7). Under tensile loading, the yield stress has been almost independent of twin boundary spacing, while under compressive loading, the yield stress showed strong dependence on twin boundary spacing. This contrasting behaviour in yield stress has been explained by repulsive force offered by the twin boundaries. Under tensile loading, deformation is dominated by the twinning mechanism, where the initial twin boundary offers negligible repulsive force on the nucleation of twinning partials. Due to this, the yield stress varies marginally as a function of twin boundary spacing. In addition to twinning, minor activity of full dislocations and twin-twin interactions of <021> type have been observed during tensile deformation. The observed <021> type twin intersection is in agreement with the fact that in BCC metals, there are five types of probable twin-twin intersections, namely <011>, <012>, <113>, <111>, and <135>. Further, it has been found that the edge of the curved twin boundary can acts as a dislocation source. Contrary to tensile loading, deformation under compressive loading was dominated by slip of full dislocations, where the twin boundaries offer a strong repulsive force for the nucleation of full dislocations. This repulsive force results in the strong dependence of yield stress on twin boundary spacing. The observed dislocation-twin boundary interactions revealed that the dislocation can either directly transmit without any deviation in slip plane or it can transmit on symmetrical slip plane in the neighbouring grain. These two way transmission of dislocation have been explained in terms of the similarity in the slip planes across the twin boundary in BCC system.

8.2   Future directions

Based on the understanding gained from the present work, it is suggested that there is huge

<111> BCC Fe nanowires undergo ductile-brittle transition at 400 K. Below this temperature, the nanowires yield through the nucleation of a sharp crack and fails in a brittle manner, whereas at high temperatures, the nucleation of multiple 1/2<111> dislocations associated with significant plastic deformation leads to ductile failure. This transition is also reflected in the accumulated plastic strain. The plastic strain is negligible at low temperatures (10-375 K) followed by a sharp increase in the temperature range 375-500 K. Beyond 500 K, the ductility remained nearly constant. Further, the results have shown that the nanowire size, shape and applied strain rate also influences the transition temperature. The nanowire with circular cross-section shape has shown higher transition temperature than the square cross-section nanowire. In nanowire with square cross-section, the transition temperature increases with increasing size and strain rate. It has been demonstrated that the ductile-brittle transition in <111> BCC Fe nanowires results mainly from the competition between the yield and fracture processes with respect to temperature. Below the transition temperature of 400 K, the yield and fracture stresses were nearly similar which resulted in sudden failure without yielding and significant plastic deformation. On the other hand, above the transition temperature, the yield stress was lower than the fracture stress, and thus facilitated easy yielding and significant plastic deformation before failure. It was observed that the ductile-brittle transition was absent in <100> and <110> orientations.

Influence of twist boundaries: MD simulation results indicated that the twist boundaries in BCC Fe contain a network of dislocations. Therefore, the deformation behaviour of nanowires consisting of low angle twist grain boundaries provide valuable insights into how the presence of initial dislocations influences the deformation mechanisms in nanowires. The influence twist boundary has been studied in two different orientations, one deforming by twinning i.e. <100> orientation, and the other by slip i.e. <110> orientation. The simulation results on

trasting behaviour. The Young's modulus and yield stress in <100> nanowire decreases with increasing size followed by saturation towards their respective bulk/theoretical value. On the other hand in <110> nanowire, the Young's modulus and yield strength exhibited an initial increase followed by saturation towards their respective bulk/theoretical value. The yield strength variations with respect to size in <100> BCC Fe nanowires has been explained based on the presence of initial residual stress and the variations in the number of defect nucleation sites with increasing size. Similarly, the variations in surface energy were found to be responsible for the yield strength variations in <110> nanowire.

Influence of size and temperature on twinning: In order to understand the combined influence of size and temperature, extensive MD simulations have been carried out on ultra-thin <100> BCC Fe nanowires of different sizes and temperatures. The results indicated that BCC Fe nanowires with cross-section width less than 3.23 nm deform by twinning mechanisms at low temperatures, while dislocation slip dominated the deformation behaviour at high temperatures. The temperature at which the nanowires show twinning to slip transition, increases with increasing size, and above 3.23 nm, deformation twinning prevailed at all temperatures. These observations suggests that depending on the temperature, there is a size limit below which the twinning does not occur in BCC Fe nanowires. The observed twinning to slip transition has been attributed to the coordinated nature of twinning phenomenon, which may get disturbed at small sizes and high temperatures. The different modes of deformation are also reflected in respective stress-strain behaviour of the nanowires. Interestingly, when the nanowire deform by dislocation slip mechanism, the formation of pentagonal atomic chains have been observed in the necking region of nanowires. In nanowires with d = 0.404 and 0.807 nm, complete transformation to pentagonal structures has been observed at relatively higher temperatures. The formation of pentagonal atomic chains have not been observed in nanowires that deform by

under compressive loading. A good agreement between the deformation twinning in BCC Fe nanowires and those reported experimentally for the bulk single crystal counterparts was obtained. The <100> and <110> oriented nanowires displayed opposite tension-compression asymmetry in deformation mechanisms. The <100> nanowire deform by twinning under tensile loading, while slip is observed under the compressive loading. On the contrary, <110> nanowire deform by slip under tensile loading, while twinning is observed under compressive loading. The orientation dependent deformation behaviour and the opposite tension-compression asymmetry in BCC Fe nanowires has been explained based on the twinning-antitwinning asymmetry of 1/6<111> partial dislocations on {112} planes.

Size effects: The influence of nanowire size on the deformation behaviour under tensile loading has been investigated on two different orientations, one deform by twinning i.e. <100>, and the other by slip i.e. <110> orientation. These two orientations were chosen mainly to reveal the influence of size on deformation twinning and dislocation plasticity in BCC Fe nanowires. The investigations on <100> BCC Fe nanowires indicated the presence of two different behaviours as a function of size. The small size nanowires up to d = 11.42 nm deform by twinning at low strains (i.e. for $\varepsilon < 0.6$) followed by reorientation due to the activation of only single twin system. Following the reorientation, the deformation mode shifts from twinning to slip at higher strains and this results in high ductility more than 100% and failure by necking. On the other hand, the large size nanowires beyond d = 11.42 nm, deforms by twinning on multiple twin systems, which disrupts the reorientation process. The twin-twin interaction leads to crack nucleation and failure by cleavage resulting in lower ductility in large size nanowires. It has been revealed that the twin growth occurs by the repeated initiation and glide of 1/6<111> twinning partial dislocations along the adjacent {112} planes. The variations in twin propagation stress indicated that twin growth is easier in large size nanowires as compared to that in small size

Chapter 8

Conclusions and future directions

8.1 Conclusions

Detailed molecular dynamics simulations have been performed to examine the influence of orientation, nanowire size, cross-section shape, mode of loading (tension/compression) and temperature on the deformation and failure behaviour of BCC Fe nanowires. In addition, the influence of twist and twin boundaries on the deformation mechanisms of BCC Fe nanopillars has been investigated. The important findings of the present study are described in the following:

Influence of orientation and mode of loading: Molecular dynamics simulations performed on BCC Fe nanowires with five different orientations revealed that the operative deformation mechanisms depends strongly on the crystallographic orientation and mode of loading i.e. tension/compression. Under tensile loading, the <100>, <112> and <102> oriented nanowires yield by the nucleation of twin embryos followed by subsequent plastic deformation domi-

[190] M. Mrovec, C. Elsasser, and P. Gumbsch, Interactions between lattice dislocations and twin boundaries in tungsten: A comparative atomistic simulation study, Philos. Mag. 89 (2009) 3179-3194. https://doi.org/10.1080/14786430903246346.

[191] A. Ojha, H. Sehitoglua, L. Patriarca, and H.J. Maier, Twin migration in Fe-based bcc crystals: Theory and experiments, Philos. Mag. 94 (2014) 1816-1840. https://doi.org/10.1080/14786435.2014.898123.

[192] L. Wang, F. Zhao, F.P. Zhao, Y. Cai, Q. An, and S.N. Luo, Grain boundary orientation effects on deformation of Ta bicrystal nanopillars under high strain-rate compression, J. Appl. Phys. 115 (2014) 053528. https://doi.org/10.1063/1.4864427.

[193] Y. Zhu, Z. Li, M. Huang, and Y. Liu, Strengthening mechanisms of the nanolayered polycrystalline metallic multilayers assisted by twins, Int. J. Plast. 72 (2015) 168-184. https://doi.org/10.1016/j.ijplas.2015.05.014.

[194] S. Mahajan, Accommodation at deformation twins in bcc crystals, Metall. Trans. A 12 (1981) 379-386. https://doi.org/10.1007/BF02648535.

[195] D. Hull, The initiation of slip at the tip of a deformation twin in α-iron, Acta Metall. 9 (1961) 909-911.https://doi.org/10.1016/0001-6160(61)90204-8.

[196] Z. You, X. Li, L. Gui, Q. Lu, T. Zhu, H. Gao, and L. Lu, Plastic anisotropy and associated deformation mechanisms in nanotwinned metals, Acta Mater. 61 (2013) 217-227. https://doi.org/10.1016/j.actamat.2012.09.052.

[177] L. Liu, J. Wang, S.K. Gong, and S.X. Mao, Atomistic observation of a crack tip approaching coherent twin boundaries, Sci. Rep. 4 (2014) 4397. https://doi.org/10.1038/srep04397.

[178] C. Deng and F. Sansoz, Effects of twin and surface facet on strain-rate sensitivity of gold nanowires at different temperatures, Phys. Rev. B 81 (2010) 155430. https://doi.org/10.1103/PhysRevB.81.155430.

[179] O. Anderoglu, A. Misra, H. Wang, and X. Zhang, Thermal stability of sputtered Cu films with nanoscale growth twins, J. Appl. Phys. 103 (2008) 094322. https://doi.org/10.1063/1.2913322.

[180] J. Wang, N. Li, and A. Misra, Structure and stability of Σ3 grain boundaries in face centered cubic metals, Philos. Mag. 93 (2012) 315-327. https://doi.org/10.1080/14786435.2012.716908.

[181] L. Lu, Y. Shen, X. Chen, L. Qian, and K. Lu, Ultrahigh strength and high electrical conductivity in copper, Science 304 (2004) 422-426. https://doi.org/10.1126/science.1092905.

[182] T. Zhu and H. Gao, Plastic deformation mechanism in nanotwinned metals: An insight from molecular dynamics and mechanistic modeling, Scr. Mater. 66 (2012) 843-848. https://doi.org/10.1016/j.scriptamat.2012.01.031.

[183] A.J. Cao, Y.G. Wei, and S.X. Mao, Deformation mechanisms of face-centered-cubic metal nanowires with twin boundaries, Appl. Phys. Lett. 90 (2007) 151909. https://doi.org/10.1063/1.2721367.

[184] Y. Zhang and H. Huang, Do twin boundaries always strengthen metal nanowires?, Nanoscale Res. Lett. 4 (2009) 34-38. https://doi.org/10.1007/s11671-008-9198-1.

[185] F. Hammami and Y. Kulkarni, Size effects in twinned nanopillars, J. Appl. Phys. 116 (2014) 033512. https://doi.org/10.1063/1.4890541.

[186] Y. Wei, Anisotropic size effect in strength in coherent nanowires with tilted twins, Phys. Rev. B 84 (2011) 014107. https://doi.org/10.1103/PhysRevB.84.014107.

[165] T.L. Johnston, G. Davies, and N.S. Stoloff, Slip character and the ductile to brittle transition of single-phase solids, Philos. Mag. 12 (1965) 305-317. https://doi.org/10.1080/14786436508218873.

[166] J.B. Yang, Y. Nagai, M. Hasegawa, and Y.N. Osetsky, Atomic scale modeling of {110} twist grain boundaries in α-iron: Structure and energy properties, Phil. Mag. 90 (2010) 991-1000. https://doi.org/10.1080/14786430903154086.

[167] J. Hetherly, E. Martinez, M. Nastasi, and A. Caro, Helium bubble growth at BCC twist grain boundaries, J. Nucl. Mater. 419 (2011) 201-207. https://doi.org/10.1016/j.jnucmat.2011.08.009.

[168] N. Naveen Kumar, E. Martinez, B.K. Dutta, G.K. Dey, and A. Caro, Nodal effects in α-iron dislocation mobility in the presence of helium bubbles, Phys. Rev. B 87 (2013) 054106. https://doi.org/10.1103/PhysRevB.87.054106.

[169] S.M. Ohr and D.N. Beshers, Crystallography of dislocation networks in annealed iron, Phil.Mag. 8 (1963) 1343-60. https://doi.org/10.1080/14786436308207298.

[170] A.M. Andrews, R. Lesar, M.A. Kerner, J.S. Speck, A.E. Romanov, A.L. Kolesnikova, M. Bobeth, and W. Pompe, Modeling crosshatch surface morphology in growing mismatched layers. Part II: periodic boundary conditions and dislocation groups, J. Appl. Phys. 95 (2004) 6032-6047. https://doi.org/10.1063/1.1707208.

[171] L.A. Zepeda-Ruiz, A. Stukowski, T. Oppelstrup, and V.V. Bulatov, Probing the limits of metal plasticity with molecular dynamics simulations, Nature 550 (2017) 492-495. https://doi.org/10.1038/nature23472.

[172] L. Lu, X. Chen, X. Huang, and K. Lu, Revealing the maximum strength in nanotwinned copper, Science 323 (2009) 607-610. https://doi.org/10.1126/science.1167641.

[173] X. Li, Y. Wei, L. Lu, L. Lu, and H. Gao, Dislocation nucleation governed softening and maximum strength in nano-twinned metals, Nature 464 (2010) 877-880. https://doi.org/10.1038/nature08929.

[153] Z. Wang, X. Zu, F. Gao, and W. J. Weber, Atomistic simulation of brittle to ductile transition in GaN nanotubes, Appl. Phys. Lett. 89 (2006) 243123. https://doi.org/10.1063/1.2405879.

[154] Z. Yuan, K. Nomura, and A. Nakano, Core/shell structural transformation and brittle-to-ductile transition in nanowires, Appl. Phys. Lett. 100 (2012) 153116. https://doi.org/10.1063/1.3703303.

[155] F. A. El Nabi, J. Godet, S. Brochard, and L. Pizzagalli, Onset of ductility and brittleness in silicon nanowires mediated by dislocation nucleation, Modell. Simul. Mater. Sci. Eng. 23 (2015) 025010. https://doi.org/10.1088/0965-0393/23/2/025010.

[156] R. Ramachandramoorthy, W. Gao, R. Bernal, and H. Espinosa, High strain rate tensile testing of silver nanowires: rate-dependent brittle-to-ductile transition, Nano Lett. 16 (2016) 255-263. https://doi.org/10.1021/acs.nanolett.5b03630.

[157] E. Rabkin, H.S. Nam, and D. J. Srolovitz, Atomistic simulation of the deformation of gold nanopillars, Acta Mater. 55 (2017) 2085-2099. https://doi.org/10.1016/j.actamat.2006.10.058.

[158] D.J. Quesnel, A. Sato, and M. Meshii, Solution softening and hardening in the iron-carbon system, Mater. Sci. Eng. 18 (1975) 199-208. https://doi.org/10.1016/0025-5416(75)90170-6.

[159] J. Diehl, M. Schreiner, S. Staiger, and S. Zwiesele, On the characteristic features of solution softening and hardening in B.C.C. metals, Scr. Metall. 10 (1976) 949-953. https://doi.org/10.1016/0036-9748(76)90220-9.

[160] D. Tseng and K. Tangri, Temperature and strain rate sensitivities of flow stress for the high purity AISI iron, Scr. Metall. 11 (1977) 719-723. https://doi.org/10.1016/0036-9748(77)90147-8.

[161] E. Kuramoto, Y. Aono, and K. Kitajima, Thermally activated slip deformation of high purity iron single crystals between 4.2 K and 300 K, Scr. Metall. 13 (1979) 1039-1042.

[140] F. Sato, A.S. Moreira, J. Bettini, P.Z. Coura, S.O. Dantas, D. Ugarte, and D.S. Galvao, Transmission electron microscopy and molecular dynamics study of the formation of suspended copper linear atomic chains, Phys. Rev. B 74 (2006) 193401. https://doi.org/10.1103/PhysRevB.74.193401. https://doi.org/10.1103/PhysRevLett.83.3884.

[141] D. Sanchez-Portal, E. Artacho, J. Junquera, P. Ordejon, A. Garcia, and J.M. Soler, Stiff monatomic gold wires with a spinning zigzag geometry, Phys. Rev. Lett. 83 (1999) 3884-87. https://doi.org/10.1103/PhysRevLett.83.3884.

[142] P. Sen, O. Gulseren, T. Yildirim, I.P. Batra, and S. Ciraci, Pentagonal nanowires : A first-principles study of the atomic and electronic structure, Phys. Rev. B 65 (2002) 235433. https://doi.org/10.1103/PhysRevB.65.235433.

[143] X. L. Wu and Y.T. Zhu, Inverse grain-size effect on twinning in nanocrystalline Ni, Phys, Rev. Lett. 101 (2008) 025503. https://doi.org/10.1103/PhysRevLett.101.025503.

[144] V.K. Sutrakar and D.R. Mahapatra, Formation of stable ultra-thin pentagon Cu nanowires under high strain rate loading, J. Phys. Condens. Matter. 20 (2008) 335206. https://doi.org/10.1088/0953-8984/20/33/335206.

[145] P. Garcia-Mochales, S. Pelaez, P.A. Serena, C. Guerrero, and R. Paredes, On the optimal conditions for the formation and observation of long icosahedral nanowires of aluminium, nickel and copper, Modell. Simul. Mater. Sci. Eng. 21 (2013) 045002. https://doi.org/10.1088/0965-0393/21/4/045002.

[146] P. Garcia-Mochales, R. Paredes, S. Pelaez, and P.A. Serena, The formation of pentagonal Ni nanowires: dependence on the stretching direction and the temperature, Phys. Stat. Sol. 205 (2008) 1317-1323. https://doi.org/10.1002/pssa.200778170.

[147] H.S. Park and J.A. Zimmerman, Modeling inelasticity and failure in gold nanowires, Phys. Rev. B 72 (2005) 054106. https://doi.org/10.1103/PhysRevB.72.054106.

[148] A. Takahashi, S. Kurokawa, and A. Sakai, Molecular dynamics simulation of the break of magnesium nanowires, Phys. Stat. Sol. B, 251 (2014) 1363-1371. https://doi.org/10.1002/pssb.201350245.

[149] N. Fujita, S. Kurokawa, and A. Sakai, Formation of icosahedral nanowires, Phys. Stat.

[129] C.R. Weinberger, A.T. Jennings, K. Kang, and J.R. Greer, Atomistic simulations and continuum modeling of dislocation nucleation and strength in gold nanowires, J. Mech. Phys. Solids 60 (2012) 84-103. https://doi.org/10.1016/j.jmps.2011.09.010

[130] S. Kotrechko, A. Timoshevskii, I. Mikhailovskij, T. Mazilova, N. Stetsenko, O. Ovsajannikov, and V. Lidych, Atomic mechanisms governing upper limit on the strength of nanosized crystals, Eng. Fract. Mech. 150 (2015) 184-196. https://doi.org/10.1016/j.engfracmech.2015.03.025.

[131] R. Groger and V. Vitek, Explanation of the discrepancy between the measured and atomistically calculated yield stresses in body-centred cubic metals, Philos. Mag. Lett. 87 (2007) 113-120. https://doi.org/10.1080/09500830601158781.

[132] A.S. Schneider, C.P. Frick, B.G. Clark, P.A. Gruber, and E. Arzt, Influence of orientation on the size effect in bcc pillars with different critical temperatures, Mater. Sci. Eng. A 528 (2011) 1540-1547. https://doi.org/10.1016/j.msea.2010.10.073.

[133] J. Marian and J. Knap, Breakdown of self-similar hardening behavior in Au nanopillar microplasticity, Int. J. Multiscale Comp. Eng. 5 (2007) 287-294. 10.1615/IntJMultCompEng.v5.i3-4.100.

[134] Y. Gan and J.K. Chen, Molecular dynamics study of size, temperature and strain rate effects on mechanical properties of gold nanofilms, Appl. Phys. A 95 (2009) 357-362. https://doi.org/10.1007/s00339-008-4970-8.

[135] J. Ren, Q. Sun, L. Xiao, X. Ding, and J. Sun, Size-dependent of compression yield strength and deformation mechanism in titanium single-crystal nanopillars oriented [0001] and [11$\bar{2}$0], Mater. Sci. Eng. A 615 (2014) 22-28. https://doi.org/10.1016/j.msea.2014.07.065.

[136] C. Zhang, Y. Yao, and S. Chen, Size-dependent surface energy density of typically fcc metallic nanomaterials, Comp. Mat. Sci 82 (2014) 372-377. https://doi.org/10.1016/j.commatsci.2013.10.015.

[116] J.W. Christian and S. Mahajan, Deformation twinning, Prog. Mater. Sci. 39 (1995) 1-157. https://doi.org/10.1016/0079-6425(94)00007-7.

[117] P.T. Olsson, S. Melin, and C. Persson, Atomistic simulations of tensile and bending properties of single crystal bcc iron nanobeams, Phy. Rev. B 76 (2007) 224112. https://doi.org/10.1103/PhysRevB.76.224112.

[118] D.M. Clatterbuck, D.C. Chrzan, and J.W. Morris Jr., The ideal strength of iron in tension and shear, Acta Mater. 51 (2003) 2271-2283. https://doi.org/10.1016/S1359-6454(03)00033-8.

[119] K. Gall, J. Diao, and M.L. Dunn, The strength of gold nanowires, Nano Lett. 4 (2004) 2431-2436. https://doi.org/10.1021/nl048456s.

[120] C.N. Reid, A review of mechanical twinning in body-centred cubic metals and its relation to brittle fracture, J. Less Common Met. 9 (1965) 105-122. https://doi.org/10.1016/0022-5088(65)90088-3.

[121] W.D. Biggs and P.L. Prati, The deformation and fracture of alpha-iron at low temperatures, Acta Metall. 6 (1958) 694-703. https://doi.org/10.1016/0001-6160(58)90060-9.

[122] J.H. Seo, H.S. Park, Y. Yoo, T.Y. Seong, J. Li, J.P. Ahn, B. Kim, and I.S. Choi, Origin of size dependency in coherent-twin-propagation-mediated tensile deformation of noble metal nanowires, Nano Lett. 13 (2013) 5112-5116. https://doi.org/10.1021/nl402282n.

[123] L. Patriarca, W. Abuzaid, H. Sehitoglu, H.J. Maier, and Y. Chumlyakov, Twin nucleation and migration in FeCr single crystals, Mater. Charact. 75 (2013) 165-175. https://doi.org/10.1016/j.matchar.2012.11.001.

[124] R.C. Cammarata, Surface and interface stress effects in thin films, Prog. Surf. Sci. 46 (1994) 1-38. https://doi.org/10.1016/0079-6816(94)90005-1.

[125] J. Diao, K. Gall, M.L. Dunn, and J.A. Zimmerman, Atomistic simulations of the yielding of gold nanowires, Acta Mater. 54 (2006) 643-653. https://doi.org/10.1016/j.actamat.2005.10.008.

[103] A. Stukowski, Visualization and analysis of atomistic simulation data with OVITO-The Open Visualization Tool, Modell. Simul. Mater. Sci. Eng. 18 (2009) 015012. https://doi.org/10.1088/0965-0393/18/1/015012.

[104] A. Stukowski and K. Albe, Dislocation detection algorithm for atomistic simulations, Modell. Simul. Mater. Sci. Eng. 18 (2010) 025016. https://doi.org/10.1088/0965-0393/18/2/025016.

[105] H.W. Paxton, Experimental verification of the twin system in alpha-iron, Acta Metall. 1 (1953) 141-143. https://doi.org/10.1016/0001-6160(53)90052-2.

[106] J. Harding, The yield and fracture behaviour of high purity iron single crystals at high rates of strain, Proc. Roy. Soc. Lond. A 299 (1967) 464-490. https://doi.org/10.1098/rspa.1967.0150.

[107] M. Friak, M. Sob, and V. Vitek, Ab initio calculation of tensile strength in iron, Philos. Mag. 83 (2003) 3529-3537. https://doi.org/10.1080/14786430310001605588.

[108] D.L. Chen and T.C. Chen, Mechanical properties of Au nanowires under uniaxial tension with high strain-rate by molecular dynamics, Nanotech. 16 (2005) 2972-2981. https://doi.org/10.1088/0957-4484/16/12/041.

[109] J. Wang, W. Hu, X. Li, S. Xiao, and H. Deng, Strain-driven phase transition of molybdenum nanowire under uniaxial tensile strain, Comput. Mater. Sci. 50 (2010) 373-377. https://doi.org/10.1016/j.commatsci.2010.08.029.

[110] S.K.R.S. Sankaranarayanan, V.R. Bhethanabotla, and B. Joseph, Molecular dynamics simulation of temperature and strain rate effects on the elastic properties of bimetallic Pd-Pt nanowires, Phys. Rev. B 76 (2007) 134117. https://doi.org/10.1103/PhysRevB.76.134117.

[111] D. Kaufmann, R. Monig, C.A. Volkert, and O. Kraft, Size dependent mechanical behaviour of tantalum, Int. J. Plast. 27 (2011) 470-478. https://doi.org/10.1016/j.ijplas.2010.08.008.

[112] H.S. Park, K. Gall, and J.A. Zimmerman, Deformation of FCC nanowires by twinning

[88] J. Niskanen and H. Henschel, Lecture notes on molecular dynamics simulations, University of Helsinki, 2003, http://www.courses.physics.helsinki.fi/fys/moldyn/.

[89] S. Nose, A unified formulation of the constant temperature molecular dynamics methods, J. Chem. Phys. 81 (1984) 511-519. https://doi.org/10.1063/1.447334.

[90] S. Nose, A molecular dynamics method for simulation in the canonical ensemble, Mol. Phys. 52 (1984) 225-268. https://doi.org/10.1080/00268978400101201.

[91] W.G. Hoover, Canonical dynamics: Equilibrium phase-space distributions, Phys. Rev. A 31 (1985) 1695-1697. https://doi.org/10.1103/PhysRevA.31.1695.

[92] H.J.C. Berendsen, J.P.M. Postma, W.F. van Gunsteren, A. DiNola, and J.R. Haak, Molecular dynamics with coupling to an external bath, J. Chem. Phys. 81 (1984) 3684-3690. https://doi.org/10.1063/1.448118.

[93] M.P. Allen, Introduction to molecular dynamics simulation, Computational soft matter: from synthetic polymers to proteins 23 (2004) 1-28.

[94] S.J. Plimpton, Fast Parallel Algorithms for short-range molecular dynamics, J. Comput. Phys. 117 (1995) 1-19. https://doi.org/10.1006/jcph.1995.1039.

[95] P. Hirel, Atomsk: A tool for manipulating and converting atomic data files, Comput. Phys. Comm. 197 (2015) 212-219. https://doi.org/10.1016/j.cpc.2015.07.012.

[96] K. S. Cheung and S. Yip, Atomic-level stress in an inhomogeneous system, J. Appl. Phys. 70 (1991) 5688-5690. https://doi.org/10.1063/1.350186.

[97] M. Zhou, A new look at the atomic level virial stress: on continuum-molecular system equivalence, Proc. R. Soc. London, A 459 (2003) 2347-2392. https://doi.org/10.1098/rspa.2003.1127.

[98] D. Faken and H. Jonsson, Systematic analysis of local atomic structure combined with 3D computer graphics, Comput. Mater. Sci. 2 (1994) 279-86. https://doi.org/10.1016/0927-0256(94)90109-0.

[99] N. Lummen and T. Kraska, Common neighbour analysis for binary atomic systems,

[75] M.I. Mendelev, S. Han, D.J. Srolovitz, G.J. Ackland, D.Y. sun, and M. Asta, Development of new interatomic potentials appropriate for crystalline and liquid iron, Philos. Mag. 83 (2003) 3977-3994. https://doi.org/10.1080/14786430310001613264.

[76] M.I. Mendelev and Y. Mishin, Molecular dynamics study of self-diffusion in bcc Fe, Phys. Rev. B 80 (2009) 144111. https://doi.org/10.1103/PhysRevB.80.144111.

[77] Y. Abe, Application of hyper-molecular dynamics to self-interstitial diffusion in α-iron, Comput. Mater. Sci. 74 (2013) 23-26. https://doi.org/10.1016/j.commatsci.2013.03.013.

[78] P.A. Gordon, T. Neeraj, Y. Li, and J. Li, Screw dislocation mobility in BCC metals: the role of the compact core on double-kink nucleation, Modelling Simul. Mater. Sci. Eng. 18 (2010) 085008. http://dx.doi.org/10.1088/0965-0393/18/8/085008.

[79] S. Queyreau, J. Marian, M.R. Gilbert, and B.D. Wirth, Edge dislocation mobilities in bcc Fe obtained by molecular dynamics, Phy. Rev. B 84 (2011) 064106. https://doi.org/10.1103/PhysRevB.84.064106.

[80] C. Domain and G. Monnet, Simulation of Screw Dislocation Motion in Iron by Molecular Dynamics Simulations, Phys. Rev. Lett. 95 (2005) 215506. https://doi.org/10.1103/PhysRevLett.95.215506.

[81] J. Chaussidon, M. Fivel, and D. Rodney, The glide of screw dislocations in bcc Fe: Atomistic static and dynamic simulations, Acta Mater. 54 (2006) 3407-3416. https://doi.org/10.1016/j.actamat.2006.03.044.

[82] S.L. Frederiksen and K.W. Jacobsen, Density functional theory studies of screw dislocation core structures in bcc metals, Philos. Mag. 83 (2003) 365-375. https://doi.org/10.1080/0141861021000034568.

[83] P. Blonski and A. Kiejna, Structural, electronic, and magnetic properties of bcc iron surfaces, Surf. Sci. 601 (2007) 123-133. https://doi.org/10.1016/j.susc.2006.09.013.

[84] W.R. Tyson and W.A. Miller, Surface free energies of solid metals : estimation from liquid surface tension measurements, Surf. Sci. 62 (1977) 267-276. https://doi.org/10.

[63] J. Wang, Z. Zeng, C.R. Weinberger, Z. Zhang, T. Zhu, and S.X. Mao, In situ atomic-scale observation of twinning dominated deformation in nanoscale body-centred cubic tungsten, Nat. Mater. 14 (2015) 594-600. https://doi.org/10.1038/nmat4228.

[64] A.B. Hagen, B.D. Snartland, and C. Thaulow, Temperature and orientation effects on the deformation mechanisms of α-Fe micropillars, Acta Mater. 129 (2017) 398-407. https://doi.org/10.1016/j.actamat.2017.03.006.

[65] S. Kotrechko and A. Ovsjannikov, Temperature dependence of the yield stress of metallic nanosized crystals, Philos. Mag. 89 (2009) 3049-3058. https://doi.org/10.1080/14786430903179554.

[66] W. Kang, M. Merrilla, and J.M. Wheeler, In-situ thermo-mechanical testing methods for micro/nano-scale materials, Nanoscale 9 (2017) 2666-2688. https://doi.org/10.1039/C6NR07330A

[67] R. Balasubramaniam, Callister'S Materials Science And Engineering: Indian Adaptation, John Wiley & Sons, 2009.

[68] M.P. Allen and D.J. Tildesley, Computer Simulation of Liquids. Oxford University Press, 1987.

[69] M.S. Daw and M.I. Baskes, Embedded-atom method: Derivation and application to impurities, surfaces, and other defects in metals, Phys. Rev. B, 29 (1984) 6443-6453. https://doi.org/10.1103/PhysRevB.29.6443.

[70] M.W. Finnis and J.E. Sinclair, A simple empirical N-body potential for transition metals, Philosophical Magazine A, 50 (1984) 45-55. https://doi.org/10.1080/01418618408244210.

[71] G. Simonelli, R. Pasianot, and E. Savino, Embedded-atom-method inter-atomic potentials for bcc-iron, Mater. Res. Soc. Symp. Proc. 291 (1993) 567-572. https://doi.org/10.1557/PROC-291-567.

[72] H. Chamati, N.I. Papanicolaou, Y. Mishin, and D.A. Papaconstantopoulos, Embedded-

[50] H. Xie, F. Yin, T. Yu, G. Lu, and Y. Zhang, A new strain-rate-induced deformation mechanism of Cu nanowire: Transition from dislocation nucleation to phase transformation, Acta Mater. 85 (2015) 191-198. https://doi.org/10.1016/j.actamat.2014.11.017.

[51] A.S.J. Koh and H.P. Lee, Shock-induced localized amorphization in metallic nanorods with strain-rate-dependent characteristics, Nano Lett. 6 (2006) 2260-2267. https://doi.org/10.1021/nl061640o.

[52] C.R. Weinberger and W. Cai, Surface controlled dislocation multiplication in metal micropillars, Proc. Nat. Acad. Sci. (PNAS), USA, 105 (2008) 14304 -14307. https://doi.org/10.1073/pnas.0806118105.

[53] S.W. Lee, Y.T. Cheng, I. Ryu, and J.R. Greer, Cold-temperature deformation of nano-sized tungsten and niobium as revealed by in-situ nano-mechanical experiments, Sci. China Technol. Sci. 57 (2014) 652-662. https://doi.org/10.1007/s11431-014-5502-8.

[54] A. Dutta, M. Bhattacharya, P. Barat, P. Mukherjee, N. Gayathri, and G. C. Das, Lattice resistance to dislocation motion at the nanoscale, Phys. Rev. Lett. 101 (2008) 115506. https://doi.org/10.1103/PhysRevLett.101.115506.

[55] J. Marian, W. Cai, and V.V. Bulatov, Dynamic transitions from smooth to rough to twinning in dislocation motion, Nature 3 (2004) 158-163. https://doi.org/10.1038/nmat1072.

[56] A. Dutta, Compressive deformation of Fe nanopillar at high strain rate: Modalities of dislocation dynamics, Acta Mater. 125 (2017) 219-230. https://doi.org/10.1016/j.actamat.2016.11.062.

[57] S.A. Kotrechko, A.V. Filatov, and A.V. Ovsjannikov, Molecular dynamics simulation of deformation and failure of nanocrystals of bcc metals, Theor. Appl. Fract. Mech. 45 (2006) 92-99. https://doi.org/10.1016/j.tafmec.2006.02.002.

[58] R.A. Johnson, Interstitials and vacancies in $alpha$-iron, Phys. Rev. A 134 (1964) 1329-1336. https://doi.org/10.1103/PhysRev.134.A1329.

[59] P. Wang, W. Chou, A. Nie, Y. Huang, H. Yao, and H. Wang, Molecular dynamics simulation on deformation mechanisms in body-centered-cubic molybdenum nanowires, J.

[38] C. Gerard and L. Pizzagalli, Mechanical behaviour of nanoparticles: Elasticity and plastic deformation mechanisms, Pramana - J. Phys. 84 (2015) 1041-1048. https://doi.org/10.1007/s12043-015-0998-4.

[39] V.K. Sutrakar, D.R. Mahapatra, and A.C.R. Pillai, Temperature-pressure induced solid-solid <100> to <110> reorientation in FCC metallic nanowire: a molecular dynamic study, J. Phys.: Condens. Matter 24 (2012) 015401. https://doi.org/10.1088/0953-8984/24/1/015401

[40] H.S. Park, K. Gall, and J.A. Zimmerman, Shape memory and pseudo-elasticity in metal nanowires, Phys. Rev. Lett. 95 (2005) 255504. https://doi.org/10.1103/PhysRevLett.95.255504.

[41] V.K. Sutrakar and D.R. Mahapatra, Coupled effect of size, strain rate, and temperature on the shape memory of a pentagonal Cu nanowire, Nanotech. 20 (2009) 045701. https://doi.org/10.1088/0957-4484/20/4/045701.

[42] J.C. Gonzalez, v. Rodrigues, J. Bettini, L.G.C. Rego, A.R. Rocha, P.Z. Coura, S.O. Dantas, F. Sato, D.S. Galvao, and D. Ugarte, Indication of unusual pentagonal structures in atomic-size Cu nanowires, Phys. Rev. Lett. 93 (2004) 126103. https://doi.org/10.1103/PhysRevLett.93.126103.

[43] O. Gulseren, F. Ercolessi, and E. Tosatti, Noncrystalline structures of ultrathin unsupported nanowires, Phys. Rev. Lett. 80 (1998) 3775-78. https://doi.org/10.1103/PhysRevLett.80.3775.

[44] H.S. Park and J.A. Zimmerman, Stable nanobridge formation in <110> gold nanowires under tensile deformation, Scr. Mater. 54 (2006) 1127-1132. https://doi.org/10.1016/j.scriptamat.2005.11.064.

[45] Y. Kondo and K. Takayanagi, Synthesis and characterization of helical multi-shell gold nanowires, Science 289 (2000) 606-608. https://doi.org/10.1126/science.289.5479.606.

[46] G. Richter, K. Hillerich, D.S. Gianola, R. Monig, O. Kraft, and C.A. Volkert, Ultrahigh strength single crystalline nanowhiskers grown by physical vapor deposition, Nano Lett.

[26] S. Xu, Y.F. Guo, and A.H.W. Ngan, A molecular dynamics study on the orientation, size, and dislocation confinement effects on the plastic deformation of Al nanopillars, Inter. J. Plast. 43 (2013) 116-127. https://doi.org/10.1016/j.ijplas.2012.11.002.

[27] S. Lee, J. Im, Y. Yoo, E. Bitzek, D. Kiener, G. Richter, B. Kim, and S.H. Oh, Reversible cyclic deformation mechanism of gold nanowires by twinning-detwinning transition evidenced from in situ TEM, Nature comm. 5 (2014) 3033. https://doi.org/10.1038/ncomms4033.

[28] A. Cao and E. Ma, Sample shape and temperature strongly influence the yield strength of metallic nanopillars, Acta Mater. 56 (2008) 4816-4828. https://doi.org/10.1016/j.actamat.2008.05.044.

[29] P. Rohith, G. Sainath, and B. K. Choudhary, Double reorientation in <110> Cu nanowires, Phil. Mag. Lett. 97 (2017) 408-416. https://doi.org/10.1080/09500839.2017.1390618.

[30] Z.J. Wang, Q.J. Li, Y. Li, L.C. Huang, L. Lu, M. Dao, J. Li, E. Ma, S. Suresh, and Z.W. Shan, Sliding of coherent twin boundaries, Nature comm. 8 (2017) 1108. https://doi.org/10.1038/s41467-017-01234-8.

[31] H. Liang, M. Upmanyu, and H. Huang, Size-dependent elasticity of nanowires: Nonlinear effects, Phys. Rev. B 71 (2005) 241403(1)-(4). https://doi.org/10.1103/PhysRevB.71.241403.

[32] M.D. Uchic, D.M. Dimiduk, J.N. Florando, and W.D. Nix, Sample dimensions influence strength and crystal plasticity, Science 305 (2004) 986-989. https://doi.org/10.1126/science.1098993.

[33] Y. Yue, P. Liu, Q. Deng, E. Ma, Z. Zhang, and X. Han, Quantitative evidence of crossover toward partial dislocation mediated plasticity in copper single crystalline nanowires, Nano Lett. 12 (2012) 4045-4049. https://doi.org/10.1021/nl3014132.

[34] C. Peng, Y. Zhan, and J. Lou, Size-dependent fracture mode transition in copper nanowires, Small 8 (2012) 1889-1894. https://doi.org/10.1002/smll.201101911.

[12] N.K. Bourne, Atomistic views of deformation, Nature 550 (2017) 461-463. https://doi.org/10.1038/550461a

[13] M.N. Shetty, Dislocations and mechanical behaviour of materials, Eastern Economy Edition, PHI Learning Pvt. Ltd., Delhi, 2013.

[14] D. Hull and D. J. Bacon, Introduction to dislocations, 5th edn. Butterworth-Heinemann, 2001.

[15] J.P. Hirth, J. Lothe, Theory of dislocations, McGraw-Hill Book Co., New York, 1982.

[16] G.E. Dieter, Mechanical Metallurgy, 3rd edn. McGraw-Hill Book Co., New York, 1988.

[17] K.J. Bowman and R. Gibala, Stress asymmetry in of BCC cyclic deformation metals, Acta. Metall. Mater. 40 (1992) 193-200. https://doi.org/10.1016/0956-7151(92)90213-X.

[18] Y. Shibuta, S. Takamoto, and T. Suzuki, A molecular dynamics study of the energy and structure of the symmetric tilt boundary of iron, ISIJ Int. 48 (2008) 1582-1591. https://doi.org/10.2355/isijinternational.48.1582.

[19] P. D. Bristowe and A. G. Crocker, A computer simulation study of the structures of twin boundaries in body centred cubic crystals, Philos. Mag. 31 (1975) 503-517. https://doi.org/10.1080/14786437508226533.

[20] M. Yamaguchi and V. Vitek, Twin boundaries and incoherent steps on twin boundaries in body centered cubic metals, Philos. Mag. 34 (1976) 1-11. https://doi.org/10.1080/14786437608228170.

[21] Z. Shi and C.V. Singh, Competing twinning mechanisms in body centered cubic metallic nanowires, Scripta Mater. 113 (2016) 214-217. https://doi.org/10.1016/j.scriptamat.2015.11.006.

[22] M.A. Tschopp and D.L. McDowell, Influence of single crystal orientation on homogeneous dislocation nucleation under uni-axial loading, J. Mech. Phys. Solids 56 (2008) 1806-1830. https://doi.org/10.1016/j.jmps.2007.11.012.

Bibliography

[1] C.M. Lieber and Z.L. Wang, Functional Nanowires, MRS Bull. 32 (2007) 99-104. https://doi.org/10.1557/mrs2007.41.

[2] J. Sarkar, G.G. Khan, and A. Basumallick, Nanowires: properties, applications and synthesis via porous anodic aluminium oxide template, Bull. Mater. Sci. 30 (2007) 271-290. https://doi.org/10.1007/s12034-007-0047-0.

[3] C.M. Lieber, Nanoscale science and technology: building a big future from small things, MRS Bull. 28 (2003) 486-491. https://doi.org/10.1557/mrs2003.144.

[4] American elements, Iron nanorods in http://www.americanelements.com/femnr.html.

[5] J.I. Martin, J. Nogues, K. Liu, J.L. Vicent, and I.K. Schuller, Ordered magnetic nanostructures: fabrication and properties, J. Magn. Magn. Mater. 256 (2003) 449-501. https://doi.org/10.1016/S0304-8853(02)00898-3.

[6] X.Y. Zhang, G.H. Wen, Y.F. Chan, R.K. Zheng, X.X. Zhang, and N. Wang, Fabrication and magnetic properties of ultrathin Fe nanowire arrays, Appl. Phys. Lett. 83 (2003) 3341-3343. https://doi.org/10.1063/1.1621459.

[7] C. Neetzel, T. Ohgai, T. Yanai, M. Nakano, and H. Fukunaga, Uni-axial magnetization performance of textured Fe nanowire arrays electro-deposited by a pulsed potential deposition technique, Nanoscale Res. Lett. 12 (2017) 598. https://doi.org/10.1186/s11671-017-2367-3.

[8] M.A. Zeeshan, S. Pane, S.K. Youn, E. Pellicer, S. Schuerle, J. Sort, S. Fusco, A.M. Lindo, H.G. Park, and B.J. Nelson, Graphite coating of iron nanowires for nanorobotic